

**Molecular dynamics of clathrin proteins
at endocytic sites
studied with evanescent-wave microscopy**

Dissertation

zur Erlangung des Doktorgrades der Mathematisch-Naturwissenschaftlichen Fakultäten
der Georg-August-Universität zu Göttingen

Vorgelegt von
Dinah Loerke
aus München

Göttingen 2004

D7

Referent: Prof. Erwin Neher

Korreferentin: Prof. Annette Zippelius

Tag der mündlichen Prüfung: 12. Februar 2004

Table of contents

Abstract	7
Chapter 1: Introduction	
1.1 Endocytosis	9
1.2 Clathrin-mediated endocytosis	12
1.3 Clathrin structure	14
1.4 Investigating clathrin function	17
1.5 Evanescent-wave-FRAP studies of clathrin-mediated endocytosis	18
1.6 Aims and scope of this work	21
Chapter 2: Theoretical and experimental methods	
2.1 Total internal reflection and the evanescent field	23
2.2 Evanescent-wave (EW) microscopy	27
2.3 EW calibration of the setup	27
2.4 Photobleaching recovery and diffusion	30
2.4.1 FRAP reaction limit	32
2.4.2 Bleaching in the immobile fraction	34
2.4.3 Reaction component of recovery (immobile fraction)	36
2.4.4 Diffusion (mobile fraction)	40
2.5 FRAP experiment design and analysis	45
2.5.1 Single clathrin pits	47
2.5.2 Separation of components	48

2.6 Errors and artifacts

2.6.1 Time Series Intensity Artifact	53
2.6.2 Focus Drift and error	55
2.6.3 Jackknifed error	57

Chapter 3: Experimental Material**3.1 Experimental setup**

3.1.1 Microscope and image acquisition	59
3.1.2 Laser and optical system	60

3.2 Material

3.2.1 Cells	63
3.2.2 Measuring Solutions	63
3.2.3 Fluorescent probes	64
3.2.4 Treatments and drugs	66

Chapter 4: Results**4.1 Clathrin light chain results**

4.1.1 Separation of components: light chain exchange inhibition	68
4.1.2 Separation of components: variable bleaching times	70
4.1.3 Bleaching constant	73
4.1.4 Diffusion results	73
4.1.5 Temperature dependent recovery	77
4.1.6 Inhibition of clathrin light chain exchange	78

4.2	Clathrin heavy chain results	
4.2.1	Temperature dependent recovery of heavy chain	79
4.2.2	Inhibition of clathrin heavy chain exchange	80
4.2.3	Model for clathrin heavy chain exchange	81
Chapter 5: Discussion and Outlook		
5.1	Clathrin exchange studied by photobleaching recovery	89
5.2	Clathrin light chain and heavy chain interaction	92
5.3	Outlook	95
	Appendix	96
	References	97
	Acknowledgements	101
	Curriculum Vitae	103

Abstract

Clathrin (consisting of a light chain and a heavy chain subunit) is a triskelion-shaped molecule that self-assembles into polyhedral lattices on cellular membranes. It has a pivotal role in membrane transport inside the cell, as the curvature of the clathrin lattice can be increased to form a clathrin “pit”, which serves to progressively invaginate the attached patch of membrane to form a small membrane sphere (called vesicle), which is then pinched off from the membrane. To study the cellular regulation of the self-assembly of clathrin pits, the binding/unbinding kinetics of fluorescent fusion constructs of the two clathrin subunits were investigated using evanescent-wave (EW) microscopy in conjunction with photobleaching recovery.

EW microscopy makes use of the evanescent wave created by total internal reflection of a laser beam (at the dielectric interface between a glass coverslip and a specimen in aqueous medium) for fluorescence excitation. Through the exponential decay of the evanescent field, fluorescence excitation is restricted to a thin layer on top of the interface (with a thickness on the order of magnitude of the light wavelength); thus, the technique is ideally suited to study cellular processes in the vicinity of the membrane. Fluorescence recovery after photobleaching (FRAP) is used to estimate the speed of unbinding of fluorescent clathrin molecules from single clathrin pits (as the time constant of exponential reaction recovery constitutes the unbinding time constant $1/k_{\text{off}}$). Since the reaction signal is partly masked by the diffusion of cytosolic fluorophores, one important aim of this work was to separate reaction and diffusion signals to permit a quantitative estimation of unbinding kinetics.

At room temperature, the unbinding time constant of clathrin light chain was estimated to be $\tau=18.9\pm 1.3\text{s}$. Light chain exchange from pits is blocked by sucrose treatment, by calcium depletion or ATP depletion of the cell. For clathrin heavy chain, it was found that the unbinding time constant is faster than for light chain. Additionally, the treatments which completely inhibit clathrin light chain exchange from pits do not abolish heavy chain recovery. It is concluded that for heavy chain, a light-chain independent exchange pathway with a faster time constant exists, which is isolated through calcium and ATP depletion, and its time constant is estimated to be $10.0\pm 0.9\text{s}$. The contributions of the different pathways are modulated by selective overexpression of the clathrin subunits.

It can be concluded that clathrin light chain, in turn, therefore has a role in stabilising heavy chain molecules bound in pits, as well as in modulating clathrin function *in vivo* in a calcium- and ATP-dependent manner.

Chapter 1

Introduction

1.1 Endocytosis

Endocytosis is the formation of an intracellular vesicle (a small membrane-bound compartment resembling a lipid sphere) in a cell by membrane invagination. By this mechanism, cells absorb material from the outside, as the invagination engulfs extracellular fluid including material dissolved or suspended in it, or material associated with the membrane. Endocytosis is required for a large number of essential cell functions, including nutrient uptake, communication between cells, and the modulation of the composition of the membrane. The reverse process, where filled vesicles fuse with and collapse into the membrane to release their contents into the extracellular medium, is called exocytosis.

Endocytosis exists in different forms: *Phagocytosis* is the process by which the cell ingests large objects, such as prey cells or pieces of dead organic matter. In *pinocytosis*, the membrane invaginates to form a pocket filled with extracellular fluid, after which the pocket pinches off to form a vesicle. *Receptor-mediated endocytosis* is similar to pinocytosis, but it is prompted by the binding of an extracellular molecule, e.g. a protein, to a receptor embedded in the membrane. The invagination then engulfs the receptor and the bound extracellular molecule.

For example, in vertebrates, iron is transported in the blood bound to a protein called transferrin. Cells have transferrin receptors on their surface, and they tightly bind a transferrin molecule when they encounter it. The complex of transferrin and its receptor is then internalized by receptor-mediated endocytosis, and ultimately, the iron is released into the cytosol. Even if only a small amount of transferrin is present in the extracellular medium, the strong affinity of the transferrin receptor for transferrin (its ligand) will pull out the available molecules. Through this selectivity, receptor-mediated endocytosis is extremely efficient in acquiring a particular substance, much more so than simple pinocytosis.

The constitutive forms of exocytosis and endocytosis (those forms that occur continuously in all cell types) have an important role in housekeeping: The vesicle fusion supplies the membrane with newly produced material from inside the cell, and endocytosis permits the recycling of membrane components, including the retrieval of surface proteins destined for degradation, and the internalisation of nutrients and receptors with extracellular ligands.

Additionally, some (but not all) cell types have a pathway of regulated exo- and endocytosis, which permits the cell to respond to an external stimulus. In this case, vesicles filled with transmitters or hormones fuse with the membrane and release their contents into the extracellular medium. Endocytosis counteracts the increase in membrane surface area caused by addition of fusing vesicles, and recycles vesicles required for a new round of fusion. Regulated exo-/endocytosis is of particular interest and has been studied extensively in neuronal synapses, where the release of neurotransmitter in response to an electrical stimulus is the basis of signal transduction. It is, however, also the underlying functional mechanism of secretion in non-neuronal cells; these include digestive secretion, secretion from the tear glands, from mammary glands, or endocrine and neuroendocrine glands. For example, beta cells in the pancreas secrete insulin in response to an elevated glucose concentration, and chromaffin cells in the adrenal medulla secrete adrenalin in response to acetylcholine.

The most important and common functional pathway for membrane retrieval both in constitutive and regulated secretion is clathrin-mediated endocytosis (Heuser and Reese, 1973, Pearse, 1976, Takei et al., 1996, Shupliakov et al., 1997, Augustine et al., 1999, Marsh and McMahon, 1999). This is a form of endocytosis mediated by vesicles that have a morphologically distinct bristle coat (which is made up of a protein complex including clathrin), forming from membrane domains called clathrin pits.

A study of neuromuscular junction (Heuser and Reese, 1973) found that after depolarisation, clathrin-coated structures could be labeled with a fluid-phase marker, and that endocytic pits appeared after a brief depolarisation. They proposed that during fusion, a vesicle collapses fully, flattening out into a patch in the surrounding membrane, after which it diffuses laterally to a different area, where it is retrieved by the invagination of the membrane patch with the help of clathrin. Clathrin polymerises on the membrane into the clathrin-coated pits, which cause the membrane to curve inward to gradually form an invagination. When the vesicle is fully formed, it is pinched off from the membrane and transported into the cell interior (see fig. 1.1).

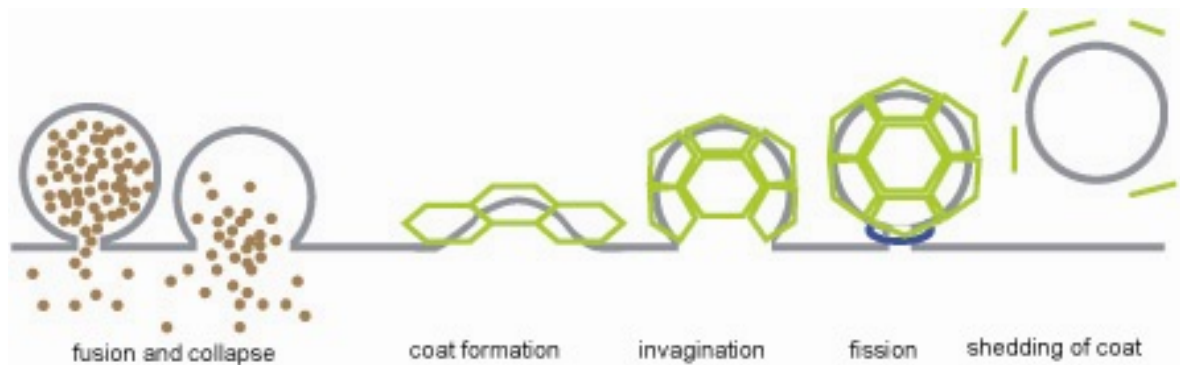


Fig. 1.1: Schematic of clathrin-mediated endocytosis.

Other mechanisms of endocytosis include a slow endocytic pathway which works via large tubular infoldings (*caveolae*) (Takei et al., 1996), and the *kiss-and-run* mechanism involving the brief opening of a fusion pore (Ceccarelli et al., 1973; Koenig et al., 1998, Aravanis et al., 2003), and a re-closing of the vesicle instead of collapsing, which is thought to permit rapid retrieval without the involvement of clathrin. This mechanism was proposed in response to several observations: It was shown that in electron micrographs, omega-shaped profiles exist at the membrane without the presence of clathrin, which were interpreted as vesicles connected to the membrane through a small opening (e.g. Koenig et al., 1998). The transient opening of a fusion pore has been observed with electrophysiological and amperometric measurements (e.g. Chow et al., 1992; Alvarez de Toledo et al., 1993). Also, several studies investigating the kinetics of endocytosis at the hippocampal synapse (e.g. Ryan, 1996; Klingauf et al., 1998; Aravanis et al., 2003) suggest that there are two types of endocytosis, a fast type with a half-time on the order of a few seconds, and a slow type with a half-time on the order of 20s.

1.2 Clathrin-mediated endocytosis

Clathrin-mediated endocytosis, the subject of this study, consists of several morphologically distinct steps. First, clathrin is recruited from the cytosol and forms a coat by binding (via adaptor proteins) to the membrane, and the pit is progressively invaginated. After full invagination, the neck of the pit is constricted to effect fission from the membrane. After pinching off from the membrane, the clathrin coat is quickly disassembled from the vesicle in the cytosol (Cremona and De Camilli, 1997; Brodin et al., 2000; Jarousse and Kelly, 2001; Gundelfinger et al., 2003).

Clathrin-coated vesicles are found in virtually all cells. Clathrin-mediated endocytosis, apart from its role in vesicle recycling in regulated secretion, is the key mechanism in sorting proteins in the trans-Golgi network, in selective translocation of receptors from one intracellular membrane to another, as well as nutrient uptake through receptor-mediated endocytosis. In fact, the majority of material entering the cells from the outside does so by coated pits at the membrane.

At least two sets of proteins are involved in this form of endocytosis: those that form the clathrin coat, and their accessory proteins (Brodin et al., 2000; Slepnev and De Camilli, 2000). The core components of clathrin coats are the clathrin triskelion and the AP-2 adaptor complex. Clathrin was found in 1976 (Pearse, 1976), followed in 1984 (Pearse and Robinson, 1984) by the adaptor protein complex AP-2. Clathrin triskelia have a strong tendency to self-assemble *in vitro*; under certain conditions, they also do so on biological membranes, and assemble from the pool of subunits in the cytosol to form a hexagonal lattice on the plasma membrane (Kirchhausen, 2000; Slepnev and De Camilli, 2000; Brodsky et al., 2001; McPherson et al., 2001; Smith et al., 1998; Moore et al., 1987; Heuser, 1980).

The clathrin coat cannot directly attach to the membrane, since it does not interact with the lipid bilayer, but connects to the membrane through the adaptor complex AP2. The first step in the formation of a pit, the nucleation, is thought to take place when AP-2 binds to a receptor; the nucleation site then starts to recruit clathrin triskelia and induces them to polymerize onto its template (see fig.1.2). (In some cases, the order is thought to be reversed, e.g. for agonist-activated G-protein coupled receptors, which are thought to target to pre-

existing clathrin-coated pits, as opposed to inducing coat formation *de novo* (Santini et al., 2002; Scott et al., 2002).

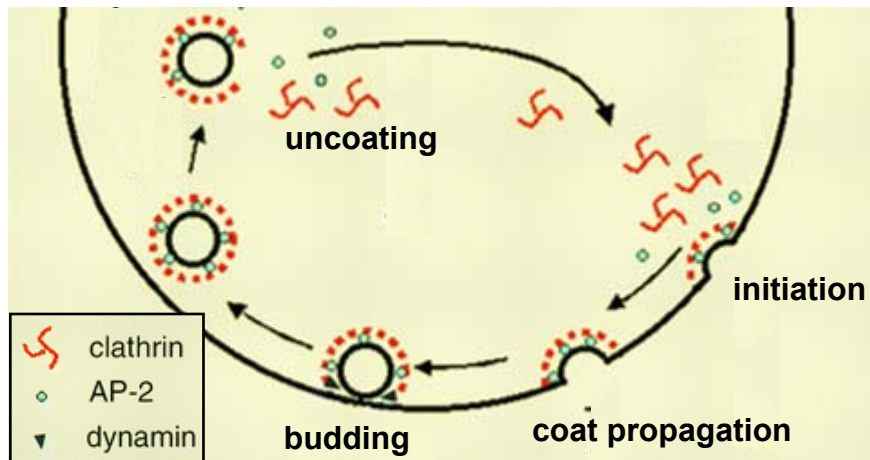


Fig. 1.2: Schematic of clathrin-mediated endocytosis (Adapted from Kirchhausen, 2000).

AP-2 is a heterotetrameric complex which is usually required both to bind the clathrin coat to the membrane and to recruit cargo molecules into the pit; it is thought to also recruit additional proteins involved in endocytosis. Apart from clathrin, AP-2 has additional binding sites to e.g. dynamin and amphiphysin, as well as the calcium-binding protein synaptotagmin (Zhang et al., 1994). It should also be noted that AP-2 is indispensable to some, but not all pathways of endocytosis, and may be replaced by alternative adaptors in some pathways (Motley et al., 2003; Conner and Schmid, 2003).

After the initial trigger of coat formation, the binding of clathrin to AP-2, a one-to-one stoichiometry for clathrin and AP-2 is no longer needed, since, once seeded, cooperative clathrin coat assembly can proceed with only occasional clathrin/AP-2/membrane interactions. As the clathrin lattice grows, it forms a scaffold of hexagons and pentagons (where the incorporated pentagons increase the curvature of the lattice), and thus progressively invaginates the attached membrane.

While coat and lattice formation occur spontaneously from clathrin *in vitro* at low pH, and while it is triggered intracellularly by merely adding AP-2 and clathrin at physiological pH (Moore et al., 1987), additional accessory proteins are required for budding, i.e. the pinching off of the clathrin-coated vesicle from the membrane. The fission of the neck of the coated vesicle requires both ATP, GTP and protein fission machinery. Dynamin, a GTPase, is one of the key constituents. Its function was first described by

characterisation of a temperature-sensitive mutant in *Drosophila* (*shibire*), where the protein becomes non-functional at the so-called non-permissive temperature. Morphologically, it was characterised by a cessation of endocytosis. Electron micrographs show long-necked pits that failed to fully separate from the membrane as the specific defect (Kosaka and Ikeda, 1983).

After budding, a vesicle is transported into the cell interior to its destination (the site of action of its cargo, or for refilling). The clathrin coat of the vesicle was traditionally thought to be disassembled rapidly after pinching off from the membrane, since free coated vesicles are rarely seen in electron micrographs. However, a study using live cell imaging (Merrifield et al., 2002) estimated the time course of uncoating to be on the order of 60s. The uncoating activity is largely attributed to the heat shock protein hsc70 and auxilin (Ungewickell et al., 1995).

1.3 Clathrin structure

Clathrin, the scaffold protein of the clathrin coat, provides the driving force behind the generation of coated pits and coated vesicles with its assembly into progressively curved lattices. Isolated from vesicles, the basic subunit of clathrin pits are three 190-kDa heavy chains and three light chains (25-27kDa). The heavy chains form a three-limbed structure (triskelion) in which the light chains span the inner segments of each limb and are in position to interact with other proteins (see fig. 1.3).

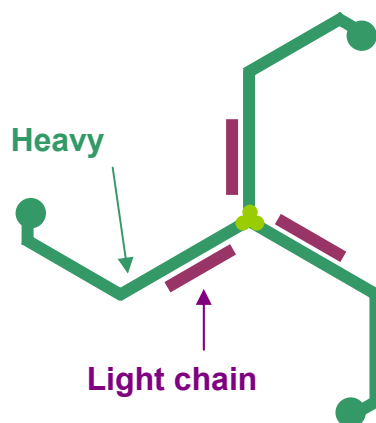


Fig. 1.3: Clathrin triskelion comprised of heavy and light chain.

Light chains bind to heavy chains with high affinity ($K_D < 10^{-10}$ M) (Winkler and Stanley, 1983). The N-terminus of the heavy chain, which interacts with AP-2, is known as the globular domain, the C-terminals are located at the vertex (where the three legs meet). Clathrin triskelia assemble into lattices comprising hexagons and pentagons. Purely hexagonal lattices are flat, but by adding pentagons, a curved surface is formed. To provide sufficient curvature to form a closed surface of hexagons and pentagons, there must be exactly 12 pentagons. Electron microscopic images show extended hexagonal arrays of clathrin (Heuser, 1980).

To introduce curvature into flat hexagonal lattice by restructuring hexagons into pentagons requires massive local disassembly. Since this rearrangement is energetically unfavorable (as it requires the breaking of many protein-protein interactions), and since there are also many incidences of budding coated pits without flat lattices present, it was thought to be more likely that the flat lattices might constitute reservoirs, or that the formation of pentagons takes place at the edges of lattices.

However, two studies using confocal microscopy (Wu et al., 2001; Wu et al., 2003) demonstrated that there is considerable exchange between soluble and membrane lattice pools even under conditions that block endocytosis, which would make massive restructuring possible; also, another live dell imaging study (Merrifield et al., 2002) suggests that flat lattices can be rearranged into functional pits.

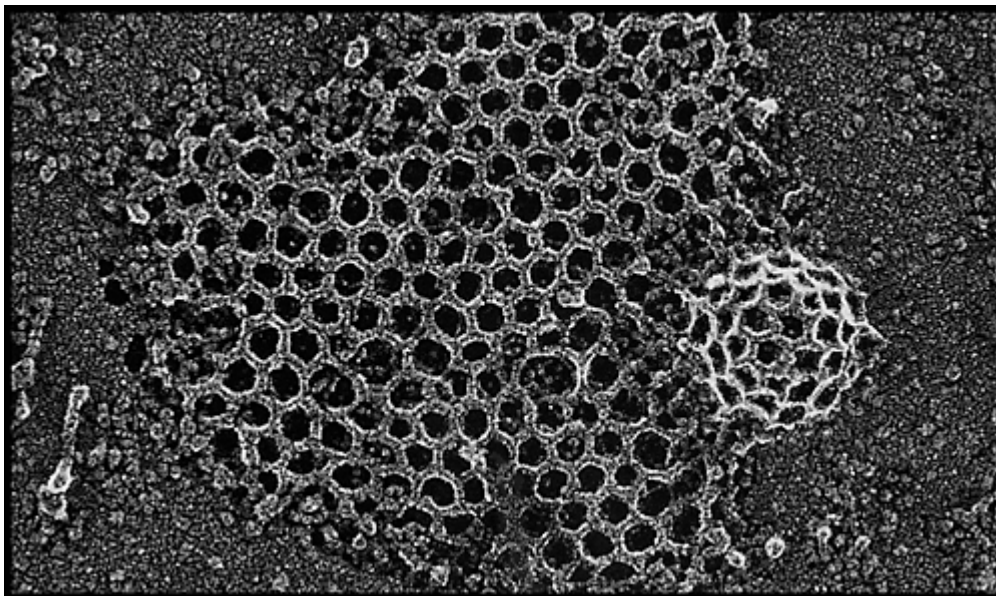


Fig. 1.4: Deep-etch electron micrograph of coated pit structure. Image by John E. Heuser, Washington University School of Medicine, St. Louis, Missouri.

Clathrin lattices can have an outside diameter ranging from 60-200nm (Crowther et al., 1976; Pearse, 1982). In non-neuronal cells, clathrin coated pits have varying sizes, but in neuronal cells, their size is very uniform (Zhang et al., 1998; Zhang et al., 1999), and is thought to be regulated by the adaptor protein AP-180, the neuronal form of AP-2.

The cell has to regulate the time and location of clathrin assembly, to recruit clathrin molecules from intracellular pools, and to control disassembly, with intracellular molecular signals. These signals, based on current knowledge, are probably directed at clathrin light chain, which thus serves as mediator of clathrin function.

In higher eukaryotes, there are two types of clathrin light chain, LCA and LCB, encoded by separate genes and expressed in every cell type (Brodsky, 1988). A clathrin light chain molecule can be considered to be a linear array of functionally distinct domains (e.g. Kirchhausen et al., 1987); these include an hsc70-binding sequence, an EF-hand type calcium binding sequence, and for LCB, also a phosphorylation target sequence.

Calcium affinity of light chains to calcium is $K_D=25\mu\text{M}$, predicting that 1-5% of light chains have calcium bound to them at steady-state intracellular conditions (Brodsky et al., 1991). These authors also suggest that, considering the position of the calcium-binding motif within the structure of the light chain, its influence could be exerted in two ways: On the one hand, the calcium binding site is close to the binding site for hsc70, the clathrin-uncoating protein. On the other hand, it could affect the conformation of the adjacent alpha-helix which is involved in heavy chain binding and triskelion assembly. If there is a calcium-mediated stabilisation of the complex, this might explain why high concentrations of calcium (2-5mM) can rapidly induce assembly of purified clathrin *in vitro* (Keen et al., 1979).

As a consequence, it is probable that clathrin light chain function (but not necessarily clathrin heavy chain) is sensitive to the presence and concentration of Ca^{2+} and ATP. This fact was investigated in this study by studying cells under conditions of depleted Ca^{2+} or ATP.

In the presence of light chains, clathrin self-assembly is exquisitely sensitive to regulation and depends on salt bridges that form only at low pH. Thus it has been proposed that cellular clathrin assembly is controlled via the simple biochemical mechanism of reversing the inhibitory effect of the light-chain regulatory sequence, thereby promoting high-affinity salt bridge formation (Ybe et al., 1998). However, it has also been reported that

in vitro, assembly properties of clathrin are not affected significantly by absence of light chains, so that the light chain regulatory role is a crucial characteristic of *in vivo* clathrin function (Winkler and Stanley, 1983; Ybe et al., 1998; Lindner and Ungewickell, 1991).

1.4 Investigating clathrin function

The earliest reconstruction of the time course of clathrin-mediated endocytosis was obtained in neuromuscular junction from electron micrographs (Miller and Heuser, 1984), yielding an estimate on the order of 90s. Live cell imaging of clathrin function became possible with the development of fusion proteins, which are genetically encoded fluorescent probes consisting of enhanced green fluorescent protein (EGFP, a fluorescent protein originally from the jellyfish *Aequorea victoria*) and the endogenous protein of interest. We used a fusion protein of EGFP with either clathrin light chain A (LCA) (Gaidarov et al., 1999) or clathrin heavy chain (Damer and O'Halloran, 2000), which permitted the visualisation of clathrin dynamics of constitutive endocytosis in real time. Combined with evanescent field microscopy the formation, single clathrin-coated vesicle fission as well as their movement from the membrane into the cytosol could be studied in mammalian cells (Merrifield et al., 2002; Rappoport and Simon, 2003). In another study expressing clathrin-GFP in hippocampal neurons (Blanpied et al., 2002), single coated pits were imaged in thin processes like dendrites and spines at low expression levels, and it was found that coat assembly in constitutive endocytosis is slow ($\tau \sim 20$ s at 37°C), while uncoating appeared to be four times faster. It is not clear, however, exactly how the rate of coat assembly (i.e. propagation) relates to the binding/unbinding rate of clathrin molecules to and from pits investigated in this study.

Of particular interest to this study is the interaction of clathrin light chain with heavy chain. It was shown *in vitro* (Winkler and Stanley, 1983) that clathrin can be reversibly dissociated into heavy chain trimers and light chains, and that heavy chain trimers reassemble into regular polygonal cage structures in the absence of light chains; so while light chains have a high affinity binding site on the heavy chain, they are not essential for the formation of regular cage structures. In recombinant hubs (the central part of the clathrin triskelion, lacking the extended bended leg), self-assembly takes place without light chains at physiological pH, while light-chain-bound hubs assemble only below pH 6.5 (Liu et al., 1995). It was subsequently proposed, also on the basis of *in vitro* data, that clathrin light

chain regulates the pH dependence of hub assembly through controlling the formation of salt bridges, so that light chains provide an inhibition of (non-productive) spontaneous assembly at physiological pH, which may be reversed by adaptors (Ybe et al., 1998). Investigating clathrin function *in vivo* in *Dictyostelium*^{*}, one study (Wang et al., 2003) found that the clathrin light chain did not influence steady state levels of clathrin, triskelion formation, or contribute to clathrin overassembly on intracellular membranes, but that light chain knockouts showed a decreased association of clathrin with intracellular membranes.

In contrast, a study on yeast (Huang et al., 1997) describes that light chain-deficient cells showed phenotypes similar to those displayed by yeast that have a disruption in the clathrin heavy chain gene. Their results indicate that the light chain is important for heavy chain trimerisation in yeast.

In light of these results, it can be concluded that the clathrin light chain is pivotal at least for the *in vivo* control and regulation of clathrin pits, but is probably not indispensable for coat formation as such.

1.5 Evanescent-wave-FRAP studies of clathrin-mediated endocytosis

Through the development of fluorescent probes specifically targeted to organelles and proteins inside the cell, fluorescence microscopy has become an excellent tool to visualize dynamic processes in the cell. In many cases, the protein of interest is ubiquitous inside the cell and its fluorescence signal from the region of interest is completely obscured by the contribution of other parts of the cell. Therefore, a number of fluorescence microscopic methods target the problem of out-of-focus light to improve signal-to-background resolution. These include confocal microscopy, where fluorescence generated outside the focus is rejected by a confocal pinhole (Minsky, 1988), two-photon-microscopy, where fluorescence excitation is spatially restricted to the focus of a laser beam through the non-linear relationship between intensity and two-photon excitation probability (Denk et al., 1990) - or evanescent-wave microscopy, which has been used in this work (Axelrod, 1981).

^{*} *Dictyostelium discoideum*: A cellular slime mould, growing as a soil-living amoeba which feeds on bacteria

Total internal reflection of a laser beam at the interface between two media of different refractive indices creates a so-called evanescent wave, an inhomogeneous electromagnetic field, in the optically rarer medium.

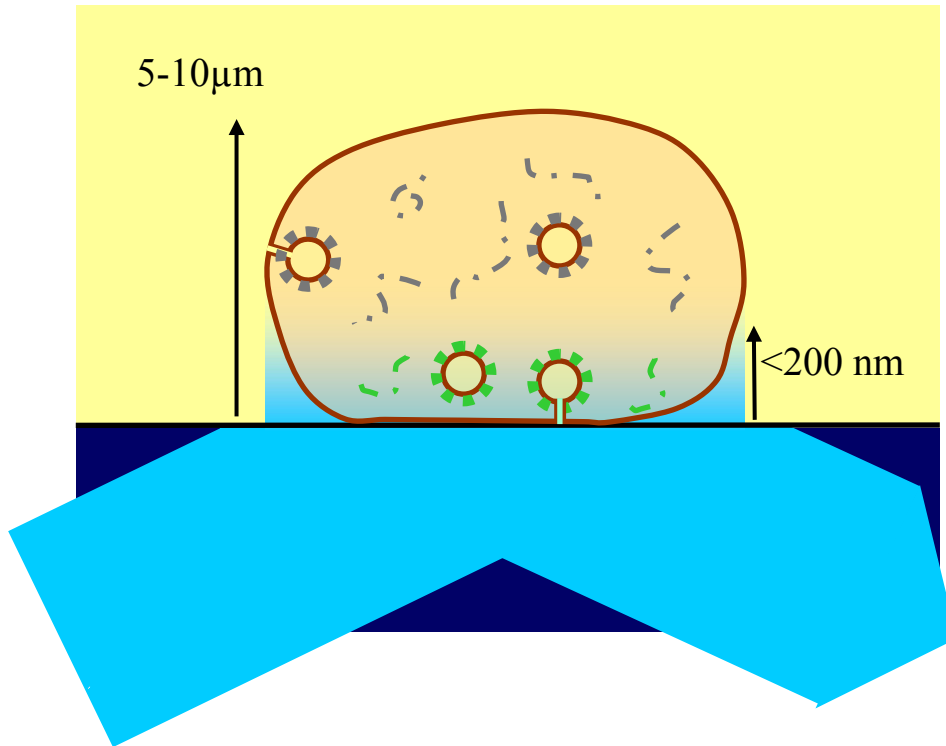


Fig.1.5: Schematic of total internal reflection of laser beam at interface, generating an evanescent wave in the lower-index medium. EW illumination selectively excites fluorophores in the cell only in the immediate vicinity of the membrane.

This evanescent field has the useful characteristic that its intensity decays very rapidly with distance from the interface – typically within some tens to hundreds of nanometers, depending on the light wavelength, the incidence angle, and the refractive indices. In evanescent-wave (EW) fluorescence microscopy, the EW is employed to excite fluorescence in a restricted volume of the specimen.

For a cell grown onto a glass coverslip in aqueous culture medium, the glass surface to which the cell attaches constitutes the dielectric interface for total internal reflection. Thus, the EW will excite fluorescence in the aqueous medium only in the immediate vicinity of the surface, and therefore only in a thin layer inside the cell just above the cell membrane, while the fluorescence signal from regions deeper within the cell is suppressed (see figure 1.5). This technique lends itself naturally to the study of secretion, as well as other processes which are localized to the cell membrane (e.g. Steyer et al., 1997; Oheim et al., 1998; Oheim et al., 1999; Steyer and Almers, 1999; Zenisek et al., 2000). It also has been used to study clathrin dynamics at the plasma membrane, using dual-color imaging of clathrin light chain

constructs together with fluorescent actin or dynamin constructs (Merrifield et al., 2002; Rappoport and Simon, 2003).

Fluorescence recovery after photobleaching (FRAP) is a method in fluorescence microscopy particularly suited to study rates of motion and adsorption/desorption kinetics. It is based on the phenomenon of photobleaching, where a fluorescent specimen is illuminated with intensely strong light, so that some fluorescent molecules will be irreversibly blanked by photon damage (via radical formation due to excited states of the dye molecules). FRAP makes use of this effect by bleaching transiently and locally in a small subregion of the specimen (in our case, in the evanescent field, which illuminates only a subsection of the cell); after the illumination is returned to the initial low intensity, the fluorescence recovers due to an exchange of bleached and unbleached molecules from outside the bleached region. The observed recovery permits the estimation of the kinetic parameters that underlie the relevant dynamic process of recovery.

The technique has been used in conjunction with EW excitation to study cytoplasmic viscosity (Swaminathan et al., 1996), to study binding/unbinding kinetics of rhodamine actin or phalloidin at the cytofacial surface of the cell membrane (Sund and Axelrod, 2000), receptor binding (Gesty-Palmer and Thompson, 1997), and protein adsorption dynamics (Burghardt and Axelrod, 1981; Thompson et al., 1981; Stout and Axelrod, 1995). FRAP has also been used in conjunction with confocal excitation and bleaching to image clathrin light chain dynamics (Wu et al., 2001; Wu et al., 2003), and to study the chemical disruption of clathrin function (Moskowitz et al., 2003).

In two of the studies cited above (Wu et al., 2001; Wu et al., 2003), the speed of clathrin light chain molecules unbinding from coats (k_{off}) is calculated as the speed of bleaching recovery. These studies yield values of the recovery halftime in the range of 16-30s (for temperatures ranging from 37°-28°C). Additionally, they demonstrate that exchange of clathrin and AP2 from coats at the plasma membrane still takes place under conditions where clathrin-mediated endocytosis is blocked, and that AP2 continues to exchange under conditions that block clathrin light chain exchange. The other FRAP study (Moskowitz et al., 2003) addresses clathrin light chain recovery under different conditions, using varying amplitudes of photobleaching recovery as a measure of chemical disruption of clathrin function. While they do not calculate a value, a rough estimation of k_{off} halftime from their

published data yields a value around 35s (at 37°C), which is in the same range as, if somewhat slower than the values from the other papers discussed above.

Neither of these FRAP studies on clathrin, however, accounts for diffusion. In a FRAP experiment with the typical bleaching durations on the order of 10s to bleach clathrin-coated pits at the membrane, the individual pits are immersed in a background of freely diffusible fluorophores in the cytosol. The local bleaching also creates a gradient of fluorescent vs. bleached fluorophores in this diffusive fraction, as molecules drift in and out of the focal volume during the bleaching interval.

After the end of the bleaching pulse, diffusion contributes to the recovery of bleached pit: Firstly, the speed of pit recovery may be limited by the re-supply of diffusive fluorescent material. Secondly, the measured pit signal itself contains a diffusive component, as pits are in most cases sub-resolution structures, and any region of interest used to record the intensity of the pit diffraction image also contains intensity contributions from diffusing molecules flowing around the pit. Therefore, *quantitative* assessment of clathrin dynamics should account for a slow diffusional component, and thus the recovery signal should be corrected for diffusion.

1.6 Aims and scope of this work

The studies using confocal FRAP to address clathrin exchange cited above provide fundamental information about clathrin light chain exchange and blocking conditions, and they give an estimate for the speed of recovery. They neglect, however, to consider any contributions of free diffusion.

In this work, evanescent-wave microscopy is used to image single fluorescently labeled clathrin-coated pits in chromaffin cells (neuroendocrine cells from the adrenal medulla) and HEK cells (a human embryonic kidney cell line). In FRAP experiments, cells are illuminated with high intensity to photobleach the pits located at the membrane; from the recovery of the pit signal, the off-rate of clathrin molecules binding to stationary pits is calculated. In this work, particular note is taken of the contribution of diffusion to this recovery. The correction for diffusive background yields more precise estimations for the time-constant of unbinding

from pits than previously published. Additionally, by using a novel clathrin heavy chain fusion construct (to our knowledge, the first use of a mammalian construct) it was possible to directly compare the dynamics of light chain and heavy chain constructs in clathrin-coated pits. The results reveal that clathrin heavy chain can unbind from pits independently of clathrin light chain and with a faster time-course. This corroborates a stabilising role of light chain molecules in clathrin pits.

Chapter 2

Theoretical and Experimental Methods

2.1 Total internal reflection and the evanescent field

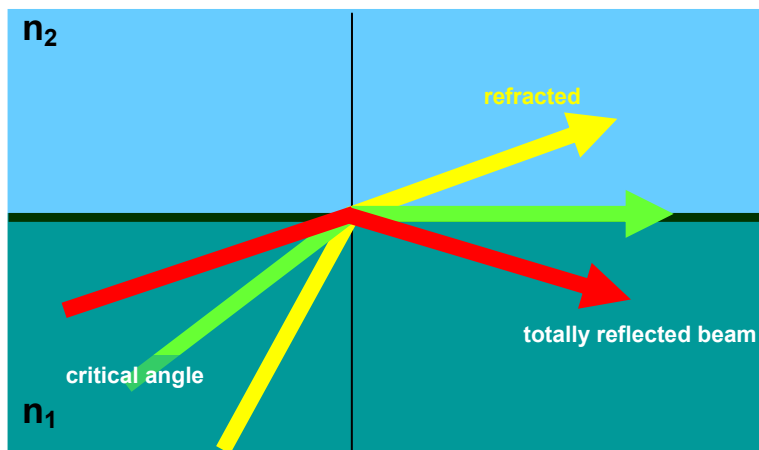


Fig. 2.1: Schematic of total internal reflection at a dielectric interface.

A light beam incident under an angle θ onto a dielectric interface between two media of differing refractive indices (medium 1 with n_1 and medium 2 with n_2 , where the beam is incident from medium 1) is refracted according to Snell's Law:

$$\sin \theta / \sin \theta_2 = n_2 / n_1 . \quad (\text{eq. 21})$$

In the case of $n_1 > n_2$, there exists a critical angle $\theta_c = \sin^{-1}(n_2/n_1)$ for which $\sin \theta_2 = 1$, so that the refracted beam is deflected at 90° , i.e. parallel to the interface. For even larger incidence angles with $\theta > \theta_c$, the incident beam is totally internally reflected. For the values of n in this study ($n_1 = 1.52$ for glass, $n_2 = 1.33$ for aqueous medium), the critical angle is 61.04° .

A thorough treatment from the perspective of wave optics is found e.g. in Hecht, 2002. In brief, Fresnel's equations show that the fraction of reflected light increases steadily for increasing incidence angle, while the fraction of refracted transmitted light decreases. The equations for the amplitude reflection coefficients can be formulated to

$$r_s = \left(\frac{E_{0r}}{E_{0i}} \right)_s = \frac{\cos \theta - \sqrt{(n_2/n_1)^2 - \sin^2 \theta}}{\cos \theta + \sqrt{(n_2/n_1)^2 - \sin^2 \theta}}$$

$$r_p = \left(\frac{E_{0r}}{E_{0i}} \right)_p = \frac{(n_2/n_1)^2 \cos \theta - \sqrt{(n_2/n_1)^2 - \sin^2 \theta}}{(n_2/n_1)^2 \cos \theta + \sqrt{(n_2/n_1)^2 - \sin^2 \theta}}$$

where E_{0i} , E_{0r} are the incident and reflected field amplitude and θ is the incident angle, and the indices s and p denote the components perpendicular to the incidence plane (s from German *senkrecht*, here corresponding to the y -direction) and parallel (p) to it (i.e. in the x,z -plane).

From these equations, it can be calculated that for $n_1 > n_2$ and $\theta > \sin^{-1}(n_2/n_1)$ (the conditions for total internal reflection) the reflectance R is

$$R = \left(\frac{E_{0r}}{E_{0i}} \right)^2 = r^2 = 1,$$

Therefore, the reflected and transmitted intensities are

$$I_r = |E_{0r}|^2 = |E_{0i}|^2 = I_i \quad \text{and} \quad I_t = |E_{0t}|^2 = 0;$$

thus, while the transmitted wave has to exist for continuity reasons, on average, no energy is carried across the interface. The wave function for the transmitted electric field in the x,z -plane is:

$$\vec{E}_t = \vec{E}_{0t} \exp i \cdot (\vec{k}_t \cdot \vec{r} - \omega t) = \vec{E}_{0t} \exp i \cdot (k_{tx}x + k_{tz}z - \omega t) \quad (\text{eq. 22})$$

where $\vec{k} = (k_{tx}, 0, k_{tz})$, and $k_{tx} = k_t \sin \theta_t$ and $k_{tz} = k_t \cos \theta_t$.

From substitution of Snell's Law (eq. 21), it is known that the cosine of the refracted angle is

$$\cos \theta_t = \pm \left(1 - \sin^2 \theta \cdot n_1^2 / n_2^2 \right)^{1/2}$$

With the conditions defining total internal reflection ($n_1 > n_2$ and $\theta > \sin^{-1}(n_2 / n_1)$), the cosine becomes imaginary. After its substitution into the above wave function (eq. 24), the resulting function is no longer a propagating wave, but the inhomogeneous evanescent field which, as can be seen from the equation, propagates in x-direction (parallel to the interface) and decays exponentially in z-direction:

$$\begin{aligned} \vec{E}_t &= \vec{E}_{oi} \exp(i(k_t x \sin \theta_t + k_t z \cos \theta_t)) \\ &= \vec{E}_{oi} \exp(ik_t x (n_1 / n_2) \sin \theta) \cdot \exp\left(-k_t z \sqrt{(\sin \theta \cdot n_1 / n_2)^2 - 1}\right) \end{aligned}$$

The distance-dependent evanescent intensity is described by an exponential decay function

$$I(z) = I(0) \cdot \exp(-z / d_p), \quad (\text{eq. 23})$$

where d_p (for *penetration depth*) is the space constant of the exponential decay.

d_p depends on the light wavelength, the incidence angle and the ratio of refractive indices:

$$d_p = \lambda / (4\pi \cdot \sqrt{n_1^2 \cdot \sin^2 \theta - n_2^2}) \quad (\text{eq. 24})$$

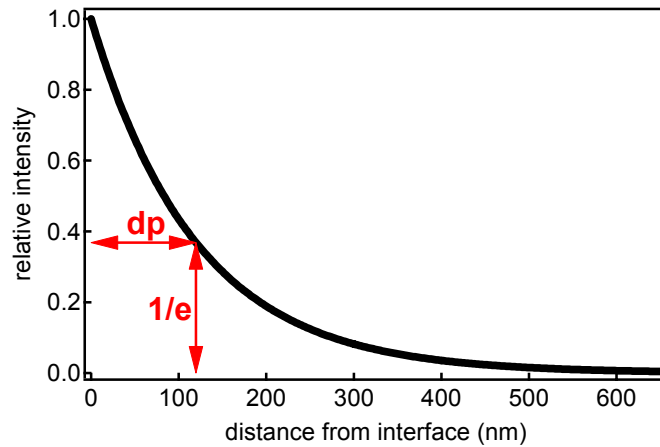


Fig. 2.2: Exponential decay of evanescent field intensity.

From the Fresnel equations, the *s*- and *p*- polarized components of the intensity are

$$I_s(0) = |E_s|^2 4 \cos^2 \theta_i / (1 - n_2^2 / n_1^2)$$

$$I_p(0) = |E_p|^2 \frac{4 \cos^2 \theta_i (2 \sin^2 \theta_i - n_2^2 / n_1^2)}{(n_2 / n_1)^4 \cos^2 \theta_i + \sin^2 \theta_i - n_2^2 / n_1^2}$$

where E_s and E_p are the incident s - and p - polarized amplitudes.

The x, y, z components of the field amplitude are

$$E_x = \left[\frac{2 \cos \theta \sqrt{\sin^2 \theta - n_2^2 / n_1^2}}{\sqrt{(n_2 / n_1)^4 \cos^2 \theta + \sin^2 \theta - (n_2 / n_1)^2}} \right] E_p e^{-i(\delta_p + \pi/2)}$$

$$E_y = \left[\frac{2 \cos \theta}{\sqrt{1 - (n_2 / n_1)^2}} \right] E_s e^{-i\delta_s}$$

$$E_z = \left[\frac{2 \cos \theta \sin \theta}{\sqrt{(n_2 / n_1)^4 \cos^2 \theta + \sin^2 \theta - (n_2 / n_1)^2}} \right] E_p e^{-i\delta_p}$$

$$\text{where } \delta_p = \tan^{-1} \left[\frac{\sqrt{\sin^2 \theta - (n_2 / n_1)^2}}{(n_2 / n_1)^2 \cos \theta} \right] \text{ and } \delta_s = \tan^{-1} \left[\frac{\sqrt{\sin^2 \theta - (n_2 / n_1)^2}}{\cos \theta} \right].$$

The angular dependence of the phase factors gives rise to a measurable longitudinal shift of a finite sized beam, known as the Goos-Hanchen shift.

In collecting fluorescence excited with an evanescent field, the main advantage of the method – the fact that fluorescence is excited only in the immediate vicinity of a dielectric interface – may create some problems in quantitatively interpreting the results. The reason is that the emission characteristics of a fluorescent dipole are significantly perturbed by the presence of a dielectric surface, which affects its intensity, angular distribution, quantum yield, and lifetime.

When the fluorophore is at distances (from the interface) on the order of or longer than the optical wavelength, the dominating effect is the interference between the propagating (far-field) emitted light and its reflection at the interface. For even smaller distances, in addition, the optical near-field of the fluorophore has to be considered for the surface optical effects. As a consequence, depending on a fluorophore's distance from the interface, varying fractions of its total emitted fluorescence are radiated into a certain spatial angle, and varying fractions, therefore, are collected by the microscope objective. A thorough treatment of this problem is found in the literature (e.g. Hellen and Axelrod, 1987; Olveczky et al., 1997).

2.2 Evanescent-wave (EW) microscopy

A broad overview of the varying strategies to integrate evanescent-wave excitation into different types of microscopes can be found in Axelrod (2001). The method used in this work through-the-objective type illumination (see figure 2.3).

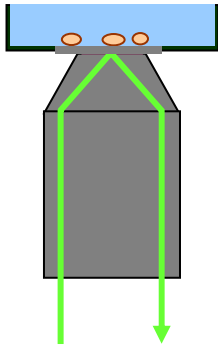


Fig. 2.3 Schematic of through-the-objective type illumination in an inverse microscope.

The specimen placed on top of the (oil-immersion) objective. The laser beam travels through the objective; it is coupled into the beam path in a conjugated plane outside of the microscope, at appropriate distance from the optical axis.

For the through-the-objective type approach, the laser beam is coupled into the same objective which is used for recording fluorescence emission. This method requires high numerical aperture objectives (as the marginal rays have to exceed the critical incidence angle for total internal reflection), and the precise adjustment of the optical pathway is indispensable. The advantage of the method is the fact that fluorescence is collected from the same side of the specimen where it is excited (which reduces scattering), and that this technique is compatible with an inverted setup and with oil-immersion objectives; due to its inherent requirement for high numerical apertures, it produces a higher optical resolution.

2.3 EW calibration of the setup

While in theory, the penetration depth of the evanescent field can be calculated from the incidence angle of the laser beam onto the interface plane, due to relative complexity of the optical system (with multiple reflections, layers of different refracting index and diffraction effects), it is important to independently estimate the depth of field in cell measurement conditions.

This *in vivo* calibration of the evanescent field is performed by a method first proposed by Prof. Axelrod's group at the University of Michigan (Mattheyses and Axelrod,

2002): Large fluorescent beads are settled onto a coverslip and the bead's footprint is recorded. Since the beads are spherical and their diameter is known, the geometry of the fluorophore distribution on the bead's surface close to the interface is well defined. Thus, each point's axial (z -) separation distance from the coverslip can be calculated from its lateral distance from the bead's equator.

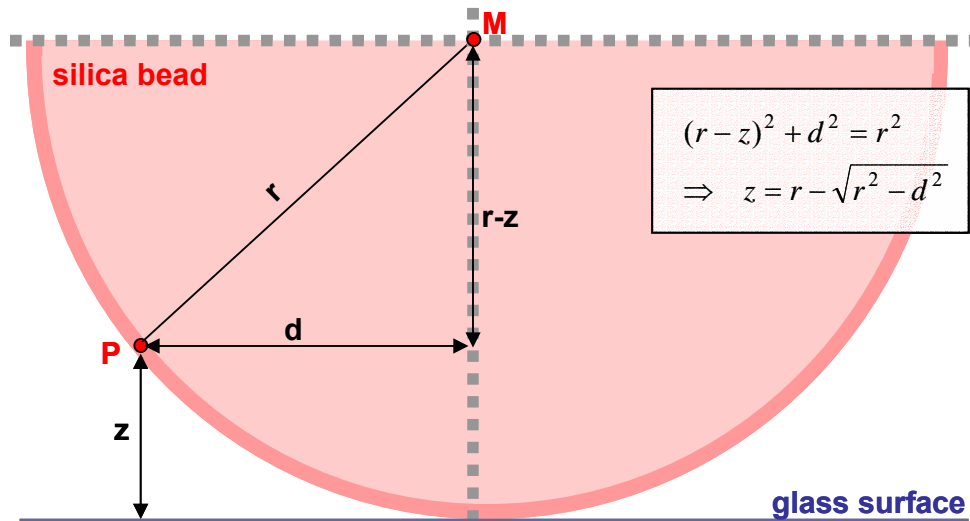


Fig 2.4: Schematic of spherical bead on coverslip, where distance from equator is used to calculate distance from coverslip.

This method doesn't work with conventional fluorescent latex beads, as these have a refractive index approaching that of glass. The high refractive index transforms the evanescent wave in the aqueous medium back into a propagating wave at the water/bead interface (a reverse of the total reflection effect creating the evanescent wave); this sometimes creates whispering-gallery modes* in the bead, and completely destroys the exponential intensity-distance relationship.

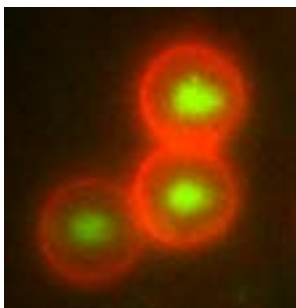


Fig: 2.5: False-colour overlay image of epi-illumination image (red) and TIRF illumination image (green) of 6.6 μ m silica beads coated with Dil. Focus level of epi-image was close to the beads' equator, approximately 3.7 μ m above TIRF focus level at the interface.

* **whispering gallery mode**: a sustained electromagnetic mode in a dielectric sphere that circulates through total internal reflection and is strongly confined within the sphere (see, e.g. Datsyuk, 1992).

Instead, this method uses large ($6.6\mu\text{m}$) silica beads (Bangs Laboratories, Fishers, In, USA), which have a refractive index more closely matched to water ($n=1.36$). As these beads are non-fluorescent, they have to be coated with *DiI* (Sigma-Aldrich, Seelze, Germany). The calibration experiment is performed in a sucrose solution of precisely matched refractive index $n=1.36$ to prevent refraction into the bead, and the calculated d_p value is then corrected for the difference in n to yield the result for aqueous solution ($n=1.33$).

As fig. 2.5 demonstrates, the size and position of the large silica beads can easily be determined in transmission or epi-fluorescence. When the focus is moved to $3\text{-}4\mu\text{m}$ above the coverslip, the full diameter of the beads can be seen as a ring (in red pseudocolor). Focusing to the interface in TIRF illumination, only a small patch of fluorescence is seen in the position where the bead makes contact with the coverslip (green pseudocolor).

The space constant of exponential intensity decay, d_p , is calculated from the plot of distance-dependent intensity from the TIRF images. First, to estimate the center of gravity, the intensity distribution was fitted with a Gaussian; the center of gravity is a reasonable approximation for the precise coordinates of the contact point with the interface (see fig 2.6).

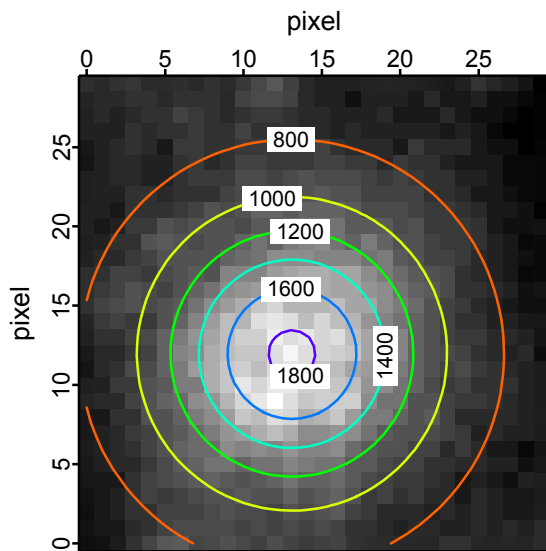


Fig. 2.6: TIRF image of a single bead's footprint. The superimposed Gaussian fit is used to determine the center of gravity; this is used as a reference point for the subsequent distance determination.

Every pixel's lateral (xy -) distance from the contact point was determined; then the axial (z -) distances were calculated geometrically. For this conversion, the bead surface is assumed to be a perfect sphere (fig. 2.4), so that axial distances z are calculated from the

lateral distances d as $z = r - \sqrt{r^2 - d^2}$ (where r represents the known radius of the silica beads, 3.3 μm). The pixel intensity is plotted as a function of distance in figure 2.7.

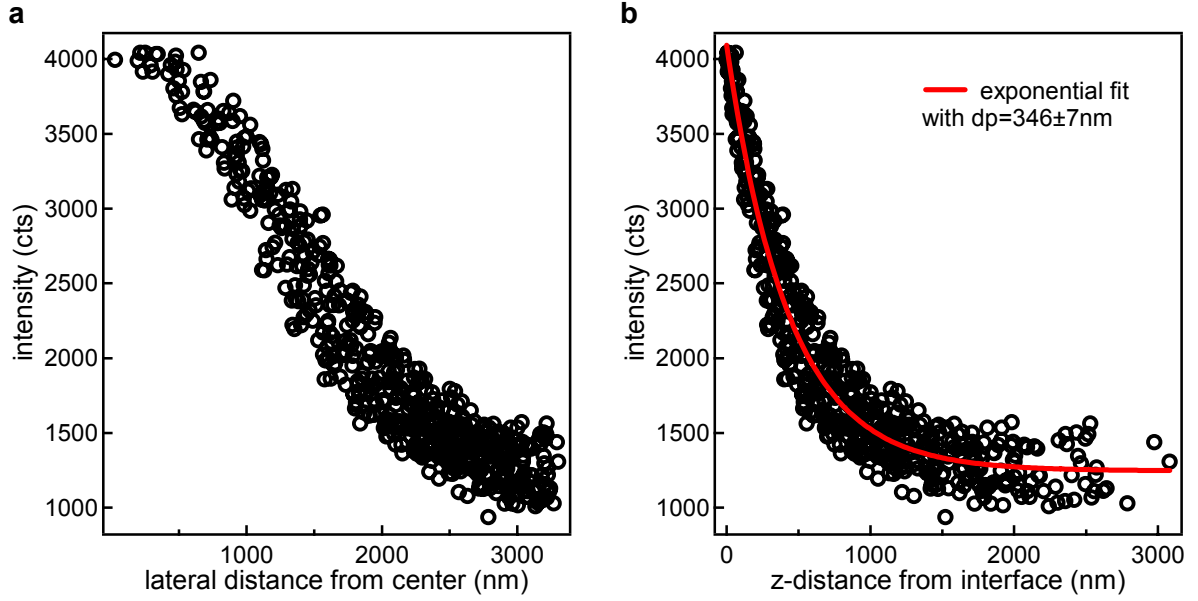


Fig. 2.7: Intensity as function of distance, each point representing the intensity of a single pixel (pixelsize 225nm). a: Intensity as function of lateral distance from center of gravity b: Lateral distances converted to axial distances; an exponential fit yields a space constant of $346 \pm 7\text{nm}$ (in sucrose solution with $n=1.36$)

For conversion into axial distances, fig. 2.7a becomes fig. 2.7b, where the exponential decay of the fluorescence intensity with distance becomes obvious. An exponential fit yields a space constant of $345.8 \pm 7.1\text{ nm}$, which is the penetration depth of the evanescent field in the sucrose solution (of refractive index $n=1.36$). With equation 23, the value of d_p in aqueous medium with $n=1.33$ is calculated from the value for sucrose solution as

$$dp_{aq} = \sqrt{\frac{1}{\frac{1}{dp_{suc}^2} + \frac{16\pi^2}{\lambda^2}(n_{suc}^2 - n_{aq}^2)}}$$

so that the final value for d_p in aqueous medium is $127.1 \pm 2.6\text{ nm}$.

2.4 Photobleaching recovery and diffusion

The basis of the FRAP technique (fluorescence recovery after photobleaching) is the transient strong illumination of a small sub-region of the specimen

which results in the photodynamic blanking (bleaching) of fluorophores in the illuminated volume. After the end of the bleaching pulse, the fluorescence intensity of the bleached region recovers as fluorophores are exchanged between the bleached and surrounding unbleached regions (see fig. 2.8). The speed and time course of recovery are determined by (and thus contain information about) the modes of exchange.

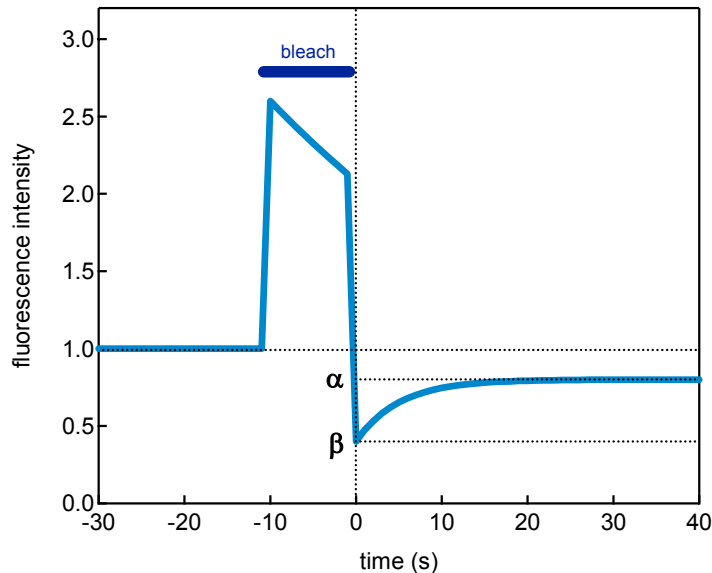


Fig. 2.8: Schematic example of a normalised FRAP trace; during the bleaching pulse, the specimen is illuminated at a high intensity (40x normal recording intensity) but with much shorter exposure time. After the end of the bleaching pulse β , the signal recovers as unbleached material diffuses back into the bleached volume, it reaches a plateau value α .

In this study, the fluorescent clathrin construct in the cell exists in two forms: in freely diffusible form in the cytosol, and in the form of immobile clathrin bound in clathrin pits at the membrane. Thus, in our experiments, the recovery is carried by two different processes, by the diffusion of unbleached molecules into the bleached region, and by the clathrin exchange reaction - i.e. unbinding of bleached clathrin molecules from coats to be replaced by unbleached ones. One of the important tasks of this study is to separate the reaction component from the diffusion component, so that the speed of the exchange reaction can be studied quantitatively.

When considering the exchange reaction (measured as the intensity of the immobile fraction at the membrane), the time course during bleaching looks roughly like figure 2.8. During bleaching, the intensity first increases (due to the illumination at high intensity), and subsequently decays with a time course similar to an exponential function (see paragraph 2.4.2). After the end of the bleaching pulse, when the intensity is returned to pre-bleaching level, pits are found to be bleached to the “bleaching depth” β . From this time point on,

recovery takes place as bleached molecules in the pit are exchanged for unbleached ones from the diffusible fraction.

If there is an unlimited supply of unbleached molecules, the normalised intensity will recover to the value before bleaching (i.e. unity). This is, however, not the case in the experiments here presented, as the cells have a limited volume and thus a noticeable fraction of the diffusible pool is bleached as well. This fraction is, of course, still much smaller than the bleached fraction in the immobile pits, since most of the diffusible pool is out of the range of the evanescent field, and this gradient is the driving force behind the fluorescent recovery measured in the coats. The overall unbleached fraction is termed α , and it denotes the level to which the both the pit fluorescence and the diffusion component will eventually recover for long observation times ($t \rightarrow \infty$), as an equilibrium between fluorescent diffusible and immobile pool is again established.

2.4.1 FRAP Reaction limit

When the surface residency time of the adsorbant is much longer than the time which is required for a diffusible molecule to enter or leave the vicinity of the observed surface area, the process is in the “reaction limit”. This condition is a prerequisite for the reaction speed not to be limited by the speed of diffusion. In the reaction limit for large illuminated area in TIRF-FRAP, fluorescence recovery depends only on k_{off} (desorption rate), and the time course of recovery is exponential. If the opposite relation is true, the process is said to be in “diffusion limit”, where the recovery time course depends only on D and the equilibrium concentrations.

The surface residency time of the adsorbant is

$$\tau = 1 / k_{off} ,$$

where k_{off} is the off-rate of the binding reaction (i.e. the unbinding rate)..

The bulk diffusion time relates to the minimum time required for unbleached molecules to diffuse through the cytosol to repopulate the sites of bleached molecules at the surface. From the Einstein-Smoluchowski equation ($\bar{x}^2 = 2Dt$), the bulk diffusion time is estimated to be

$$t_{diff} = \frac{\bar{x}^2}{2D} ,$$

where \bar{x} is the characteristic distance which the unbleached molecule travels to the surface, and D is the diffusion coefficient of solute in the bulk. \bar{x} can be approximated as the depth of the cytosol containing the same number of labeled molecules as are bound at the surface. For a surface area S , the number of molecules on the surface is $\bar{C}S$ (where \bar{C} is the equilibrium concentration of surface adsorbed solute). The number of molecules found in the volume $S\ell$ (i.e. within the characteristic distance ℓ of the surface) is $\bar{A}S\ell$ (where \bar{A} is the equilibrium concentration of bulk solute); this number is equal to the number of surface molecules for $\ell = \bar{C} / \bar{A}$ (Thompson et al., 1981).

Thus, for $\bar{x} = \ell = \bar{C} / \bar{A}$, the bulk diffusion time is

$$t = \frac{(\bar{C} / \bar{A})^2}{2D}.$$

Thus, the reaction limit can be described by the equation

$$\frac{1}{k_{off}} \gg \frac{(\bar{C} / \bar{A})^2}{D}$$

(see Axelrod et al., 1984).

Furthermore, the ratio of surface concentration vs bulk concentration, \bar{C} / \bar{A} , can be approximated from TIRF-FRAP measurements (Sund and Axelrod, 2000). It is calculated from the bleach fraction in the sample of interest as:

$$\frac{\bar{C}}{\bar{A}} \geq \frac{dp \cdot (1 - \alpha)}{(1 - \beta) - (1 - \alpha)}$$

where dp is the penetration depth of the evanescent field ($dp \approx 120nm$), $(1 - \alpha)$ is the bleach fraction in specimen of interest (typically around 0.3 in this study), and $(1 - \beta)$ is the bleach fraction in the immobile adsorbate (measured in membrane sheets as $(1 - \beta) = 0.7$).

Thus, it is calculated that $\ell = \bar{C} / \bar{A} \approx 80nm$; with typical values in this study on the order of $k_{off} \approx 0.05s^{-1}$ and $D = 0.25 \mu m^2 / s$ (Alexey Kochubey, unpublished data), the inequation is

$$\frac{1}{k_{off}} \approx 20s \gg \frac{(\bar{C} / \bar{A})^2}{D_A} \approx 3.2 \cdot 10^{-4} s.$$

Although the inequation holds true, as a note of caution it should be added that the value for $\ell = \bar{C}/\bar{A}$ is only a rough approximation, since in its derivation, a rapid turnover is assumed (Sund and Axelrod, 2000), which neglects to account for the inhomogeneous bleaching of the bulk molecules (treated in detail in paragraph 2.4.4) and the resulting effective variability of the equivalent cytosolic depth ℓ (which must contain not only an equivalent number of fluorophores, but of *unbleached* fluorophores).

However, the amplitude of the diffusive depletion depth is considerably smaller than the reaction depletion (while the absolute diffusion signal amplitude is about 5-fold higher than the corrected reaction signal, see e.g. figure 5.1), and no significant effect of the bleaching duration is seen on the determined desorption rate constant (paragraph 4.1.2). Thus, the magnitude of the reaction rate constant in this study is probably not rate-limited by the speed of diffusion, although the measured reaction signal has to be corrected for the diffusive contribution as described in paragraph 2.4.3.

In a rough estimation from the data in this study, the typical relative contributions are as follows: Let a pit have an arbitrary intensity of about 10 “fluorescence units” pre-bleaching. During the bleaching interval of 10s, the pit will be bleached down to an intensity of about 2 units; in the first 5 seconds after bleaching, on average 2 of the 8 bleached fluorescence units will be exchanged from the pit (due to $\tau \approx 20$ s). The corresponding cytosolic volume accessible by diffusion during this time (a layer of the depth $\bar{x} = \sqrt{Dt/2} \approx 1.5 \mu\text{m}$) contains a total of on the order of 450 diffusible units (both fluorescent and bleached, extrapolated from the evanescent intensity pre-bleaching); the number of fluorescent diffusible units increases (through the relaxation of the local bleaching gradient, see paragraph 2.4.4) from about 400 to 420 during the interval.

2.4.2 Bleaching in the immobile fraction

The time course measured during bleaching in the immobile fraction looks similar to an exponential function, but cannot, in fact, be fitted well with a single exponential. We consider that the intensity signal initiates from fluorophores at different distances from the interface, which are thus subject to different bleaching constants. The initial intensity at the beginning of the bleaching pulse at the different distances is:

$$I(z, t_0) = I(z_0, t_0) \cdot \exp(-z/dp) \cdot C(z)$$

where $C(z)$ represents the local concentration of fluorophore (which is, in a fixed specimen, time-independent).

With the beginning of bleaching, the initial intensity at each distance z decays exponentially with the bleaching constant $k(z)$

$$I(z, t) = I(z, t_0) \cdot \exp(-k(z) \cdot t)$$

The bleaching constant $k(z)$, when we assume it to be proportional to the illuminating intensity, is

$$k(z) = k_0 \cdot \exp(-z / dp)$$

(with dp the space constant of the evanescent intensity decay).

Thus, the distance- and time-dependent intensity for each point is

$$I(z, t) = I(z_0, t_0) \cdot \exp(-z / dp) \cdot C(z) \cdot \exp(-k_0 e^{-z / dp} t)$$

The measured time-dependent intensity $I_m(t)$ during bleaching is the integrated intensity over the entire illumination depth

$$I_m(t) = I(z_0, t_0) \cdot \int_{z=0}^{\infty} \exp(-z / dp) \cdot \exp(-k_0 \cdot e^{-z / dp} t) \cdot C(z) dz$$

With the substitution of $x = \exp(-z / dp)$ and $dz = -(dp / x) \cdot dx$, this equation is modified to

$$I_m(t) = I(z_0, t_0) \cdot \int_{x=1}^0 -dp \cdot \exp(-k_0 x t) \cdot C(x) dx$$

If, as a first approximation, $C(z)$ (and therefore also $C(x)$) are assumed to be constant, the integral can be solved and resubstituted

$$I_m(t) = I(z_0, t_0) \cdot dp \cdot C \cdot \left[\frac{1}{k_0 t} \exp(-k_0 e^{-z / dp} t) \right]_{z=0}^{z=\infty}$$

$$I_m(t) = \frac{I(z_0, t_0) \cdot dp \cdot C}{k_0 t} (1 - \exp(-k_0 t))$$

In order to normalise this function, the value at zero is determined as

$$\begin{aligned} \lim_{t \rightarrow 0} I_m(t) &= \frac{I(z_0, t_0) \cdot dp \cdot C}{k_0} \cdot \lim_{t \rightarrow 0} \left(\frac{1 - \exp(-k_0 t)}{t} \right) = \frac{I(z_0, t_0) \cdot dp \cdot C}{k_0} \cdot \lim_{t \rightarrow 0} (k_0 \cdot \exp(-k_0 t)) \\ &= I(z_0, t_0) \cdot dp \cdot C \end{aligned}$$

Thus, the normalised intensity is

$$I_n(t) = \frac{I_m(t)}{I_m(t=0)} = \frac{(1 - \exp(-k_0 t))}{k_0 t}$$

If the fluorophore distribution is not of infinite depth, but limited (to the cell diameter d)

$$C(z) = \begin{cases} C & 0 \leq z \leq d \\ 0 & z > d \end{cases}$$

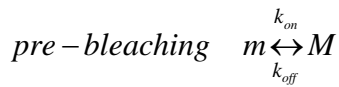
then the above equation for the normalized intensity is modified to

$$I_n(t) = \frac{(\exp(-k_0 x t) - \exp(-k_0 t))}{(1-x)k_0 t} \quad \text{where } x = \exp(-d / dp)$$

so that the normalised function additionally depends on the depth of the distribution d , the evanescent field penetration depth dp , and the bleaching constant k_0 . Thus, both for a finite and for an approximately infinite ($d \gg dp$) extended fluorophore distribution, the shape of the bleaching decay significantly differs from the simple exponential function generated by an infinitely thin layer.

2.4.3 Reaction component of recovery (immobile fraction)

Before bleaching, the system is in an equilibrium of diffusible fluorescent clathrin molecules (m) and molecules bound in clathrin coats (M), where mobile clathrin binds to existing clathrin coats and bound clathrin molecules unbind to return to the mobile cytosolic fraction.



In this case, no further assumptions are made about the fluorescence properties of the coat, or about the exact nature of the fluorescent species. As experiments are done with different clathrin fusion proteins (representing different functional units), and since their association is still a matter of discussion, this very basic model still allows for several different substitutions: that the clathrin molecule (m , M) constitutes light chains (l , L), heavy chains (h , H), or free assembled subunits of the two, e.g. assembled triskelia.

Taking M and m as the respective concentrations, it can be derived that

$$\frac{M}{m} = \frac{k_{on}}{k_{off}} \Rightarrow k_{on} = \frac{M \cdot k_{off}}{m} \quad (\text{equation 25})$$

After bleaching, the entire amount of available clathrin molecules is unchanged and constant, but separated into two optically distinct species, the bleached and the fluorescent subspecies, both in their diffusible form (m_b and m_f) and bound in coats (M_b and M_f).

We assume that both the entire number of coats and concentration of diffusible material stays the same after bleaching, i.e.

$$M = M_b + M_f = \text{const. and}$$

$$m = m_b + m_f = \text{const.}$$

Furthermore, we assume that no further molecules are bleached after the end of the bleaching pulse, so that

$$m_f + M_f = \text{const.}$$

Since in our experiments the concentration of unbound clathrin is at all times much larger than that of bound clathrin ($m \gg M$), and since this also applies to the fluorescent sub-fraction ($m_f \gg M_f$), it is safe to assume that the fraction of bleached unbound clathrin does not change significantly after the end of the bleaching pulse, as the contribution to this pool from molecules partitioning into and out of coats is extremely small, even if its spatial distribution changes as it equilibrates, so that

$$m_f + M_f = \text{const.} \approx m_f$$

Therefore, we approximate

$$\frac{m_f(t)}{m} \approx \frac{m_f(t=0)}{m} = \text{const.} \equiv \alpha \quad (\text{equation 26})$$

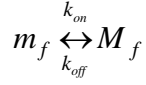
Thus, the value α , which is the overall fluorescent fraction, can be approximated as the fraction of diffusible molecules which are still fluorescent after bleaching (under the assumption that the entire amount of diffusible molecules is much larger than the amount of bound ones) (see fig.2.8).

Additionally, we set

$$\frac{M_f(t=0)}{M} \equiv \beta, \quad (\text{equation 27})$$

where β is the fraction of fluorescent coat molecules immediately after bleaching.

For the fluorescent fraction of clathrin, the reaction equation holds true in the form



Therefore

$$\begin{aligned} \frac{d}{dt} M_f &= k_{on} m_f - k_{off} M_f \quad (\text{substitute equation 25}) \\ &= \frac{M \cdot k_{off}}{m} \cdot m_f - k_{off} M_f \end{aligned} \quad (\text{equation 28})$$

Substituting equation 26 into equation 28 yields:

$$\frac{d}{dt} M_f = k_{off} \alpha M - k_{off} M_f$$

so that

$$\frac{d}{dt} \frac{M_f}{M} = k_{off} \alpha - k_{off} \frac{M_f}{M}$$

An exponential approach to this differential equation yields:

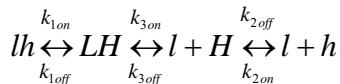
$$\frac{M_f(t)}{M} = \alpha + g \cdot e^{(-k_{off} \cdot t)} \quad (\text{with } g \text{ a constant factor})$$

With the condition $\frac{M_f(t=0)}{M} \equiv \beta$ as in equation 27, then $g = (\beta - \alpha)$, so that

$$\frac{M_f(t)}{M} = \alpha + (\beta - \alpha) \cdot e^{(-k_{off} \cdot t)}$$

This predicts an exponential recovery for the (normalised) intensity of bleached pits if the exchange reaction is a single pathway.

If we now look into more detail about our fluorescent species, and consider that we have experiments with two fluorescent species (heavy chain and light chain) involved in this reaction. This produces a slightly more complicated pathway, as we propose that clathrin heavy chain and light chain do not necessarily exchange as a unit, but that heavy chain can exchange via a light-chain dependent, and via a light-chain-independent pathway:



(where l and h are the diffusible forms, and L and H the bound forms of clathrin light and heavy chain).

In an experiment where clathrin heavy chain is the fluorescent species, the observed pit fluorescence is the sum of both bound “species” of heavy chain, i.e. the light-chain-bound and unbound fraction LHC and HC. In this case

$$\begin{aligned}\frac{d}{dt}M_f &= \frac{d}{dt}(LH_f + H_f) = \frac{d}{dt}(LH_f) + \frac{d}{dt}(H_f) \\ &= k_{1on}(lh_f) - k_{1off}(LH_f) - k_{2off}(H_f) + k_{2on}(h_f)\end{aligned}$$

The solution of this equation is analogous to the solution to the simple equation. If we assume that the two species of heavy chain (bound and unbound to light chain) have essentially the same bleaching characteristics, so that their relative level of bleaching is equally strong, then the recorded fluorescence intensity for pits is

$$\begin{aligned}\frac{M_f}{M}(t) &= \frac{LH_f(t) + H_f(t)}{LH + H} \\ &= \alpha + g_1 \cdot (\beta - \alpha) \cdot e^{-k_{1off} \cdot t} + g_2 \cdot (\beta - \alpha) \cdot e^{-k_{2off} \cdot t}\end{aligned}$$

where $g_1 = \frac{LH}{LH + H}$ and $g_2 = \frac{H}{LH + H}$ so that $g_1 + g_2 = 1$

As can be seen from this equation, the solution is a combination of two exponential recovery components. The relative amplitude contributions of the two exchange rates k_{1off} and k_{2off} are determined by the relative fraction of light-chain-bound or unbound clathrin in the entire clathrin heavy chain concentration in the pits.

As will be seen in the results chapter, this model predicts that when the equilibrium between endogenous light chain and heavy chain concentration is shifted (by the overexpression of the fluorescent heavy chain construct, which selectively increases heavy chain concentration), the contribution of the second exponential to the solution becomes higher as its amplitude increases.

In the same multiple-step model as above, the differential equation for the recovering fluorescence intensity of clathrin light chain is

$$\frac{d}{dt}(L_f H) = k_{1on}(l_f h) - k_{1off}(L_f H) - k_{3on}(L_f H) + k_{3off}(H) \cdot (l_f)$$

$$\frac{d}{dt} \frac{(L_f H)}{(LH)} = k_{1off} \alpha - k_{1off} \frac{(L_f H)}{(LH)} - k_{3on} \frac{(L_f H)}{(LH)} + k_{3on} \alpha$$

so that the solution can be recalculated to

$$\begin{aligned} \frac{M_f}{M}(t) &= \frac{(LH_f)(t)}{(LH)} \\ &= \alpha + (\beta - \alpha) \cdot e^{-(k_{1off} + k_{3on})t} \end{aligned}$$

2.4.4 Diffusion (mobile fraction)

The measured signal from the pits is “contaminated” by the fluorescence signal of the mobile fraction, and an aim of experimental design is to correct the pit signals for diffusion to permit a quantitative determination of the time course.

Additionally, we want to study the diffusible fraction in the cell both during bleaching and during recovery to gain additional information about the underlying processes in the cell.

The entire concentration of diffusible fluorescent molecules is conserved in the cell during and after bleaching; however, the concentration c of fluorescent molecules is changed by bleaching and the diffusive redistribution (c corresponds to m in the previous paragraph). In order to determine the shape of the fluorescent profile $c(z)$ for fixed time points, and the decay and recovery of the intensity with time at fixed locations $c(t)$, solutions of the form $c(z, t)$ need to be found.

In a simplified model, the membrane-adjacent region of the cell is assumed to be one surface side of a plane sheet (where the thickness l of the sheet corresponds to the axial diameter of the cell).

The diffusion equation is

$$\frac{\partial c}{\partial t} = D \frac{\partial^2 c}{\partial z^2} \quad (\text{equation 29})$$

where the reflection condition is $\frac{\partial c}{\partial z} = 0$ for $z = 0$ and for $z = l$ in a plane sheet.

The loss of fluorescence by bleaching during the bleaching interval is (with k the bleaching constant)

$$\frac{\partial c}{\partial t} = k \cdot c$$

so that taken together $\frac{\partial c(z,t)}{\partial t} = k(z) \cdot c(z,t) + D \frac{\partial^2 c}{\partial z^2}$

For exponential bleaching in the evanescent field with $k(z) = k_0 \cdot \exp(-z/dp)$, the differential equation cannot be solved analytically. This problem was approached in two steps: First, solutions were calculated numerically in an iterative simulation, allowing for the distance-dependent exponential function $k(z) = k_0 \cdot \exp(-z/dp)$ (initial macro written by Dr. Jürgen Klingauf). Secondly, on the basis of the numerical results, appropriate conditions were found for which $k(z)$ can be approximated by a distribution of the form

$$k(z) = \begin{cases} k' & z = 0 \\ 0 & z > 0 \end{cases}$$

which permits an analytical solution.

Bleaching and recovery simulation:

In the simulation, the observed space is divided into small time and space bins, so that $c(t, z) = c(t_m, z_n) = c_{m,n}$, where $z_{n+1} = z_n + \Delta z$ and $t_{m+1} = t_m + \Delta t$ ($\Delta z = 0.1 \mu\text{m}$ and $\Delta t = 10-40 \text{ ns}$) for which concentrations $c_{m,n}$ are calculated in subsequent small time steps, with the appropriate boundary and bleaching conditions observed. The concentration in each bin is calculated from its initial value as:

$$c_{m+1,n} = c_{m,n} + \Delta t \cdot (\Delta c_{m,n} / \Delta t)$$

where $(\Delta c_{m,n} / \Delta t)$ is the increase/decrease per time unit caused by bleaching and by diffusion from neighbouring bins:

$$\frac{\Delta c_{m,n}}{\Delta t} = -k_n c_{m,n} + D \frac{((c_{m,n+1} - c_{m,n}) + (c_{m,n-1} - c_{m,n}))}{\Delta z^2}$$

In the bleaching term $k_n = k_0 \cdot e^{-z_n/dp}$, and in the diffusion term (derived from eq. 29) only the concentration of the immediately adjacent neighboring bins ($c_{m,n-1}, c_{m,n+1}$) is considered for the calculation.

In addition to the exponential bleaching, another simulation was performed for constant bleaching in a limited sheet, where the bleaching constant has a rectangular profile (see fig. 2.9), so that $k(z) = k_c$ for $0 < z < r$. The variable parameters in both types of simulation were D (diffusion coefficient), k_0 and dp (which determine the local bleaching intensity), and l , the thickness of the plane sheet. For a calculation of $c(t)$, the intensities $c_{t,n}$ for all z_n were integrated to yield the “measured” signal.

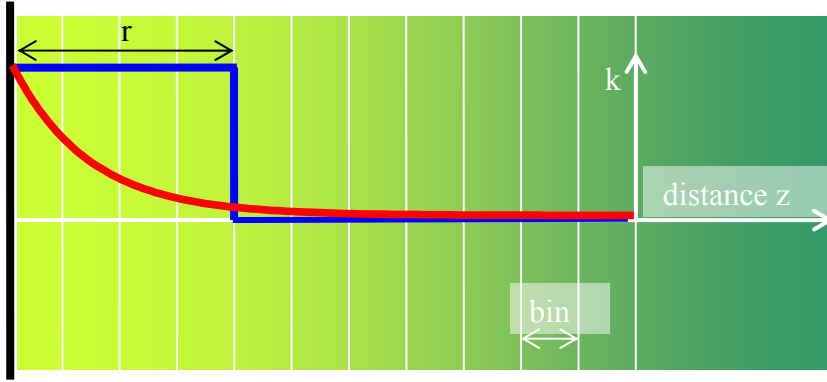


Fig. 2.9: Schematic of bleaching constant (k) profile. In the simulation, space is partitioned into bins of constant size. The bleaching constant can be set as exponential decay function (red) or as rectangular function (blue).

The results of the simulation show that it is possible to obtain solutions $c(z, t) = c(z_n, t_n)$ from rectangular bleaching that are virtually identical to the solutions for exponential bleaching, if r , the length of the rectangular profile is chosen appropriately (see figure 2.11). The condition for the parameter l is that the rectangular “bleaching integral”

$$K_{rec}(r) = \int_0^r dz k_c$$

have approximately the same value as the exponential bleaching integral

$$K_{exp} = \int_0^{\infty} dz k_0 \cdot \exp(-z/dp).$$

Thus, the condition becomes

$$r = (k_0 \cdot dp) / k_c$$

This condition is demonstrated in figure 2.10, where the exponential decay profile and two corresponding rectangular profiles are shown. For one rectangular profile, $k_c = k_0$, so that the length has to be $r = dp$, for the other $k_c = 5 \cdot k_0$ and $r = dp/5$. The resulting solutions

$c(t)$ for the different bleaching conditions during a 10s bleaching interval and 120s of recovery are shown in figure 2.11.

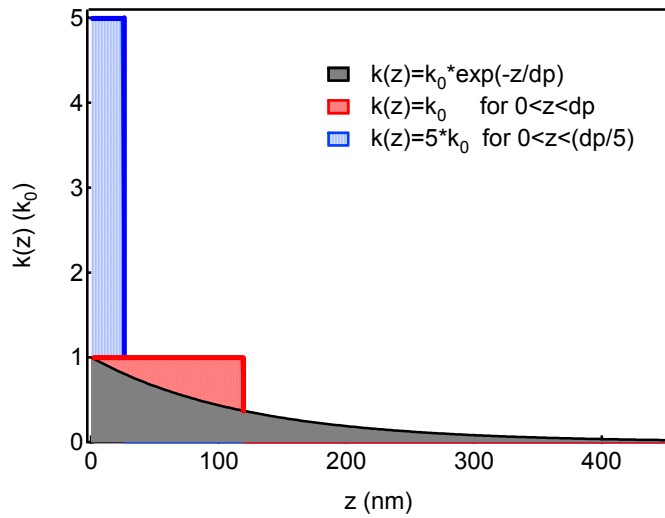


Figure 2.10: Approximation of the exponential volume profile by a rectangular profile bleaching.

Similar solutions for the concentration $c(z,t)$ are obtained for exponential bleaching (grey) and rectangular bleaching profiles (red and blue) if the covered area

$$A = \int_0^{\infty} k(z) dz$$

is equal.

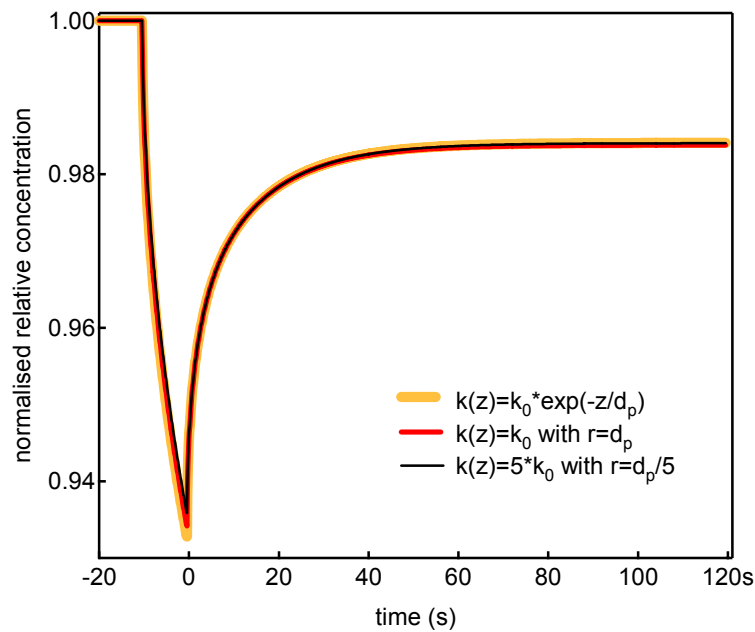


Figure 2.11: Simulated bleaching recovery time course for exponential and rectangular bleaching profiles.

Bleaching interval is 10s, $D=0.25\mu\text{m}^2/\text{s}$, $l=6\mu\text{m}$, $k_0=0.1$, $dp=100\text{nm}$. The bleaching and recovery traces are virtually identical for exponential and rectangular bleaching profiles.

The results demonstrate that it is possible to approximate exponential bleaching well with rectangular bleaching with appropriate values of r and k_c . Thus, by making the length r of the rectangle progressively smaller (i.e. decreasing the thickness of the layer where bleaching takes place), while at the same time increasing the value of k_c , it is possible to approximate infinitesimal layer thickness (where the matching value for k_c converges to $k_c = dp \cdot k_0$). This situation is physically equivalent to surface bleaching, and for these boundary conditions, analytical solutions of the diffusion equation have been derived (Crank, 1975; Carslaw and Jaeger, 1978).

Analytical solution of the diffusion equation:

For surface bleaching, the diffusion equation holds true as in equation 29; for the bleaching, the condition is

$$-D \frac{\partial c}{\partial x} = k \cdot c \text{ at the evaporation surface; the initial concentration is } c(x, t = 0) = c_0$$

Assuming the cell approximates a plane sheet (where the sheet thickness l corresponds approximately to the cell diameter), according to (Crank, 1975), the solution for a plane sheet with $-l < x < l$, where the impermeable surfaces are located at $x = \pm l$ and the surface evaporation takes place at $x = \pm l$, is

$$\frac{c_0 - c}{c_0}(x, t) = 1 - \sum_{n=1}^{\infty} \frac{2L \cos(\beta_n \cdot x/l) e^{-\beta_n^2 D t / l^2}}{(\beta_n^2 + L^2 + L) \cos \beta_n}$$

where β_n positive roots of $\beta_n \cdot \tan \beta_n = L$, $L = l \cdot k_v / D$

This solution is equivalent to the situation with a plane sheet with $0 < x < l$, where the impermeable surfaces are located at $x = 0$ and $x = l$, and where the surface evaporation takes place at $x = l$. We define $x = (l - z)$, so that for the system in this study

$$\frac{c_0 - c}{c_0}(z, t) = 1 - \sum_{n=1}^{\infty} \frac{2L \cos(\beta_n \cdot (l - z)/l) e^{-\beta_n^2 D t / l^2}}{(\beta_n^2 + L^2 + L) \cos \beta_n}$$

The diffusive redistribution of material after bleaching in the plane sheet, i.e. the diffusive recovery, is described by:

$$c(z, t) = \frac{1}{l} \int_0^l f(z') dz' + \frac{2}{l} \sum_{n=1}^{\infty} e^{-D n^2 z^2 t / l^2} \cos \frac{n \pi z}{l} \int_0^l f(z') \cos \frac{n \pi z'}{l} dz'$$

where $f(z)$ is the initial distribution at the end of the bleaching interval (i.e. the bleached concentration gradient).

Figure 2.12 **a** shows the spatial profile of the evanescent field, together with several calculated functions $f(z)$ in a 6 μm plane sheet for different bleaching intervals ($D=0.25\mu\text{m}^2/\text{s}$, $k_0=0.11$). The graph demonstrates that even for short bleaching times ($<10\text{s}$), the concentration gradient extends over multiple penetration depths into the plane sheet. In figure 2.12 **b**, the time courses of recovery in the plane sheet are plotted, after the different bleaching intervals as in **a**. They show that after the end of the bleaching pulse, the diffusion

signal requires tens of seconds to reach plateau value in a $6\mu\text{m}$ plane sheet, even for bleaching intervals below 10s; for thicker sheets, the time until equilibrations is even longer.

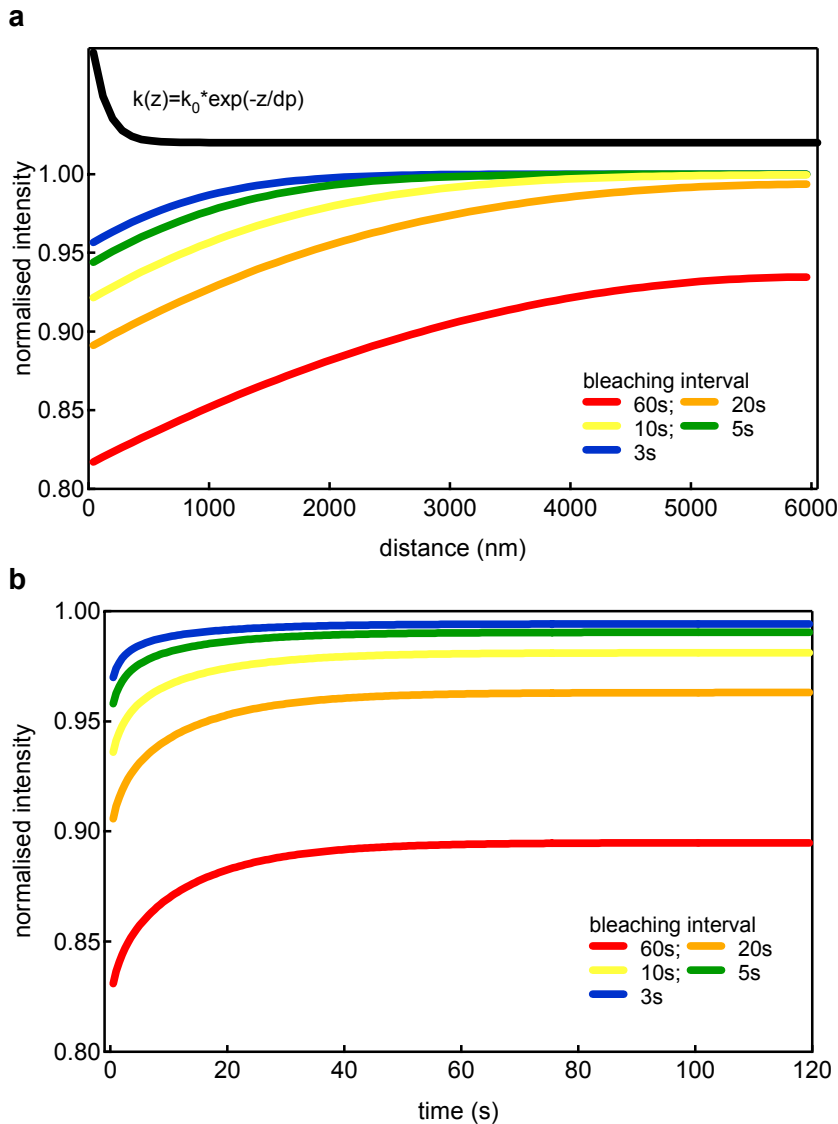


Fig.2.12: Bleaching and recovery for different bleaching intervals

a: Spatial profiles calculated for varying bleaching intervals in a plane sheet of $6\mu\text{m}$. Black trace indicates shape of evanescent bleaching profile.

b: Recovery of intensity signal after bleaching for varying bleaching intervals as in a.

2.5 FRAP experiment design and analysis

In principle, FRAP experiments consisted of recording the pre-bleach intensity at low laser power, then bleaching at high laser power, and recording the recovery at low power again. Recovery was recorded over typically 2 min at 2Hz, and a slight drift of the focus over this time scale was sometimes observed; in order to make a very basic drift correction possible, the experiment had a time window for refocus after the recovery, after which another 10 images were recorded.



Fig. 2.13: Schematic of FRAP experiment.

Operations that were performed between the bleaching and recovery recording time series included opening/closing the laser shutter (which is open during bleaching, and shuttered for individual images during recording), adding/removing the neutral density filter in the beam path (to switch between high intensity during bleaching and low recording intensity), and loading a new acquisition file (containing the exposure time of the image acquisition). Different exposure times during bleaching and recovery recordings were necessary because it is not possible to reproducibly modify the camera intensification during the course of an experiment; thus image acquisition during recovery was performed with approximately 450ms exposure time to maximize signals, and to prevent chip saturation, shorter exposure times (10-50ms) were used to record the intensity during high intensity bleaching.

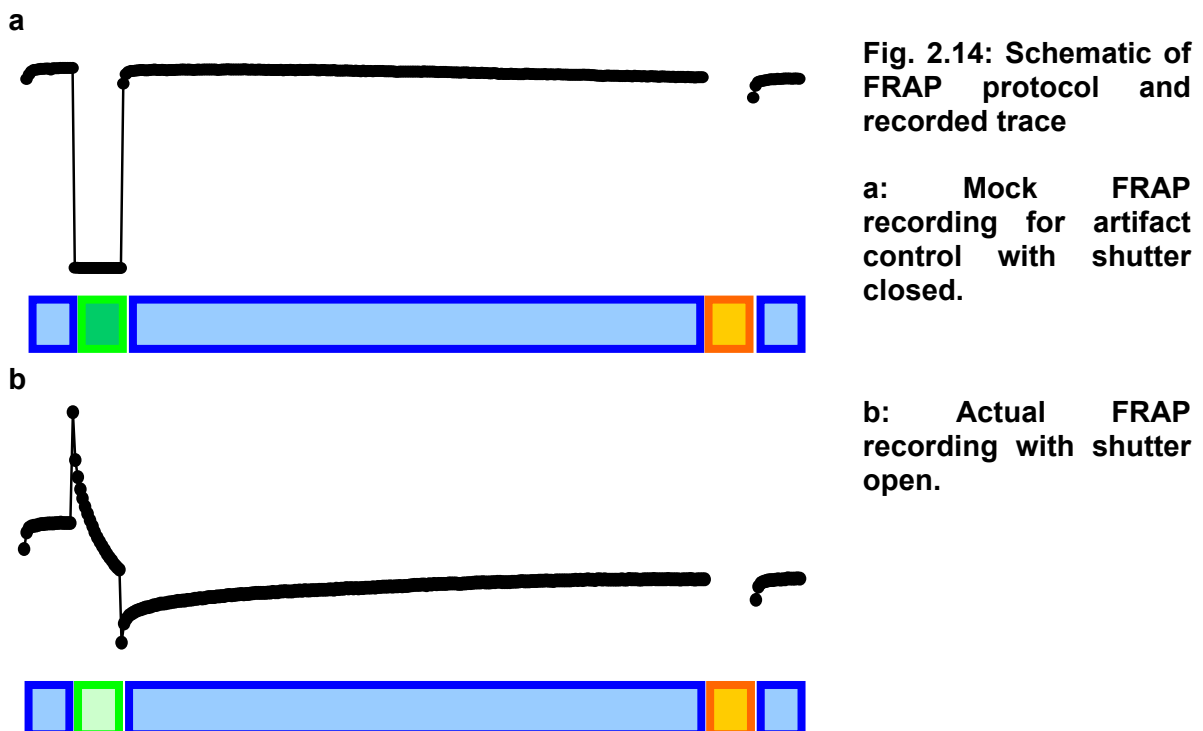


Fig. 2.14: Schematic of FRAP protocol and recorded trace

a: Mock FRAP recording for artifact control with shutter closed.

b: Actual FRAP recording with shutter open.

To control for an electronic artefact (which reduced the intensity at the beginning of a new timelapse, mimicking a small recovery signal), every recorded trace also included an initial “mock” FRAP sequence with the laser shutter closed during the bleaching interval (thus without illumination of the specimen), followed by the “real” recording with the shutter open (see figure 2.14). The measured traces shown in figure 2.14 are the average of $n=20$

original uncorrected measured traces (intensity measured in a small region of interest), where the signal is composed of reaction and the diffusion component.

2.5.1 Single clathrin pits

Figure 2.15 shows an example of a putative single clathrin coated pit (in an experiment with clathrin LCA1-GFP construct). The (x,y) intensity distribution of a sub-resolution fluorescent structure is expected to be a Lorentzian function (Sund et al., 1999)

$$f(x, y) = b + A \cdot \frac{(hw/2)^2}{(hw/2)^2 + (x - x_0)^2 + (y - y_0)^2}$$

where b is background offset, A is maximum amplitude, hw is halfwidth (full-width-half-maximum), and (x_0, y_0) is the position of maximum, so that $f(x_0, y_0) = b + A$.

a

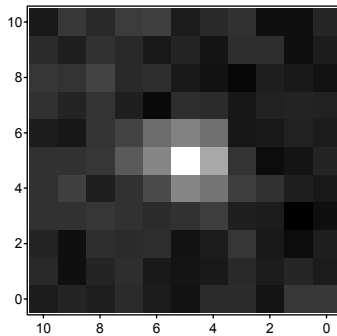
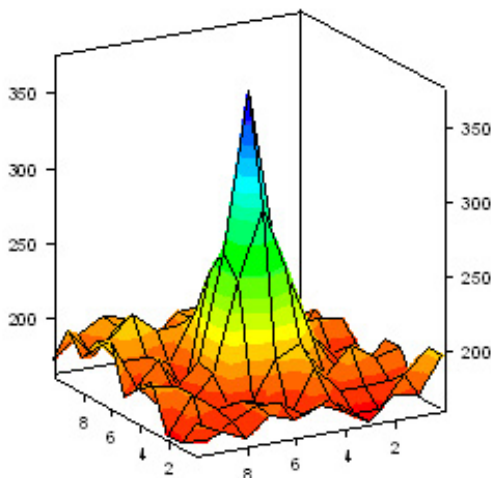
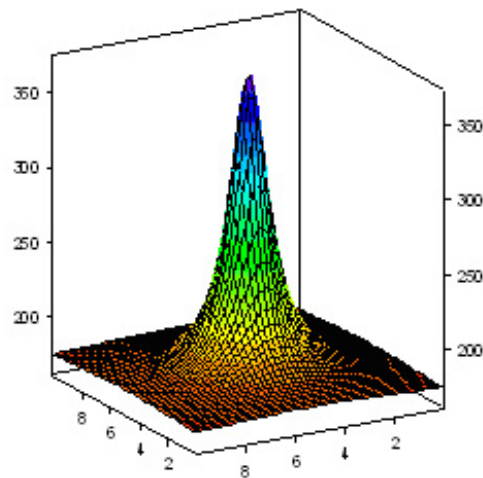


Figure 2.15: a: Original image of putative single clathrin coated pit (clathrin light chain fusion construct), pixelsize is 225nm. b: Surface plot of clathrin pit in a. c: Surface plot of Lorentzian fit to pit intensity; full-width-half-maximum of fit is $hw=2.10 \pm 0.39$ pixels.

b



c



The pit is fitted with the above Lorentzian function, and the surface plot of the original intensity trace and the Lorentzian fit are shown in fig. 2.15 **b** and **c**. The resulting halfwidth of the fitted Lorentzian is $hw=2.10\pm 0.39$ pixel; this value agrees well with the Lorentzian halfwidth measured for a sub-resolution quantum dot (Jürgen Klingauf, personal communication), which is $hw=2.04\pm 0.06$ pixel. This result supports the idea that the size of typical clathrin-coated pits in our experiments is below or close to the diffraction limit of resolution, which is

$$r_{\min} = 1.22 \cdot \frac{\lambda}{NA}$$

according to Rayleigh's criterion, where λ is the light wavelength and NA is the numerical aperture of the objective. For our values of $\lambda=520\text{nm}$ (emission maximum of the GFP fusion construct) and $NA=1.45$, the resolution limit is on the order of $r_{\min} = 440 \text{ nm}$, which leads us to conclude that the typical size of clathrin pits in our experiments does not far exceed 500nm.

2.5.2 Separation of components

The signal recorded in a region of interest (*ROI*) on a clathrin pit is made up of the reaction component originating in the actual pit, and a diffusion signal from the cytosol surrounding the pit. As the pit is a subresolution structure and diffusion takes place all around it, the diffraction images of the pit and of cytosolic diffusive light sources overlap, so that even using a very small region (e.g. a single image pixel) for recording the pit cannot exclude cytosolic contributions. Thus, to correct for diffusion, the local diffusive background (recorded in a ring around the pit) is subtracted from the pit signal to yield the pure reaction component. For this purpose, the intensity is recorded in a circular region of interest (*ROI1*, area n_1 pixels), and in a slightly larger region (*ROI2*, area n_2 pixels), so that the ring intensity (*ROIring*) is the difference of the integrated intensity of the two regions (*ROI2-ROI1*) (see figure 2.16). Both regions are considerably larger than the physical size of the pit, in order to include multiple diffraction orders.

Both the ring and central pit intensities are then divided by the number of pixels in the respective *ROI*, (n_2-n_1) or n_1 , to yield the per-pixel diffusion contribution.

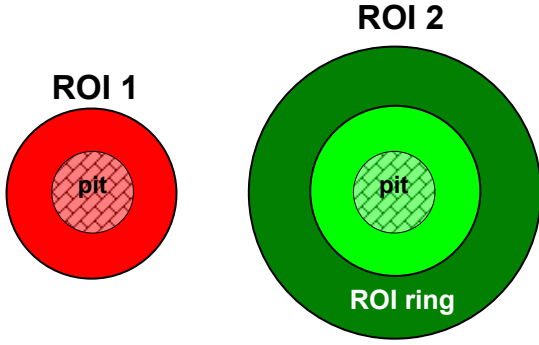


Figure 2.16: Two regions placed over the clathrin pit to record intensity: Smaller region (ROI1, red) is used to record pit intensity; larger region (ROI 2, green) is used to calculate local diffusive background, where ROI2-ROI1=ring (dark green).

The basis for our separation of diffusive and reaction component is the assumption that the per-pixel signal measured in the regions $ROI1$ ($i_1(t)$) and in $ROIring$ ($i_r(t)$) is a linear combination of the diffusion contribution, $d(t)$, and reaction contribution $r(t)$:

$$i_1(t) = bg(t) + a_1 \cdot r(t) + b_1 \cdot d(t) \text{ and}$$

$$i_r(t) = bg(t) + a_2 \cdot r(t) + b_2 \cdot d(t)$$

where $bg(t)$ is a background offset (which can be measured in a region outside the cell). We set $a_1 + a_2 = 1$ and assume that $a_1 \gg a_2$ (reflecting the fact that most of the reaction signal is concentrated in the central region) and that $b_1 = b_2 = 1$ (meaning that the average per-pixel diffusion contribution is the same in the ring and in the central pit).

The difference signal of the two regions is $(i_1(t) - i_r(t)) = (2a_1 - 1) \cdot r(t)$

$$\text{so that } r(t) = \frac{(i_1(t) - i_r(t))}{(2a_1 - 1)}.$$

Similarly, the sum of the two regions is $(i_1(t) + i_r(t)) = 2bg(t) + r(t) + 2d(t)$

$$\text{so that } d(t) = i_r(t) \left(\frac{1}{2} + \frac{1}{2(2a_1 - 1)} \right) + i_1(t) \left(\frac{1}{2} - \frac{1}{2(2a_1 - 1)} \right) - bg(t).$$

Thus, the diffusion signal and the diffusion-corrected reaction signal can be calculated from the measured intensity in the central region and the ring.

The sizes of the $ROIs$ chosen for the pit and the background diffusion recording are a compromise between a good signal-to-background ratio (which requires large regions to include the outer fringes of the diffraction image of the subresolution pit), and reasonable statistics: Most of the punctuate spots are clustered closely together, so that, in order to record a large number of pits per cell, the regions have to be small enough to not overlap too much with neighbouring spots. The relative reaction contribution to the central region (a_1) can be estimated from the region sizes and the Lorentzian distribution width calculated in

figure 2.15. The *ROI* sizes used in this study are shown in figure 2.17; they are, due to the pixellation of the image, not perfectly circular. If we calculate a median radius \bar{r} of the regions as

$$\bar{r} = \sqrt{\text{area} / \pi} ,$$

then the mean radius of the central (red) region is

$$\bar{r}_{ROI1} = \sqrt{29 / \pi} \text{ pixels} = 3.04 \text{ pixels}$$

and that of the green region

$$\bar{r}_{ROI2} = \sqrt{51 \cdot \pi} \text{ pixels} = 4.03 \text{ pixels} .$$

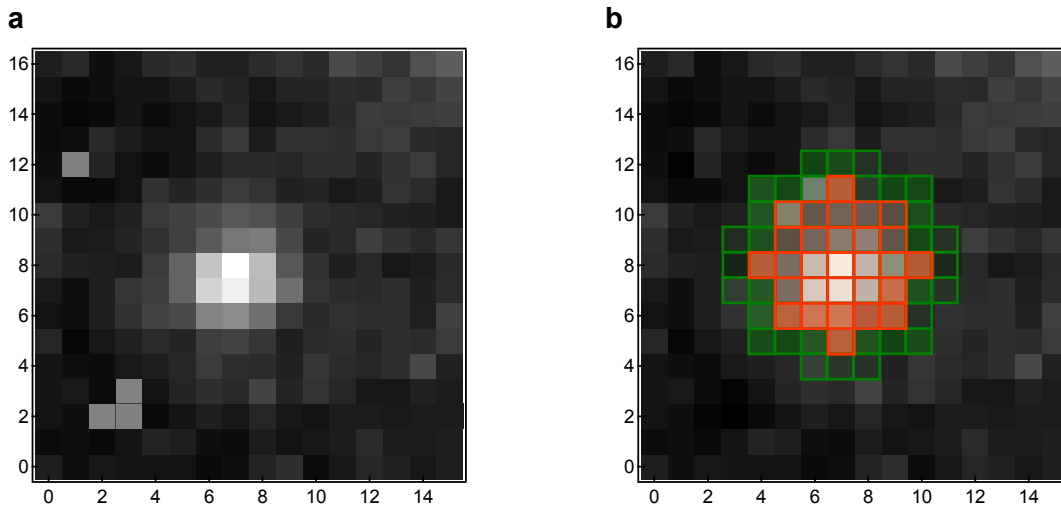


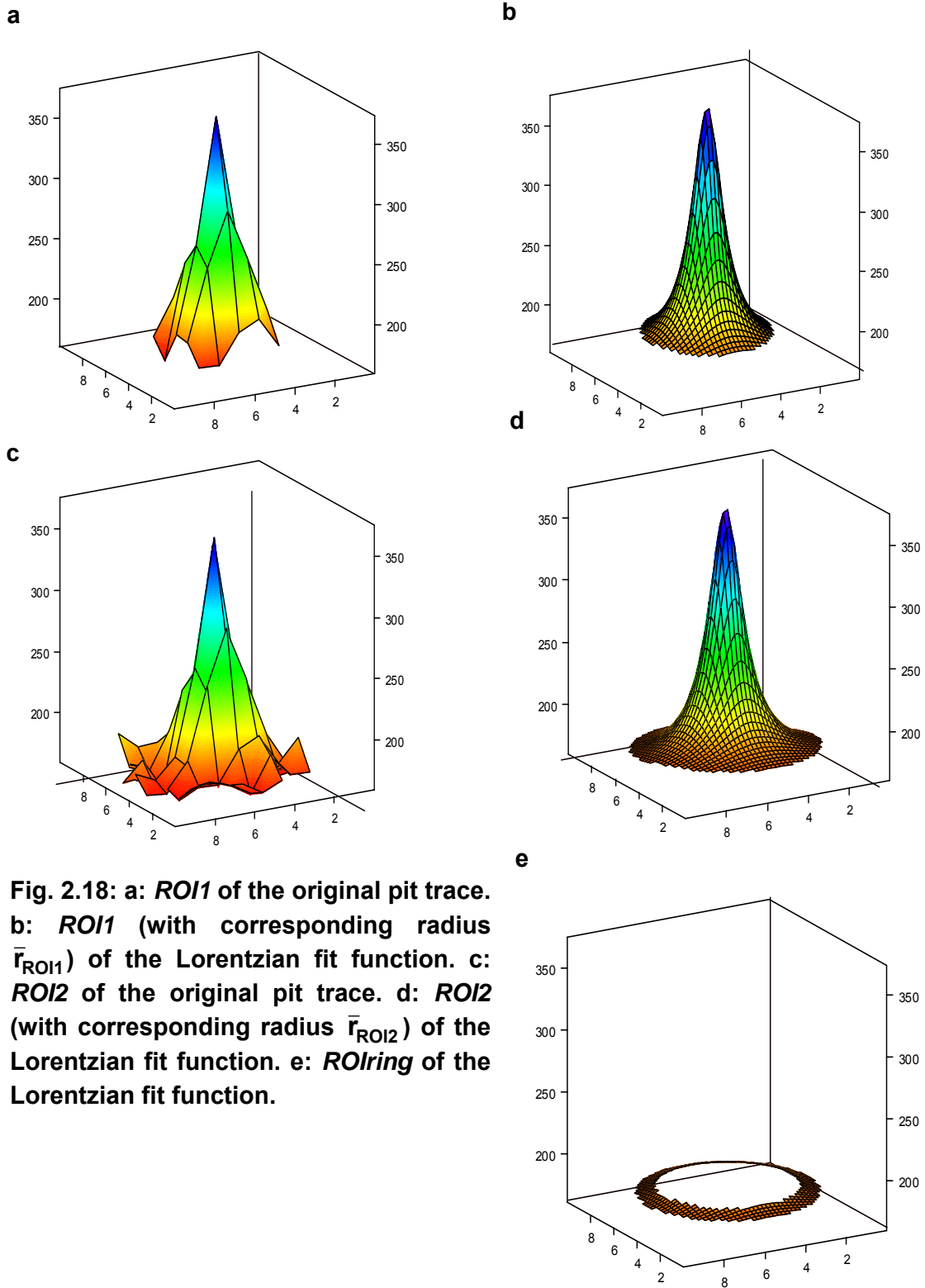
Fig. 2.17: a: Image of single clathrin pit. b: The central red region (29 square pixels) records pit intensity, the green ring around the pit (51-29=32 square pixels) is used to calculate local diffusive background (per pixel). Pixel size is 225nm.

The resulting subregions of the surface plot of the pit signal are shown in fig. 2.18. As can be seen on the graphs, the amplitude of the pit has dropped to close to background level at the radius limiting the central pit readout region. For the specified radii of the regions shown in the graph above, the amplitude of the pit's Lorentzian function has dropped to 8.5% of its maximum value at the ring's middle diameter.

To estimate the central pit's contribution of the outer ring region, we consider the above Lorentzian function, but with normalised amplitude and centered at the origin

$$f(x, y) = \frac{s^2}{s^2 + x^2 + y^2} \text{ where } s^2 = (hw/2)^2$$

and its integral $\iint_{x,y} \left(\frac{s^2}{s^2 + x^2 + y^2} \right) dx dy .$



To integrate the intensity over a circular area, the integral is transformed to polar coordinates $(r = \sqrt{x^2 + y^2}, \varphi)$, so that the integral up to a particular radius R is

$$I(R) = \iint_{r,\varphi} f(r \cos \varphi, r \sin \varphi) \left| \frac{dx}{dr} \frac{dy}{d\varphi} - \frac{dx}{d\varphi} \frac{dy}{dr} \right| dr d\varphi = \int_{r=0}^R \int_{\varphi=0}^{2\pi} \left(\frac{s^2 \cdot r}{s^2 + r^2} \right) dr d\varphi$$

$$I(R) = 2\pi s^2 \cdot \int_{r=0}^R \left(\frac{r}{s^2 + r^2} \right) dr$$

With $\int (x/(a^2 + x^2)) dx = (1/2) \cdot \ln(a^2 + x^2)$ (Bronstein et al., 2000), the integral is

$$I(R) = 2\pi s^2 \cdot \left[\frac{1}{2} \ln(s^2 + r^2) \right]_{r=0}^{r=R} = \pi s^2 \cdot \ln((s^2 + R^2)/s^2). \quad (\text{equation 30})$$

This result shows that, although the shape of the diffraction image of a subresolution structure in EW illumination is approximated well by a Lorentzian function, this approximation has the drawback that its integral (unlike the integral of a Gaussian function) does not converge to a limited value for $R \rightarrow \infty$.

If we therefore set the integrated intensity of the larger region (*ROI2* with mean radius $\bar{r}_2 = 4.03$) as unity, then the smaller central region (*ROI1* with $\bar{r}_1 = 3.04$) contains

$$\frac{\ln((s^2 + \bar{r}_1^2)/s^2)}{\ln((s^2 + \bar{r}_2^2)/s^2)} = 0.82$$

i.e. 82% of the total integrated pit signal (calculated from eq. 30), for $s^2 = (hw/2)^2$, where $hw = 2.10$ pixels as in figure 2.15. Thus, the ring contains approximately 18% of the integrated pit signal. Correcting these values for the different number of pixels in each of the regions (29 pixels in *ROI1*, 32 pixels in *ROIring*) yields the relative per-pixel contribution of the central region $a_1 = 0.83$.

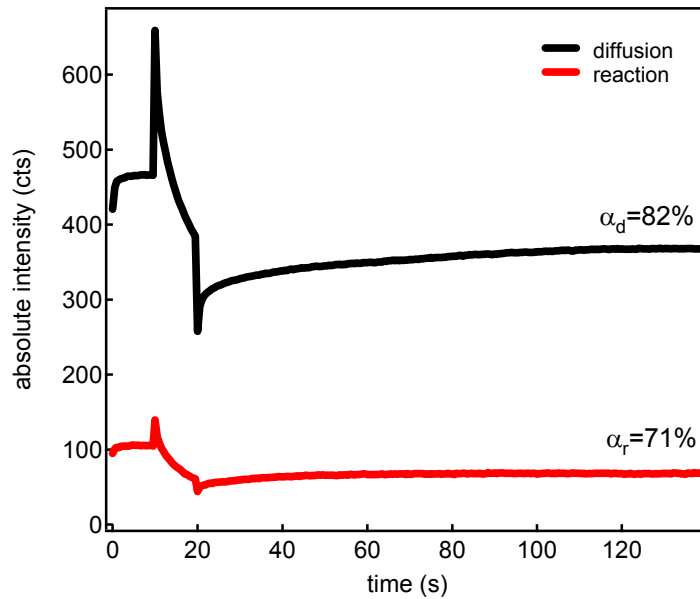


Fig. 2.19: Absolute intensity (per pixel) of separated reaction signal (red) and diffusion signal (black). Traces averaged over $n > 100$ cells. Magnitude of diffusion signal is higher by a factor of approximately 5 than reaction signal.

Thus, the equations for the per-pixel intensities of the regions are modified to

$$i_1(t) = bg(t) + 0.83 \cdot r(t) + d(t) \text{ and}$$

$$i_r(t) = bg(t) + 0.17 \cdot r(t) + d(t)$$

so that $r(t) = (i_1(t) - i_r(t))/0.66$ and $d(t) = 1.25 \cdot i_r(t) - 0.26 \cdot i_1(t) - bg(t)$.

This component separation yields the time-dependent per-pixel intensity functions $d(t)$ (diffusion) and $r(t)$ (reaction). Averaged traces for the absolute amplitudes of $d(t)$ and $r(t)$ are shown in figure 2.19 (subtracted background is the order of 100-150 counts per pixel). Apart from the reaction limit calculated in paragraph 2.4.1, the 4-5 fold contribution of diffusion to the signal is another indication that diffusive material is abundant, and that therefore the speed of exchange in a pit is not limited by diffusive resupply of material.

In practice, the level of recovery α for the reaction and diffusion signal are not identical; the reaction component recovers to a level $\alpha_r = 0.71$ significantly below the diffusion recovery $\alpha_d = 0.82$, which points to a small fraction of the bound material that does not exchange with the diffusible fraction (e.g. clathrin baskets).

2.6 Errors and artifacts

In the following paragraphs, some considerations of the limits and limitations on our measurements are presented. These include the distortion of our measured recovery signals by an electronic intensity artifact mentioned earlier (see fig. 2.14), which has to be corrected for during analysis, and a discussion of different sources of error and their influence on our results.

2.6.1 Time Series Intensity Artifact

Our recording system produces a small electronic artifact, which shows up as an instability of the intensity at the beginning of a time series (which is a series of individually shuttered exposures). Depending on the conditions, this artifact may cause a little “foot” signal at the beginning of a new time series, mimicking recovery (see figure 2.14 or 2.21). In the course of a typical FRAP protocol, new time series are started frequently, since most automatic operations (such as opening or closing a shutter, adding or removing the neutral density filter from the beampath, or loading a new acquisition file) cannot be performed during a running time series. Thus, the artifact may distort the recorded signal at the beginning of the recovery time series after photobleaching.

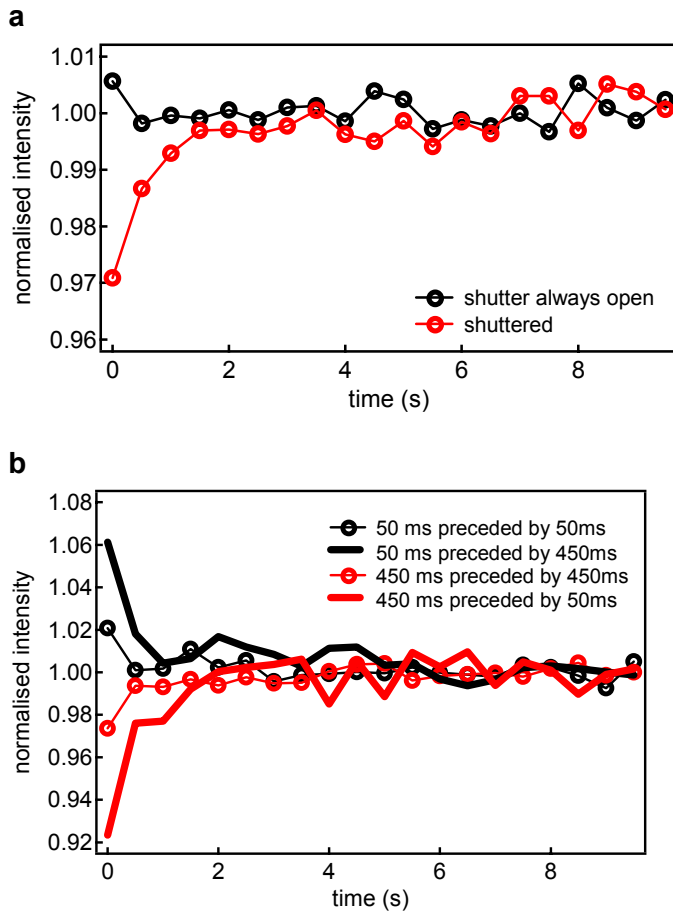
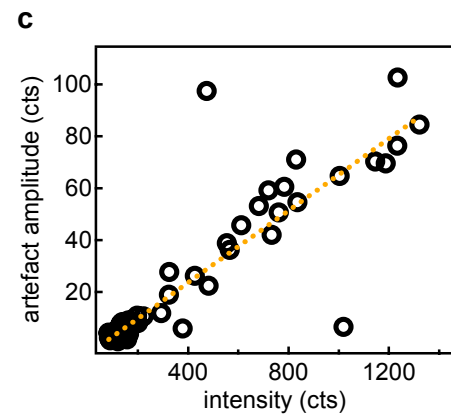


Fig. 2.20: a: Normalised intensity of the second of two subsequent identical time series. Black trace is for zero delay, red trace is for delay caused by the digital shutter opening signal. b: Normalised intensity of the second of two subsequent time series with variable exposure times. c: Magnitude of the artifact (measured in absolute counts) as a function of the absolute intensity.



When several time series are put into sequence, the artifact always occurs at the beginning of the first series, but its magnitude at the start of the subsequent series critically depends on the delay between the series, and may drop to zero for immediately subsequent series. However, even though no delays are programmed into the FRAP protocol before the bleaching recovery, a minimal delay does take place, as several necessary electronic operations are performed (closing the shutter, dropping the neutral density filter, and loading a new acquisition file). Figure 2.20a demonstrates that even the mere shutter operation causes a small delay which may result in a significant artifact. Additionally, the artifact magnitude between subsequent series of identical frequency and different exposure times also depends on the duty cycle of the camera (i.e. the ratio of exposure time and acquisition period), and the ratio of exposure times of the new and the preceding time series (fig. 2.20b). Thus, in a typical recovery recording (exposure time 350-450ms) preceded by bleaching (exposure time 10-50ms), we have to expect a significant artifact of variable magnitude.

Thus, artifact magnitude is quantified individually in each experiment by performing a “mock” FRAP recording before the actual measurement, in which the laser shutter is closed to prevent bleaching. In an experiment with beads of multiple sizes, it was shown that for a given recording, the absolute artifact amplitude is proportional to the absolute intensity (as seen in fig.2.20c). Therefore, the normalized artifact amplitude calculated from the mock recording is used for the correction of the recovery signal.

2.6.2 Focus Drift and error

Another source of signal distortion in our experiments is focus drift. Over the relatively long time range of a FRAP experiments (>2min), the focus of the microscope may drift for a distance of up to some micrometers. Apart from mechanical drift of the microscope, another source of drift is the variable thickness of the immersion oil layer, which is particularly sensitive to temperature variations affecting the viscosity of the immersion oil.

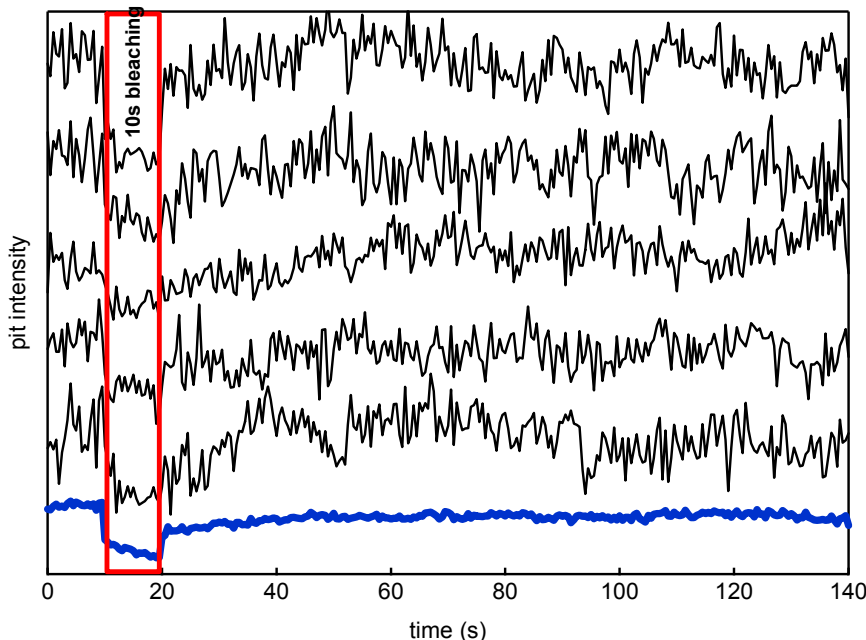


Fig. 2.21: Example traces of single clathrin pit recovery (black) and cell average trace (blue), which is averaged over n=32 individual pits.

As a basic step for focus drift correction, the image is focused several times during the recording, particularly after the recovery. The difference between the final recovery plateau and the refocused intensity is interpreted as focus drift. Recordings with massive drift

(>20%) are rejected from analysis, smaller drift magnitudes are corrected by assuming a constant intensity drift speed.

However, in reality, intensity drift is not necessarily linear. Thus, for a precise analysis of the time course of recovery, a large number of cells were averaged to minimize the influence of drift.

This also raises the question how much the different sources of error contribute to the final determination of the exponential time constant in bleaching recovery. In each cell, the reaction component of pit recovery is calculated as described above; in chromaffin cells, 10-40 pits per cell are analysed, in HEK cells, which often have larger contact regions, 20-60 pits are used. As can be seen in figure 2.21, the individual signals of pit (reaction) recovery are extremely noisy. While the average of all selected pits (blue trace) is much less noisy, it is still, as a whole, affected by focus drift.

Next, the average traces of different cells are averaged to yield the final trace for analysis. This assures that each cell, regardless of the number of pits selected for analysis, contributes equally to the final average. Thus, statistical information (e.g. $n=25$) in the results chapter of this work always refers to the number of recordings or cells (no more than two recordings were ever performed on a single cell), unless stated otherwise.

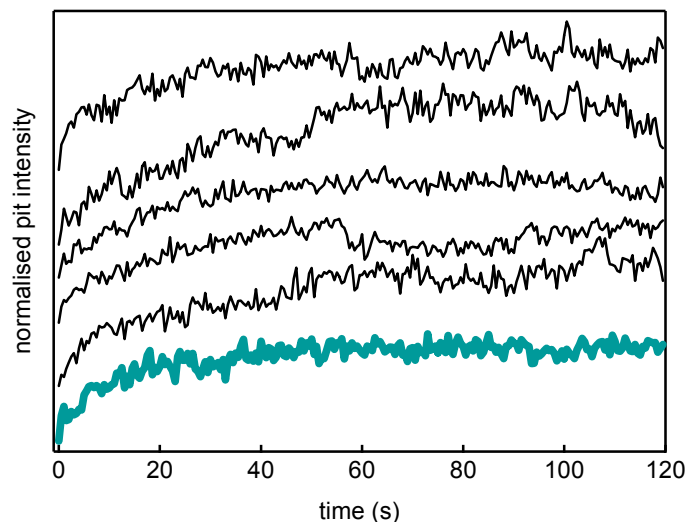


Fig. 2.22: Example traces of single cells (which constitute averages of 20-60pits).

Figure 2.22 shows examples of the average recovery traces of individual cells (black), and the recovery averaged over the five individual traces. The error of this multiple-cell average trace is composed of statistical intensity noise (from all contributing individual pits) and of cell-to-cell variations in focus drift.

To determine the time constant of recovery, the final average trace is fitted with an exponential. The error in the value of τ in the results chapter, unless explicitly stated otherwise, constitutes the estimated error, or standard deviation, of the fit. This error is calculated from the residuals, and it implicitly assumes that the errors are normally distributed with zero mean and constant variance (and, therefore, that there are no systematic errors, which requires that the fit function be a good description of the data).

In a practical sense, the fitting value of τ and its standard deviation are estimates of the mean and standard deviation of the distribution of values that would result if the same original data (with varying noise each time) were fitted an infinite number of times.

Additionally, we want to estimate the contribution of focus drift to the final result of the recovery time. For this purpose we used an alternative method of error determination described in the next paragraph.

2.6.3 Jackknifed error

Apart from the fact that we do not know the exact statistical nature of the error due to focus drift, even Gaussian-distributed statistical noise in the intensity signal does not necessarily lead to a Gaussian error distribution in the value for τ determined from these signals.

Additionally, the approach to determine an error $\Delta\tau$ by fitting all individual cell averages with an exponential (and calculate $\Delta\tau$ as the standard deviation of the resulting distribution) is complicated by the fact that the fit does not converge well for all individual traces.

Therefore, we use the “jackknife” method for error determination ((Thomson, 1991)), which offers a solution to both of these problems. It is particularly suited for distributions where the Gaussian nature of the error is not well established, and it provides individual averages which can be fitted well with an exponential.

We assume $\{x_i\}$ $i = 1, \dots, N$ to be a set of observations (in our case representing average traces from individual cells). θ is the parameter of interest (in our case time constant τ), $\hat{\theta}$ is estimate of θ . $\hat{\theta}_{all}$ is the estimate using all observations, $\hat{\theta}_i$ is the estimate using all observations except i .

The jackknife estimate of θ is:

$$\tilde{\theta} = N\hat{\theta}_{all} - \frac{N-1}{N} \sum_{i=1}^N \hat{\theta}_i$$

Of particular interest to us is the variance, which is

$$\text{var}\{\hat{\theta}_{all}\} = \frac{N-1}{N} \sum_{i=1}^N [\hat{\theta}_i - \theta_{\cdot}]^2 \quad \text{where } \theta_{\cdot} = \frac{1}{N} \sum_{i=1}^N \hat{\theta}_i$$

This value also accurately predicts the variance of $\hat{\theta}_{all}$. An important characteristic is that the jackknife estimate of variance is very conservative, which means that it is always larger than the true variance.

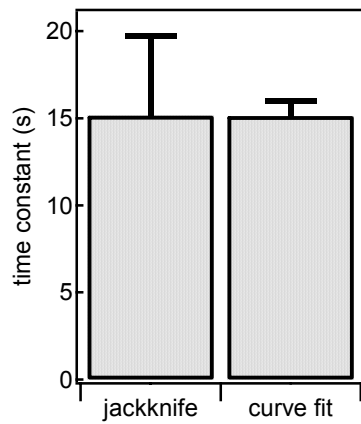


Fig. 2.23: Mean and standard deviation for time constant of clathrin heavy chain recovery, determined with jackknife method and as curve fit mean and estimated error.

Figure 2.23 shows the results of the normal and the jackknifed mean and error deviation for the time constant of bleaching recovery for the clathrin heavy chain fusion construct at room temperature ($n > 70$ cells). The resulting mean value varies less than 1% between the different methods, but the jackknifed error is about fourfold larger than the curve fit estimated error.

This result stresses that in small samples, the error in estimation of k_{off} due to focus drift may be considerably larger than estimated error from the curve fit suggests. Therefore, for reliable quantitative estimates of the time constant, large sample sizes are of pivotal importance.

Chapter 3

Experimental Material

3.1 Experimental Setup

3.1.1 Microscope and image acquisition

All experiments were performed on a Zeiss inverted microscope (Zeiss Axiovert S100 TV, Oberkochen, Germany) with the Zeiss alpha Plan-FLUAR 100x 1.45 NA oil-immersion objective (Zeiss, Oberkochen, Germany).

The microscope filter set consisted of a beamsplitter Q 495 LP, and an emission filter HQ 500 LP (AHF Analysetechnik, Tübingen, Germany).

Images were taken using an intensified air-cooled 5MHz 12bit CCD camera (PentaMAX from Princeton Instruments, Monmouth Junction, USA, available in Germany via Visitron Systems, Puchheim, Germany), with a high quantum efficiency Gen IV intensifier. The camera has 512x512 pixel chip with a pixelsize of 15 μ m. This is internally

modified by 1.5x fiber coupling, to yield a virtual pixelsize of 22.5 μ m. With 100x magnification of the objective described above, the pixelsize in the object plane was 225nm.

For double staining experiments, images were spectrally split using a double imaging fluorescence detector (DIFD) (design by Dr. R. Pick, provided to us with kind permission by the department of Dr. Stefan Hell), where both images were projected onto the left and right halves of the CCD chip (see figure 3.1). Beamsplitter filters were D640/50, HQ 545/60 and DC 560.

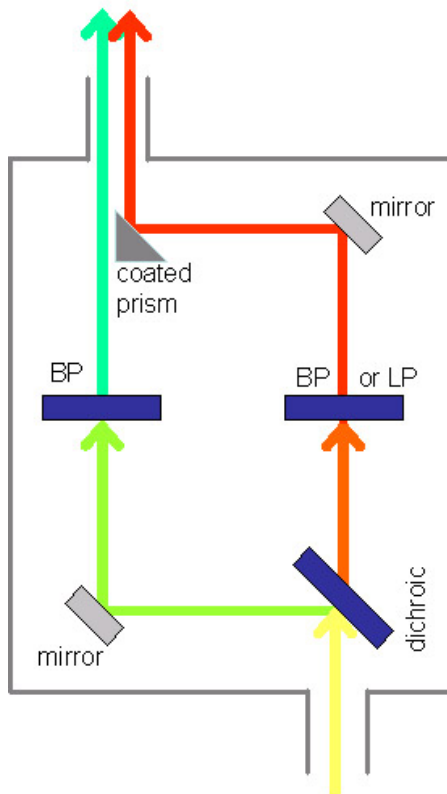


Figure 3.1: Schematic of dual imaging fluorescence detector (DIFD)
Light entering the beamsplitter from the microscope is spectrally split into two images (here: a red and a green image) which are projected onto the camera chip side by side. First, the beam is split using a dichroic beam splitter (DC 560); the red and the green beam are additionally filtered by use of band pass or long pass filters in order to clearly separate contributions from GFP (green fluorescent protein) and mRFP (red fluorescent protein).

Imaging data were digitized and analysed using Metamorph software (Universal Imaging Corporation, Downingtown, USA). Regions of interest (ROIs) in images were selected by hand, and the data was transferred for further analysis to Igor Pro (Wavemetrics, Oregon, USA), where self-written macros were used to perform the data analysis described in chapter 2.

3.1.2 Laser and optical system

Fluorescence was excited in epifluorescence mode using a polychromatic device (Polychrome IV, TILL Photonics, Germany). For TIRF mode, a laser beam from an air-

cooled argon ion laser (Model 185-F12, 75mW TEM₀₀ at 488nm, Spectra Physics, Stahnsdorf, Germany) was coupled into the microscope with a KINEflex fibre and coupling system (Point Source, Southampton, UK).

Both the laser fibre and the fibre from the monochromator were coupled into the microscope via the TILL TIRF condenser (TILL Photonics, Gräfelfing, Germany) (described in more detail further below, see figure 3.3).

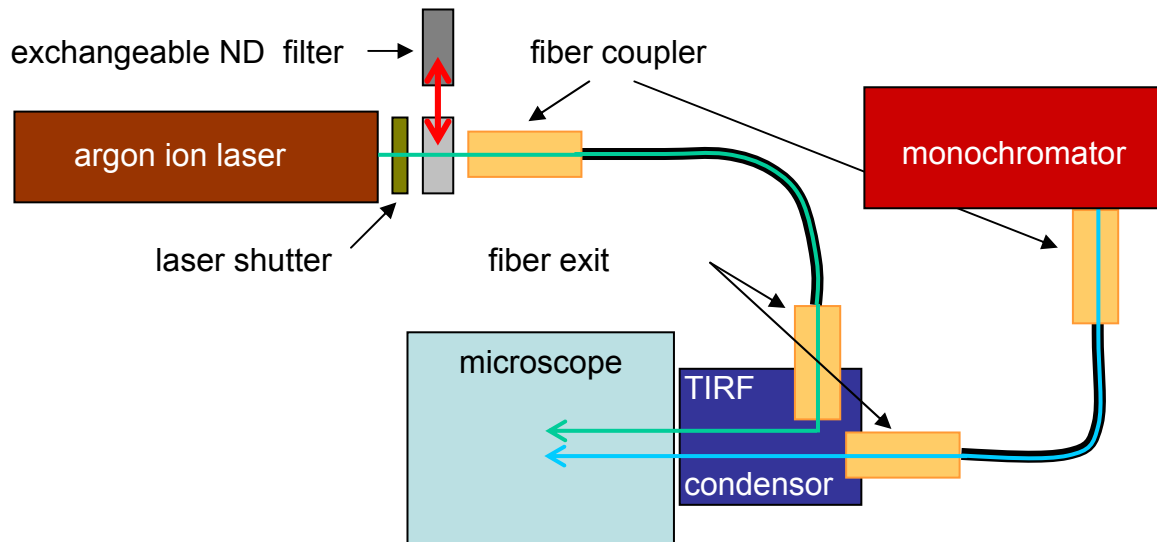


Figure 3.2: Schematic of laser and optical system.

Pre-fibre, the laser beam was shuttered (shutter from TILL photonics, Gräfelfing, Germany); laser excitation intensity was switched during FRAP experiments using a servo device dropping a neutral density filter (ND=1.6, Schott, Jena, Germany) into the light path for regular data acquisition, and removing it for bleaching. (Since the servo device is relatively slow, the command pulse for filter dropping/removing in an experiment was given before additional operations such as shuttering or acquisition file loading were performed). Laser shutter, ND exchanger, and monochromator operation were controlled by the imaging software, and could thus be automatically integrated into experimental sequences of image recordings.

The schematic in figure 3.3 shows the layout of the optical beam path in the inverted TIRF microscope and the TIRF condenser in more detail. The laser beam coupled into the optical fiber is then connected to the TIRF condenser. The laser beam is reflected at a 45° prism (hypotenuse is reflectively coated) to enter the microscope parallel to the optical axis. The fiber exit and prism can be moved together with a micrometer screw in the plane

indicated by the blue arrow; this lateral parallel shifting allows to modify the distance of the laser beam from the optical axis.

The laser beam is focused (using a tube with two lenses) to the back focal plane of the objective, approximately corresponding to its back aperture plane, so that the beam is parallel in the interface (object) plane, where it is reflected. The beam's distance from the optical axis in the back focal plane is determined by the prism position, and as the beam leaves the front of the objective, this separation distance determines the angle of beam incidence onto the dielectric interface (between coverslip and aqueous medium). For optical coupling, the coverslip is placed onto the objective on immersion oil of matching refractive index.

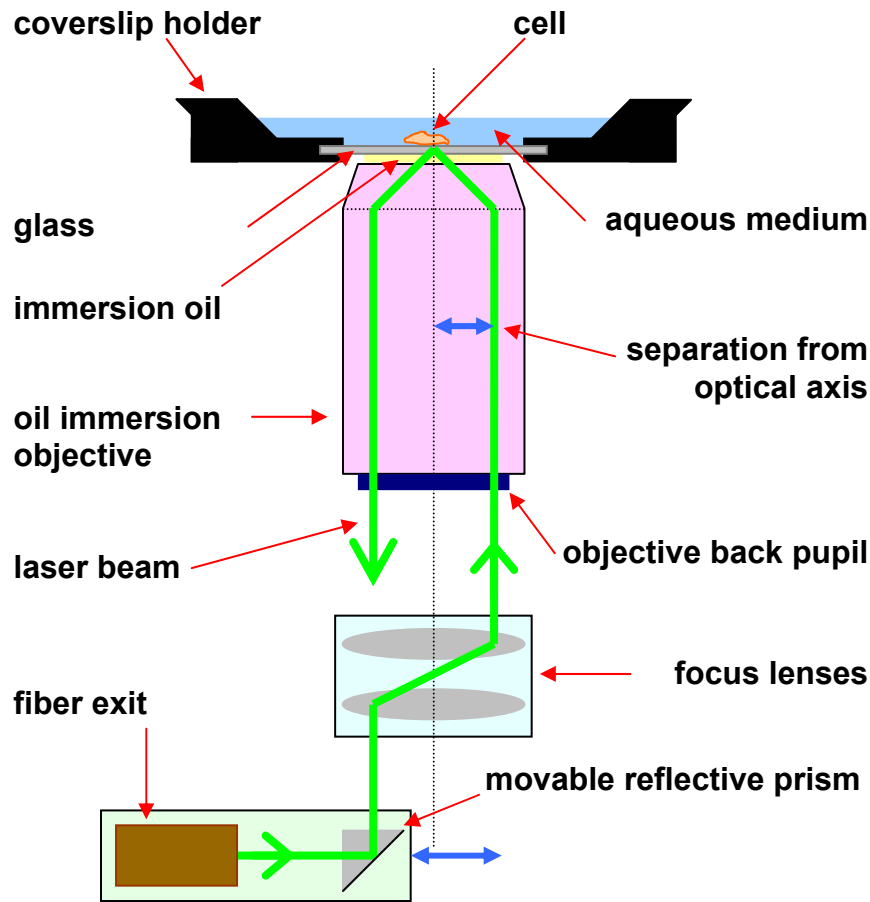


Figure 3.3: Schematic of inverted microscope TIRF experimental setup.

It should be noted that the maximum separation distance of the beam from the optical axis is limited by the back pupil diameter of the objective, so that the maximum possible angle for marginal rays corresponds to the angle of the objective cone. The cone-angle of the objective is defined by its numerical aperture, $NA = n \cdot \sin \alpha$ (where n is the refractive index of the immersion medium); thus, in order to create an evanescent field, it is necessary to use

objectives with numerical apertures exceeding the value corresponding to the critical angle $NA = n \cdot \sin \theta_c = 1.51 \cdot \sin(61.04^\circ) = 1.32$. (For this study, a $NA=1.45$ objective was used.)

Not shown in the schematic above is the piezoelectric focusing device (PIFOC, Physik Instrumente, Waldbronn, Germany) placed between the objective revolver of the microscope and the objective, which was used to control the image focus and to refocus during experiments.

3.2 Material

3.2.1 Cells

HEK 293 cells (human embryonic kidney cell line) (see e.g. Graham et al., 1977)

Cells are grown in standard plastic culture flasks. The cells are passaged by removal from flask through trypsinisation, subsequent centrifugation, and resuspension.

The culture medium is standard modified Eagle medium with 10% FCS (Fetal calf serum), and penicilin/streptomycin.

Chromaffin cells

(see, e.g. Marty and Neher, 1985, and Nagy et al., 2002 for the most recent protocol)

Bovine adrenal glands are enzymatically digested with collagenase and manually dissected. Pieces of the medulla are collected and centrifuged. After removal of the supernatant, the tissue is minced through a nylon mesh and washed; the cell suspension is centrifuged and resuspended several times.

For both cell types, the cell suspension is plated in 12-well cell Falcon culture plates on glass coverslips (thickness 0.14mm) coated with 0.1mg/ml Poly-L-Lysine (Sigma-Aldrich, Seelze, Germany).

3.2.2 Measuring Solutions

Basal buffer for chromaffin cells and HEK cells contains:

150 mM NaCl
5 mM KCl
1 mM MgCl₂
2 mM CaCl₂
10 mM Hepes
2 mg/ml Glucose
310 mosm for chromaffin cells
330 mosm for HEK cells
pH 7.4

Potassium glutamate solution used for membrane sheets and permeabilised cells contains:

120 mM potassium glutamate
20 mM potassium acetate
20 mM Hepes
4 mM MgCl₂
2 mM ATP
2-10 mM EGTA or Ca²⁺-EGTA buffer
pH 7.2-7.4

For experiments with nominally zero free calcium concentration, 5mM EGTA (and no Ca²⁺-EGTA) was added to the solution. For experiments with zero ATP and normal calcium, ATP was left out, and 7.7mM EGTA and 3.3mM Ca²⁺-EGTA were added to yield a calcium concentration of 100nM (for calculation of calcium concentration, see Appendix)

3.2.3 Fluorescent probes

Clathrin light chain GFP fusion construct:

The construct was generated by Claudia Arlt (for a detailed description, see Mueller et al., accepted).

Clathrin heavy chain GFP fusion construct:

The clathrin heavy chain GFP construct was generated by Martin Wienisch. Human clathrin heavy chain (CHC) cDNA was obtained from Kazusa DNA Research Institute (Kisarazu, Japan; clone name ha00931). To generate an EGFP fusion protein, a carboxy-terminal fragment of CHC corresponding to nucleotides 3936-5024 (open reading frame)

was amplified by PCR with a 5' forward primer covering the endogenous CHC *Sac* I site (5'-TTG AGC GAG CTC ACA TGG GAA TGT TTA CTG-3') and a 3' reverse primer encoding a *Sac* II site (5'-CGT TAT CCG CGG CAT GCT GTA CCC AAA GCC AGG CTG-3'). This fragment was ligated into pEGFP-N1 (BD Bioscience Clontech, Heidelberg, Germany) using *Sac* I and *Sac* II restriction sites.

The remaining clathrin heavy chain fragment was cut out from the original clone using the restriction endonucleases *Sma* I and *Sac* I and was ligated into the fragmentary EGFP construct restricted with *Eco*47 III and *Sac* I. The complete CHC-EGFP construct was verified by dideoxynucleotide sequencing.

Clathrin light chain mRFP fusion construct:

The construct was generated by Edward Lemke.

mRFP-C1: Monomeric Red Fluorescent Protein (mRFP, see Campbell et al., 2002) DNA was amplified by PCR from mRFP-pBluescript II KS (Stratagene, Gebouw, CA) (gift from Prof. Dr. Söling, department of Neurobiology). After restriction with endonucleases *Age*I-*Bgl*II, the PCR product was ligated into a pEGFP-C1 expression plasmid (Clontech, Palo Alto, CA) restricted with the same nucleases, thus replacing the EGFP with the mRFP.

mRFP-C1 for: 5'-GCG CAC CGG TCG CCA CCA TGG CCT CCT CCG AGG AC

mRFP-C1 rev: 5'- TCG AGA TCT GGC GCC GGT GGA GTG GCG GCG GCC

The **LCa1-mRFP-C1** overexpression plasmid was obtained by PCR amplification of the LCa1-pEGFP-C3 ((Mueller et al., accepted)) construct with the following primers:

LCa1/polyA/C1/for: 5'-AGA TCT CGA GCT GCT GCT GCT GCT ATG GCT GAG TTG GAT CCA TT

LCa1/polyA/C1/rev: 5'-CCT CTA CAA ATG TGG TAT GGC TG)

After restriction with endonucleases *Xho* I and *Kpn* I this PCR product was ligated this time into the mRFP-C1 expression plasmid (see above) restricted with the same endonucleases.

Cell transfection:

For chromaffin cells, transfection with the viral construct was used; cells were measured 5-10 hours after addition of the virus.

In HEK cells, Lipofectamine transfection (Lipofectamine Reagent, Invitrogen, Karlsruhe, Germany) was performed according to the manufacturer's instructions. Cells were usually measured after 5-8 hours. (For an example of HEK cells transfected with clathrin heavy chain-EGFP with lipofectamine, see figure 3.3).

3.2.4 Treatments and drugs

Fixation: Cells were fixed in 4% paraformaldehyde (in phosphate buffered solution) for 3hrs at room temperature.

Membrane sheet preparation (see Holroyd et al., 2002): Cells were ruptured by sonication in potassium glutamate solution.

Permeabilisation (see Chung et al., 1995): Cells in potassium glutamate solution were treated for 1 min at room temperature with 10 μ M digitonin, then washed.

Cellular ATP depletion: Cells were incubated for at least 30 min at 37°C with 16 μ M rotenone.

Calcium depletion: Cells were incubated at room temperature with 200 μ M EGTA-AM.

Hypertonic sucrose treatment: Cells were incubated for at least 30 min at 37°C in solution containing 0.2M sucrose.

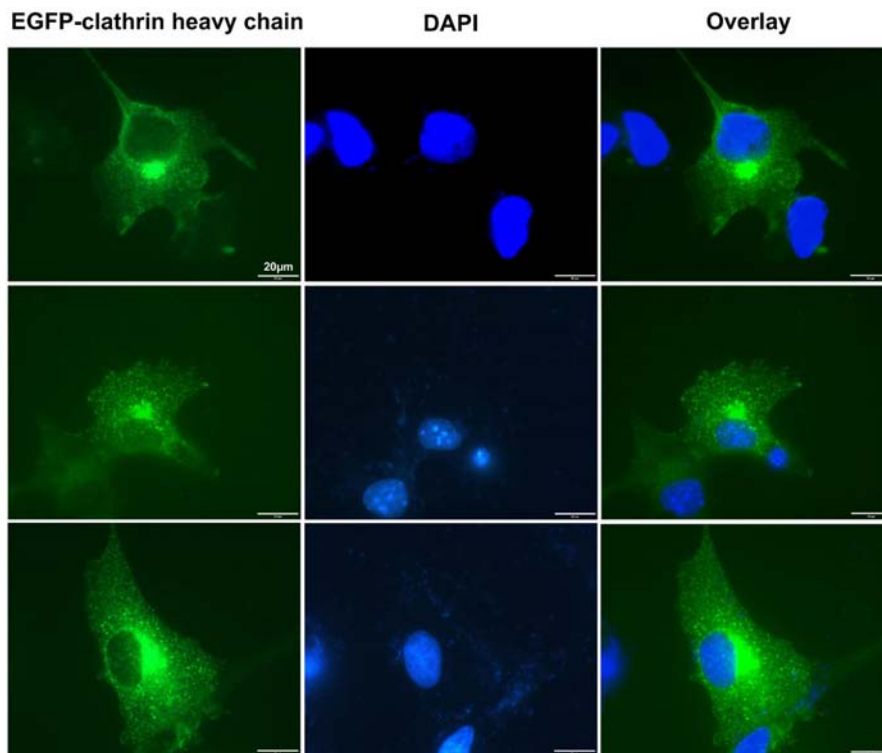


Fig. 3.3: Left column of panels (green): clathrin heavy chain GFP; middle column of panels (blue): DAPI nuclear stain; right column of panels: overlay. The overlay shows that CHC is distributed in a perinuclear fashion, putatively in the Golgi apparatus. There is a punctuate distribution ascribed to putative single coated pits (This image was kindly provided by Nadja Jung, Department of Biochemistry II, Medical Faculty, University of Göttingen).

Chapter 4

Results

In this chapter, data on the exchange properties of clathrin light chain and clathrin heavy chain from pits are presented. First, it is demonstrated on clathrin light chain that using the approach detailed in chapter 2 (Theoretical and experimental methods), it is indeed possible to separate two components in our recovery signal: One is the diffusive component (which disappears in fixed cells), the other is the reaction component, which can be selectively blocked by different treatments that leave the diffusion unaffected. It is also shown that the speed of exchange is not limited by the speed of the diffusion, but is modified by changes in temperature.

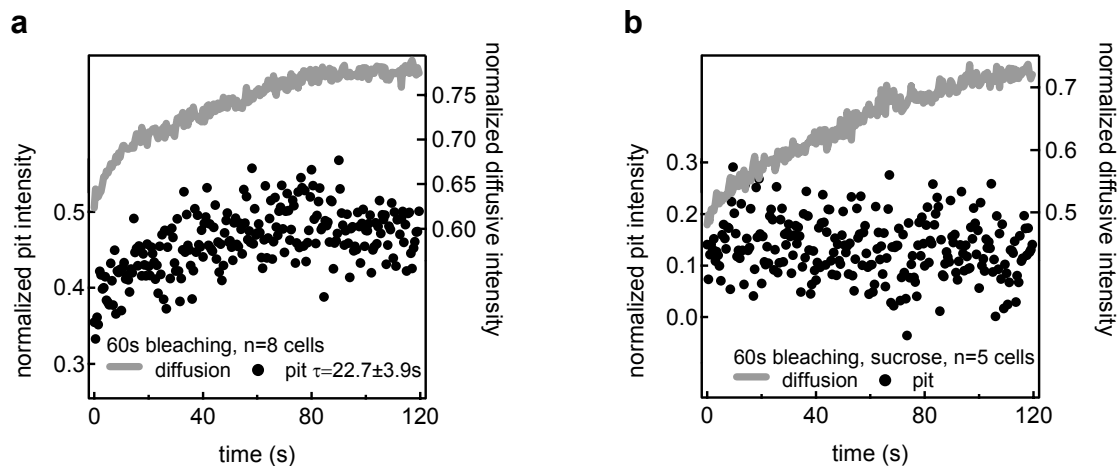
Secondly, the exchange a clathrin light chain studied in the first part is compared to a clathrin heavy chain construct. The results demonstrate the existence of a light-chain independent pathway for clathrin heavy chain from pits.

4.1 Clathrin light chain

Using the clathrin light chain fusion construct in chromaffin cells, it was demonstrated that it is possible to separate the measured pit signal into independent contributions from diffusion and from reaction exchange. For this purpose, FRAP experiments were performed on cells treated with sucrose or rotenone, which are expected to selectively inhibit the exchange of clathrin molecules from pits, but not to affect diffusive recovery. Additionally, FRAP experiments were performed with varying bleaching times, to show that pit recovery does not depend on – and is not limited by - varying time courses of diffusive recovery.

4.1.1 Separation of components: light chain exchange inhibition

It is known from the literature (e.g. Wu et al., 2001) that clathrin light chain exchange can be blocked with a number of drugs, among these hypertonic sucrose and ATP-depletion. In this study, use was made of this effect to selectively inhibit the reaction component of the signal, while the diffusive component, in theory, should not be affected. For this purpose, chromaffin cells were treated with 0.2M sucrose or 15 μ M rotenone for approximately 30min before recording. FRAP experiments were performed with 60s bleaching (at room temperature).



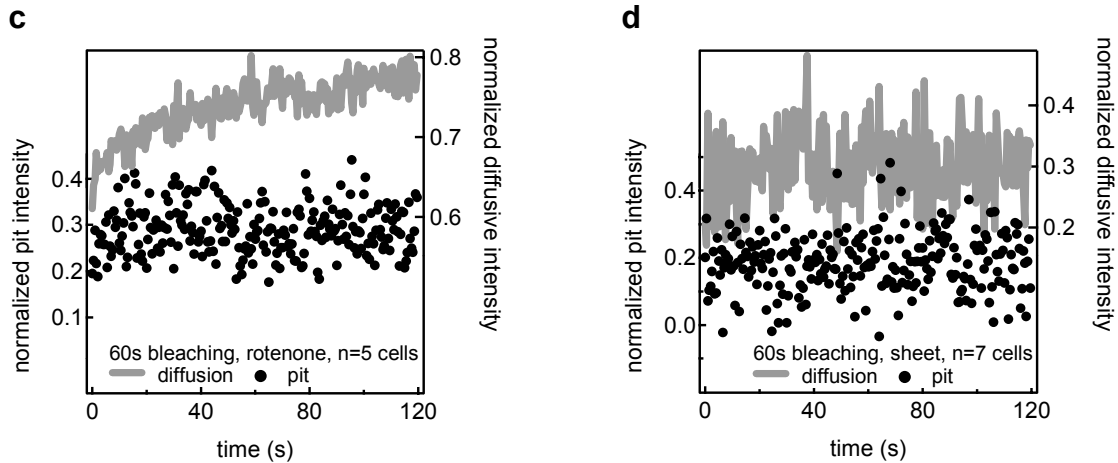


Figure 4.1 Pit recovery (black) versus diffusive recovery (grey) after 60s bleaching in an untreated cell (a), in a cell pretreated with sucrose (b), in a cell pretreated with rotenone (c), and in a membrane sheet (d). The averaged time constant of recovery in the untreated cells is 22.7 ± 3.9 s ($n=8$).

Additionally, the same experiments were performed on membrane sheets; membrane sheets are produced by rupturing the cell bodies through sonication, so that only the membrane patch attached to the surface remains. Since in this case, the diffusive component originating from the cytosol is removed, we expect *both* components of recovery to be abolished.

In figures 4.1 a-d, the reaction and diffusion recovery (calculated as described in chapter 2) are shown for untreated cells, membrane sheets, and for cells pre-treated with sucrose or rotenone. The traces show that pit recovery is suppressed in rotenone- and sucrose-treated cells, while their diffusion component is intact. In membrane sheets, there is no recovery, neither in the diffusive nor the reaction component.

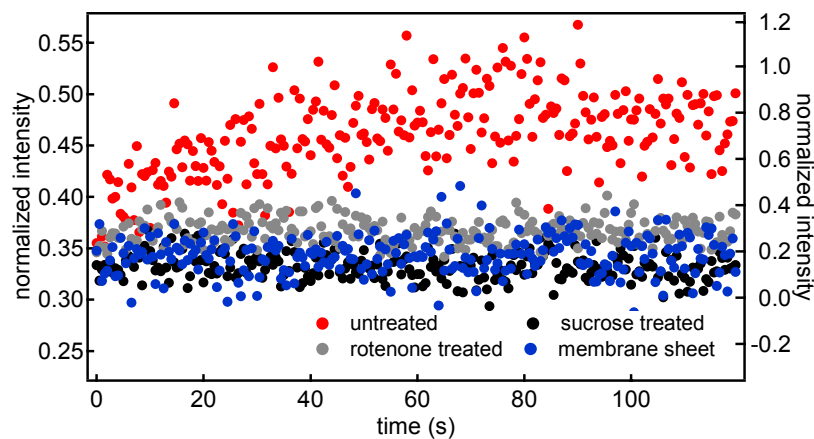


Fig. 4.2: Reaction recovery
Untreated cells recover from photobleaching with a time constant of about 20s. In cells treated with rotenone or sucrose or in membrane sheets, no reaction recovery is observed.

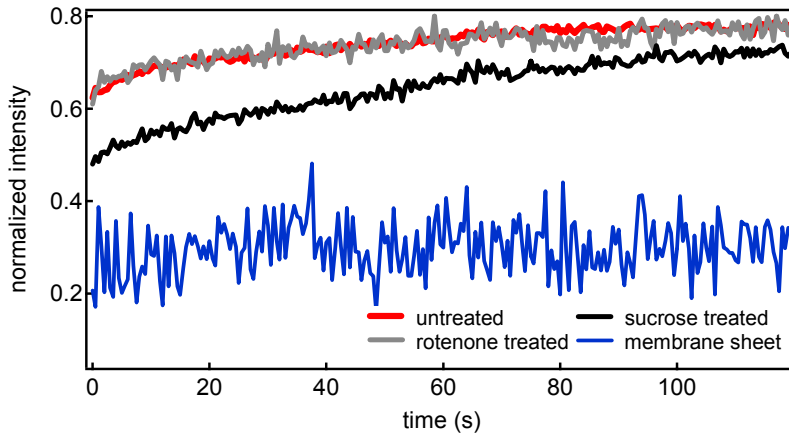


Fig. 4.3: Diffusion recovery
Diffusion recovery in rotenone-treated cells is unchanged. Recovery is also intact in sucrose-treated cells, although the time course is modified. No diffusion recovery is seen in membrane sheets.

The reaction and diffusion recovery traces of figure 4.1 are summarized in figure 4.2 and 4.1. The time constant of reaction recovery in untreated cells is on the order of 20s. The graphs also show that rotenone treatment does not significantly affect the time course of diffusive recovery; while the sucrose treatment does not inhibit diffusive recovery, it may have an influence on its time course.

4.1.2 Separation of components: variable bleaching times

Next, FRAP experiments were performed on cells with varying bleaching times; in addition to the data above taken at 60s bleaching interval, experiments were performed at 20s, 10s, 5s and 3s bleaching interval. For 10s and 3s bleaching, the inhibition of the reaction component was also tested with sucrose treatment as above (see figure 4.4 and figure 4.5).

The graphs show that, as for 60s bleaching, the reaction recovery is suppressed by sucrose treatment, while the time course of the diffusion recovery is not significantly affected by the treatment.

Figure 4.6 summarizes the diffusive recovery traces, figure 4.7 the reaction recovery component for all bleaching times (3, 5, 10, 20 and 60s). The graphs show that while the time course of recovery of the diffusive signal changes significantly with the bleaching duration, the time constant of recovery appears similar for all bleaching times (also see fig 4.8a), even if its amplitude of bleaching and recovery (α and β) is modified by varying bleaching times (also see figure 4.8b, paragraph 2.4.2).

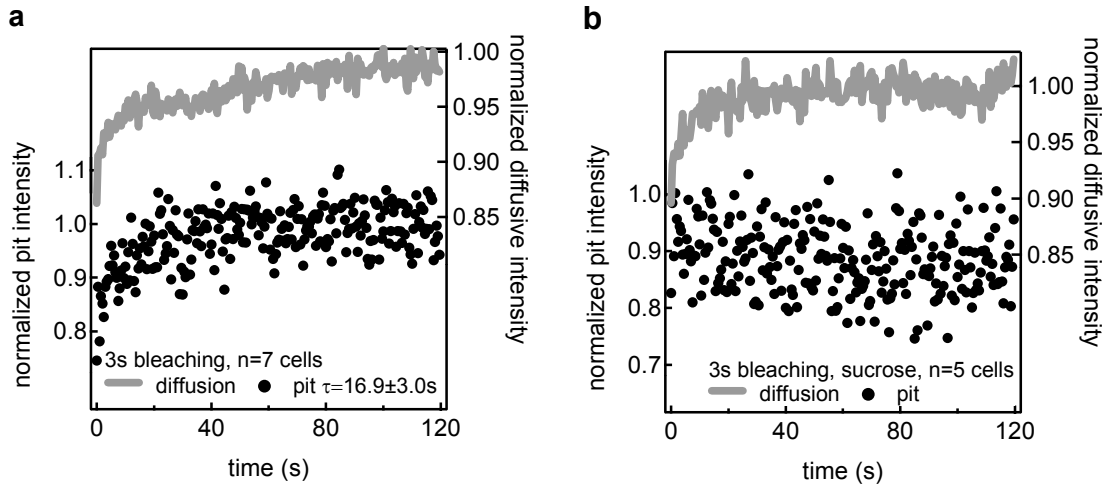


Figure 4.4 Pit recovery (black) versus diffusive recovery (grey) after 3s bleaching in an untreated cell (a) and a cell pretreated with sucrose (b). Pit recovery is blocked by sucrose treatment.

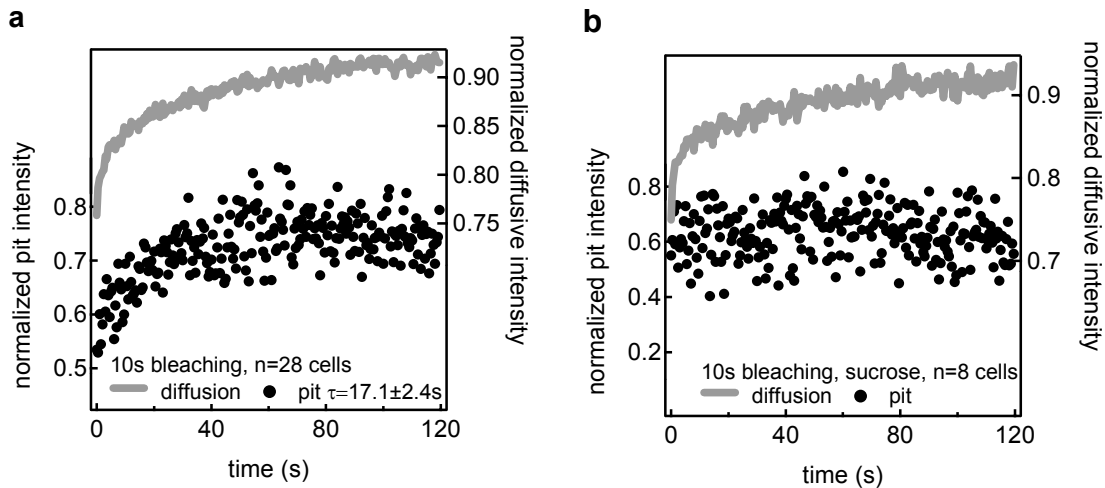


Figure 4.5a+b: Pit recovery (black) versus diffusive recovery (grey) after 10s bleaching in an untreated cell (a) and a cell pretreated with sucrose (b). Pit recovery is blocked by sucrose treatment.

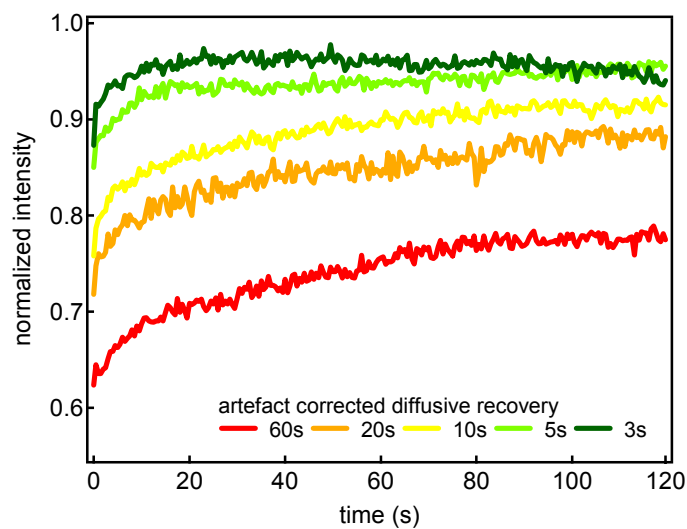


Figure 4.6: Summary of diffusive recovery for varying bleaching intervals: The timecourse of diffusive recovery varies significantly with different bleaching intervals.
t=60s, n=8
t=20s, n=7
t=10s, n=28
t=5s, n=5
t=3s, n=7

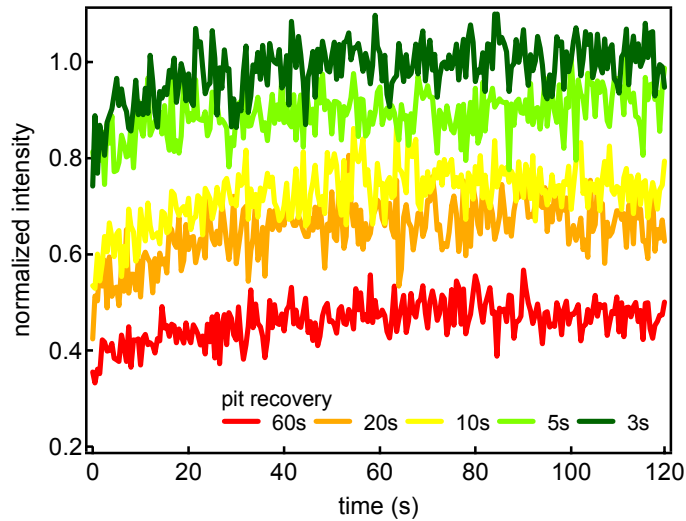


Figure 4.7: Summary of pit recovery for varying bleaching intervals: While the amplitude of bleaching depth (β) and the amplitude of recovery ($\alpha-\beta$) depend on the bleaching interval, the timecourse of pit recovery changes little for different bleaching intervals.

The reaction recovery traces in fig 4.7 are fitted with an exponential function, and the fit results are summarised in figure 4.8a. The traces are approximated well by a mono-exponential recovery with a time course on the order of $\tau=18-19$ s. The deviation from this value for a bleaching interval of 60s is not significant (due to the large error bars caused by the relatively small number of experiments, i.e. $n=8$ cells). However, it may add a note of caution for extremely long bleaching times.

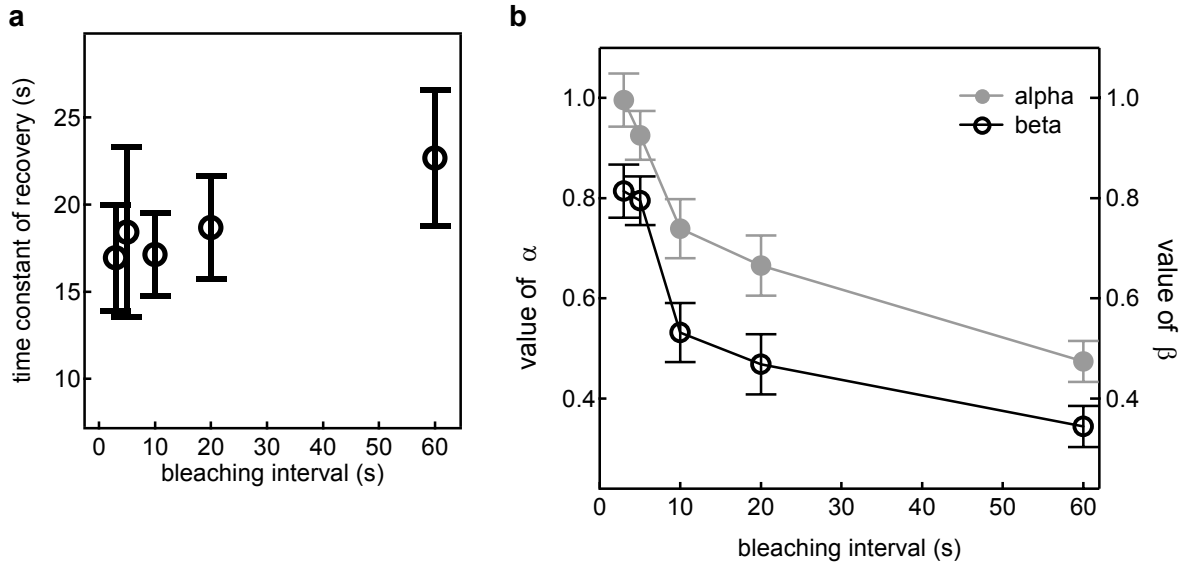


Fig. 4.8: a: Time constant of pit recovery for different bleaching times. b: Values of recovery level (α) and bleaching depth (β) for different bleaching times.

These experiments demonstrate that the two components of recovery, reaction and diffusion, are indeed independent of each other. From the results of bleaching for different time intervals, we conclude that for bleaching up to about 20s, the speed of pit recovery is not limited by diffusion speed. For all further experiments, bleaching times of 10s are used which lie well within the limit.

4.1.3 Bleaching constant

The time course of intensity during bleaching can be used to calculate the bleaching constant k . Thus, β (as a function of bleaching time) could be fitted to yield k as described in paragraph 2.4.3. However, since the 5 data points in figure 4.8b are not enough to provide a good estimate, the calculation was done from an additional intensity recording of formaldehyde-fixed chromaffin cells (where diffusion is abolished by the fixation).

The normalized intensity trace during bleaching (averaged over 4 cells) is shown in figure 4.9. The intensity was fitted with the equation

$$I_n(t) = \frac{(1 - \exp(-k_0 t))}{k_0 t}$$

to yield the parameter $k_0 = 0.11 \pm 0.02 \text{ s}^{-1}$.

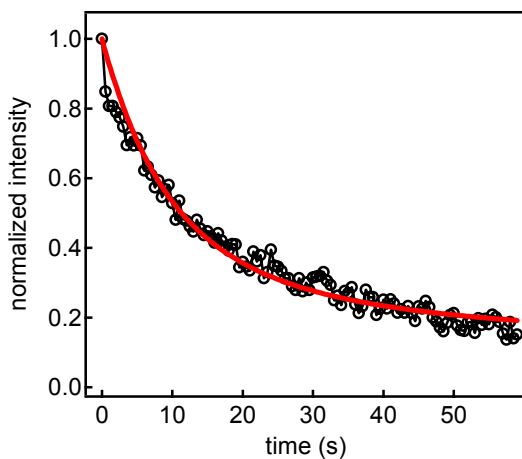


Figure 4.9: Average intensity of fixed cells ($n=4$) during 60s bleaching. Red trace is fit with equation as described above.

4.1.4 Diffusion results

The diffusion recovery traces for different bleaching times were analysed to gain some information about the diffusion process.

For a given value of k_0 and a given duration of the bleaching interval, the time course of the diffusion recovery depends on the diffusion coefficient D , and the shape and depth of the physical reservoir of fluorophores. In the solutions to the diffusion equation, these parameters are D and l , where the latter is the thickness of the plane sheet.

Figure 4.10 shows four calculated example traces for different values of D and l . The graph shows that the traces with identical values for l (solid and dotted lines) recover to the same value; thus, the final plateau level of recovery (α in analogy to the recovery in the immobile fraction) depends only on the depth of the plane sheet (the axial diameter of the cell). The bleaching depth β , i.e. the intensity after bleaching, depends on the diffusion coefficient.

Since the recovery has a complicated time course (particularly, it is not a mono-exponential function), two important characteristics are picked out for analysis, which are

1. the slope of the recovery trace after 120s recovery and
2. the recovery amplitude ($\alpha - \beta$).

The inclination of the recovery function, particularly late into recovery, strongly depends on both diffusion speed and cell diameter; the inclination increases with increasing l and with decreasing D .

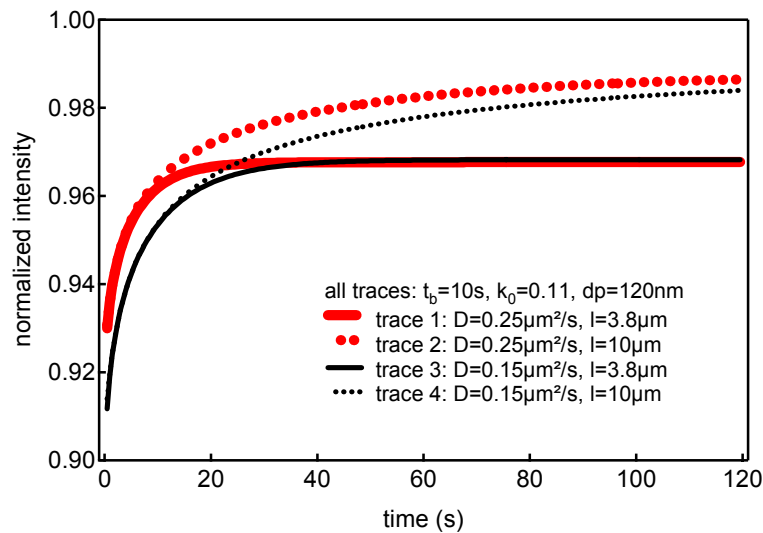


Fig. 4.10: Calculated diffusive recovery for fixed bleaching time t_b , bleaching constant k and penetration depth dp , and variable diffusion coefficient D and plane sheet depth l .

As the speed of diffusion and the cell diameter differentially affect the plateau value α and the bleaching depth β , the recovery amplitude ($\alpha - \beta$) measured at a given time point is determined by a combination of the two. Small amplitudes are achieved by fast diffusion and small diameters (solid red trace), whereas high amplitudes are achieved with slow diffusion and large diameters (dotted black trace).

The measured diffusion traces from the cells for 10s bleaching is shown in figure 4.11. The diffusion traces cannot be fitted or approximated well with a single solution for the plane sheet diffusion equation. For all bleaching times (3, 5, 10, 20 and 60s), the inclination

of the recovery trace at 120s is significantly larger than zero, which points to large diameters and slow diffusion. For values of D and l that fulfill this requirement, however, the predicted recovery amplitude of the traces is up to two-fold higher than the measured value; the measured recovery amplitude rather points to small diameters and fast diffusion. Therefore, it must be concluded that the actual cell conditions are certainly more complicated than a simple plane-sheet geometry, and that there are contributions from different populations of fluorophores, which physically differ in their distance from the interface and their speed of exchange with bleached fluorophores.

The bulk of the material has a high diffusion coefficient on the order of $D=0.25\mu\text{m}^2/\text{s}$ and a depth on the order of $l=4\text{-}6\mu\text{m}$. This limits the amplitude of recovery, as the material in this pool quickly reaches equilibrium. Additionally, there is a contribution from fluorophores much farther away from the interface (on the order of $>10\mu\text{m}$), which also have a much lower average diffusion coefficient (which is probably a reflection of diffusion barriers, most notably the nucleus, or the actin network). These fluorophores are the cause of the persisting diffusion late after the end of the bleaching pulse.

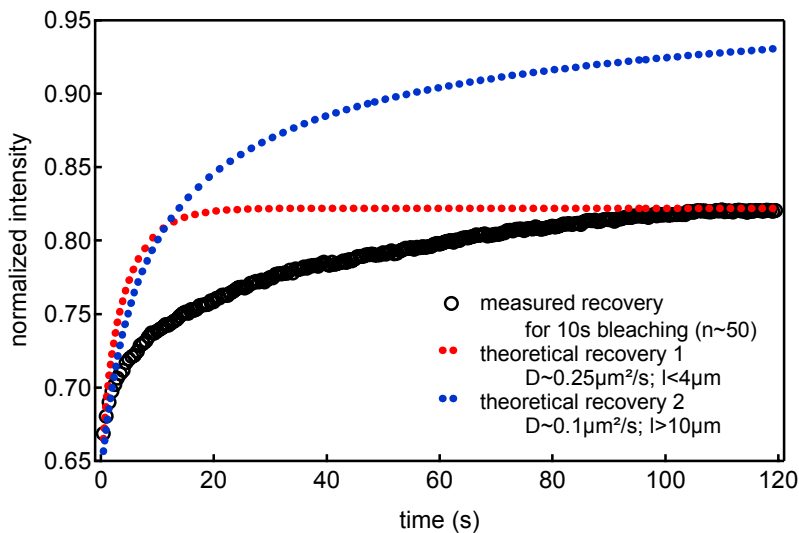


Fig. 4.11: Diffusive recovery

As an example, the graph shows the measured diffusion recovery trace for 10s bleaching and the calculated theoretical traces which account for recovery amplitude (red trace) and for inclination at 120s (blue trace). (n=28)

In addition to the rough estimations for D and l from the time courses of recovery in figure 4.11, the level of diffusion recovery in all experiments with variable bleaching times was plotted (see figure 4.12a). Using the value $k_0=0.11\pm 0.02\text{s}^{-1}$ estimated in the previous paragraph, theoretical predictions for the function $\alpha(t_{\text{bleach}})$ were calculated for different values of the cell's (or plane sheet's) thickness (red, green and blue trace in figure 4.12a). The best match is for $l=3.8\mu\text{m}$, which thus constitutes something like an average effective thickness for the fast component of diffusion recovery.

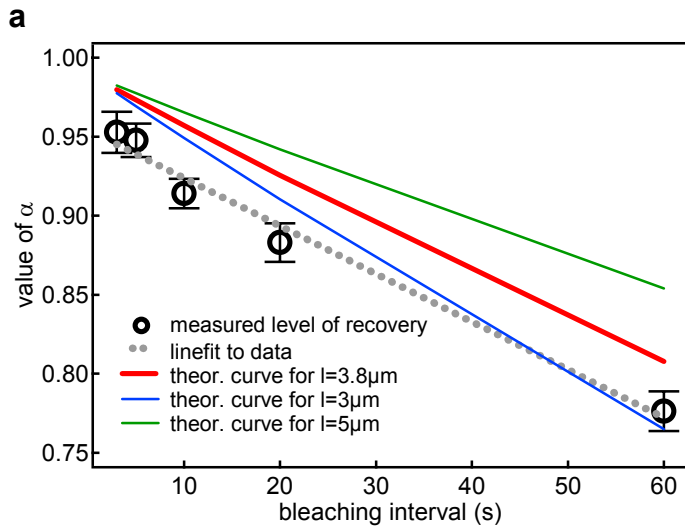
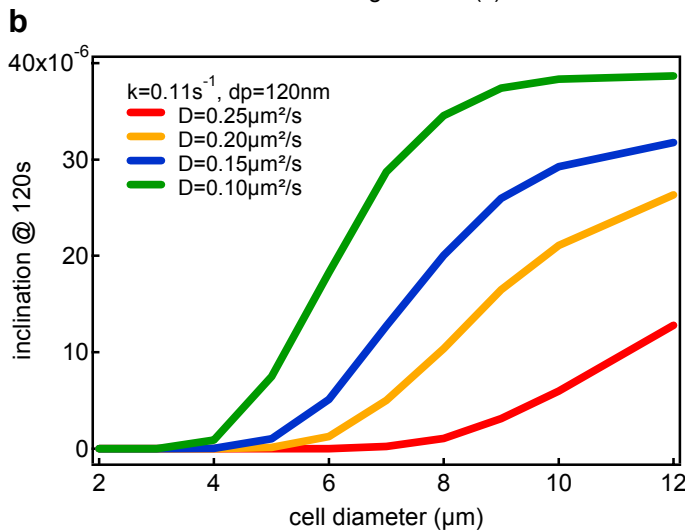


Fig. 4.12:
a: Recovery level α as a function of bleaching interval (n as in figure 4.6).



b: Slope of theoretical recovery curves (at $t=120s$) as a function of cell thickness, for different values of the diffusion coefficient D .

For the slow component determining the high inclination of the trace at 120s after bleaching, an estimation was also made from theoretical curves. Figure 4.12b shows theoretical predictions of the inclination at 120s as a function of plane sheet (cell) thickness (for 10s bleaching), for different values of the diffusion coefficient D . The slope of the measured trace (figure 4.11) was estimated to be approximately $25 \times 10^{-6} s^{-1}$. From graph 4.12b, it can be estimated that this value requires both a slightly lower diffusion coefficient (not exceeding $D=0.2 \mu m^2/s$) and a thickness on the order of 8-10 μm .

4.1.5 Temperature-dependent recovery

After it was demonstrated that it is possible to measure the exchange reaction of clathrin in pits, the time constant of reaction recovery was determined for different

temperatures. The measurements were performed with the clathrin light chain in chromaffin cells.

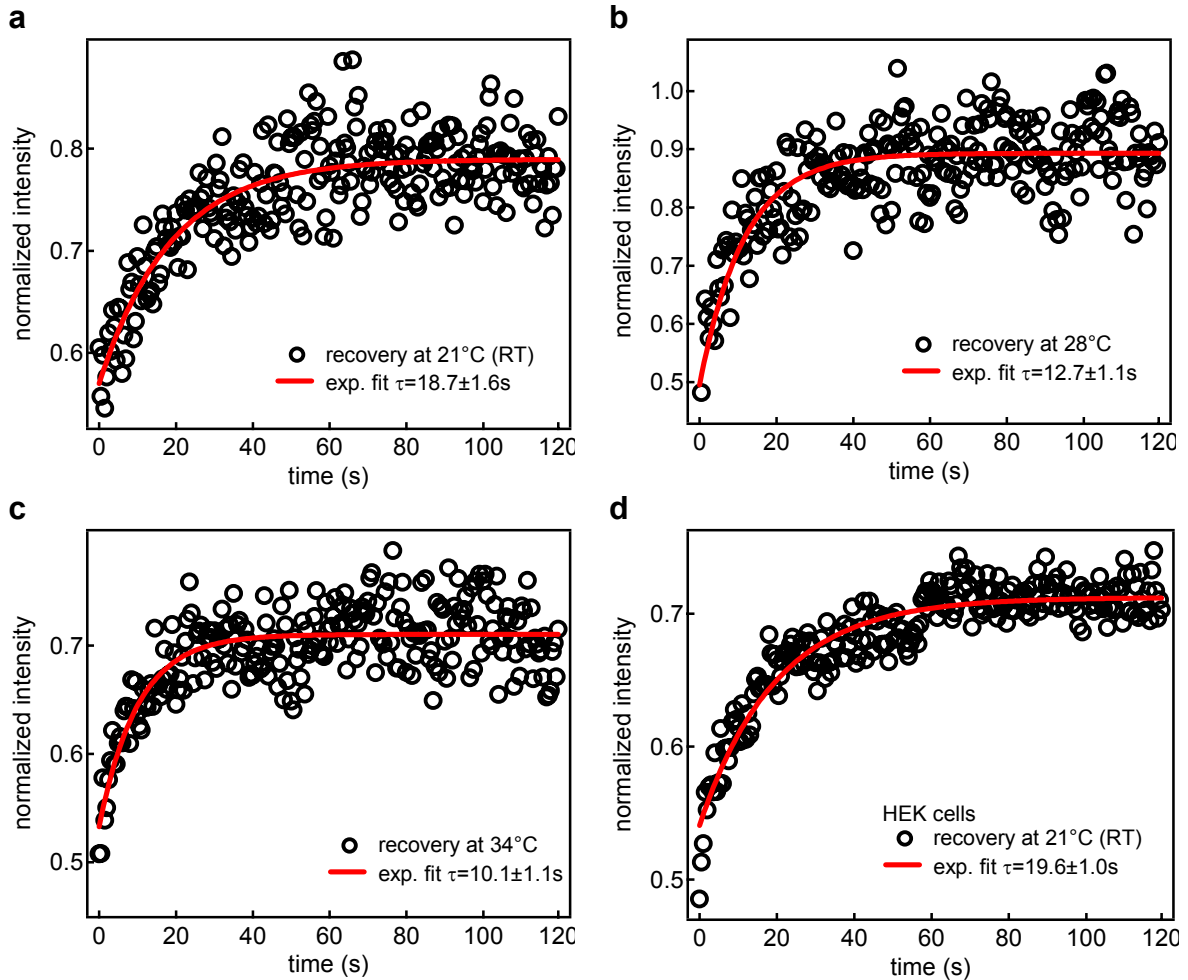


Fig. 4.13: Reaction recovery for different temperatures a: Chromaffin cells, room temperature (n=37) $\tau = 18.7 \pm 1.6$ s. b: Chromaffin cells, 28°C (n=20) $\tau = 12.7 \pm 1.1$ s. c: Chromaffin cells, 34°C (n=15) $\tau = 10.1 \pm 1.1$ s. d: HEK cells, room temperature (n=33) $\tau = 19.6 \pm 1.0$ s.

All experiments record the recovery from 10s bleaching. Later in this chapter, the results for clathrin light chain will be compared to clathrin heavy chain results; lacking a heavy chain virus construct (which would be necessary to transfect chromaffin cells), heavy chain measurements were performed in HEK cells (using lipofectamine transfection). Therefore, in addition to the measurements in chromaffin cells, the temperature-dependent recovery time constant of light chain was also measured in HEK cells to insure that the heavy chain/light chain differences are not caused by different cell systems.

Temperatures of up to 28°C could be reached with block heating; for higher temperatures, the additional use of an objective heater was necessary. No objective heater

was available for the standard Zeiss TIRF objective used in all other experiments, so that the experiments at temperatures exceeding 28°C were performed with a Nikon objective with a fitting objective heater. The maximum temperatures reached at the specimen were in the range 31-34°C. Figure 4.14 shows the summary of the time constants determined for chromaffin and HEK cells at different temperatures. The time constant decreases (as expected) for increasing temperatures, as the exchange reaction becomes faster. The results for chromaffin and HEK cells match very closely, so that it is safe to assume that there is no fundamental difference in the mechanism of clathrin exchange in the two cell types.

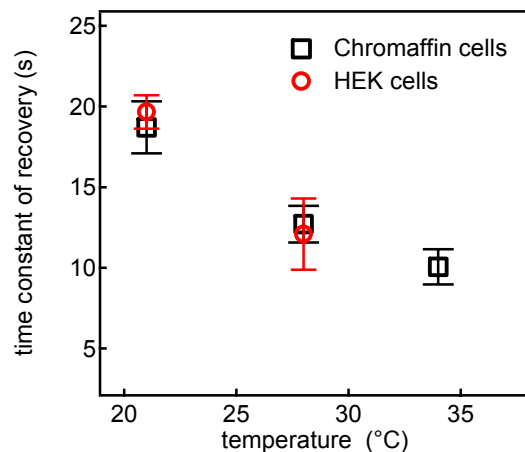


Fig. 4.14: Temperature-dependent time constant of recovery

The time constant of recovery τ (corresponding to $1/k_{\text{off}}$) for different temperatures measured in chromaffin and in HEK cells. τ decreases with increasing temperature. $Q_{10} = 1.6 \pm 0.2$. For n see figure 4.13.

4.1.6 Inhibition of clathrin light chain exchange

In addition to the treatments to disrupt light chain exchange in paragraph 4.1.1 (hypertonic sucrose and ATP depletion with rotenone), cells were now treated with 200 μ M EGTA ester to deplete calcium. Additionally, cells were permeabilised* with 20 μ M digitonin in calcium-free solution (containing 5mM EGTA). Figure 4.15 summarizes the effect of the different treatments on the amplitude of recovery (α - β) of clathrin light chain. (For the data point “untreated”, experiments in HEK cells and chromaffin at room temperature were grouped together).

* *Permeabilisation*: A number of toxins (including digitonin) form large pores in the cell membrane. The pores allow the entry of macromolecules that are not normally membrane-permeant; in the experiments of this study, the pores formed by digitonin permit the entry of external solution into the cell and thus the control of internal Ca^{2+} or ATP concentration.

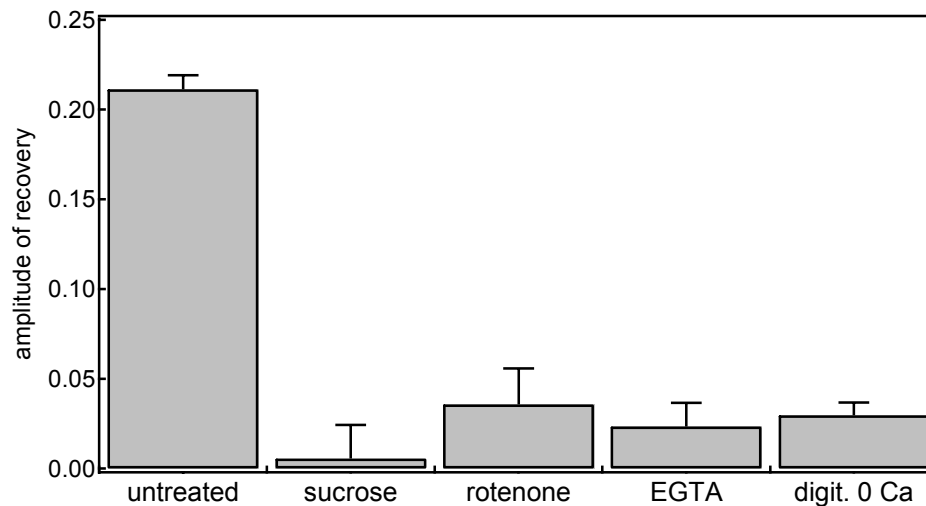


Figure 4.15: Summary of recovery amplitude for different treatments Clathrin light chain recovery ($\tau=18.9\pm 1.3s$ in untreated cells, $n=70$) is inhibited by EGTA treatment ($n=20$), by hypertonic sucrose treatment ($n=18$), by ATP-depletion ($n=19$), and in permeabilized cells in $0-Ca^{2+}$ solution ($n=17$).

Clathrin light change exchange is blocked by sucrose treatment, by ATP depletion with rotenone, and by Ca^{2+} -depletion (both with EGTA ester treatment and with permeabilisation in zero calcium solution).

4.2 Clathrin heavy chain results

The clathrin heavy chain GFP fusion construct used for the following experiments was made by my colleague Martin Wienisch. It is used here to draw a direct comparison between light chain and heavy chain exchange. All experiments in the following paragraphs measured recovery from 10s bleaching in HEK cells, which were transfected with the heavy chain construct with lipofectamine.

4.2.1 Temperature dependent recovery of heavy chain

First, the temperature-dependent time-course of recovery from photobleaching was measured in the same fashion as for light chain. At all available temperatures, clathrin heavy chain recovers with a faster time constant than clathrin light chain. The values for the time constant τ are on the order of 20% smaller than for clathrin light chain.

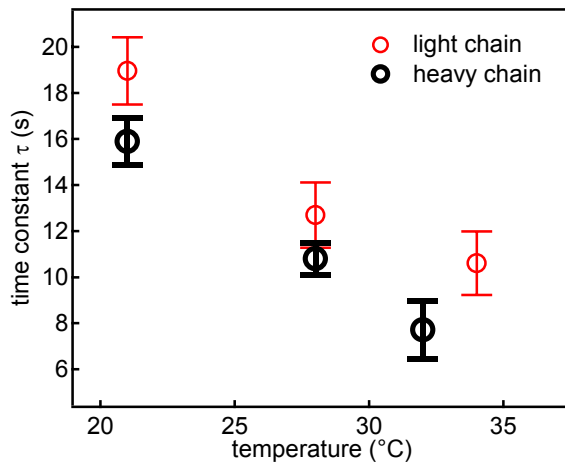


Figure 4.15: Temperature-dependent recovery of clathrin heavy chain

Clathrin heavy chain (black trace) recovers with an exponential time constant approximately 20% faster than light chain (red trace). Light chain data constitute the average of HEK cell and chromaffin cell results. Heavy chain measurements: room temperature n=70; T=28°C n=14; T=32°C n=11.

4.2.2 Inhibition of clathrin heavy chain exchange

Next, the treatments used to disrupt clathrin light chain function were also used on heavy chain (hypertonic sucrose, calcium depletion with EGTA-AM treatment, and experiments on permeabilised cells in Ca^{2+} -free or in ATP-free medium).

The results of the different treatments are summarized in figure 4.16a and b, where the recovery amplitudes and the time constant of recovery are shown. Neither sucrose treatment nor calcium or ATP depletion could completely abolish recovery of heavy chain (treatment with rotenone or with oligomycin also did not suppress recovery, data not shown).

The recovery amplitude appeared to increase for sucrose treatment and to decrease for EGTA treatment; a significant decrease was seen for complete ATP or Ca^{2+} -depletion in permeabilised cells. The time constant of recovery of heavy chain was increased significantly by sucrose treatment; interestingly, it is reported in the literature (Wu et al., 2003) that the rate of (light chain-independent) AP-2 exchange from pits is also increased by sucrose treatment, and this may in fact represent a characteristic side effect of hypertonic sucrose.

After Ca^{2+} -depletion with EGTA-AM or by permeabilising the cell in Ca^{2+} -free solution, the speed of pit recovery is increased, while the amplitude of recovery is decreased by 20% (EGTA-AM) to 40% (permeabilised cells); the result for complete ATP depletion by permeabilising the cell in ATP-free solution is similar to the Ca^{2+} -depleted permeabilised cells. Since this decrease occurs both in the permeabilised cells and in the cells treated with

EGTA-AM (the membrane-permeant ester form of EGTA), it can be ruled out that it is an effect of the permeabilisation itself. While permeabilisation of the cells with digitonin will eventually lead to large holes in the cell membrane, which do not only permit the access of the external solution, but also lead to a washout of the diffusible fraction of fluorophores (and therefore to a progressive reduction of the reaction recovery), cells with a significant decrease of the diffusion recovery signal are no longer included in the analysis.

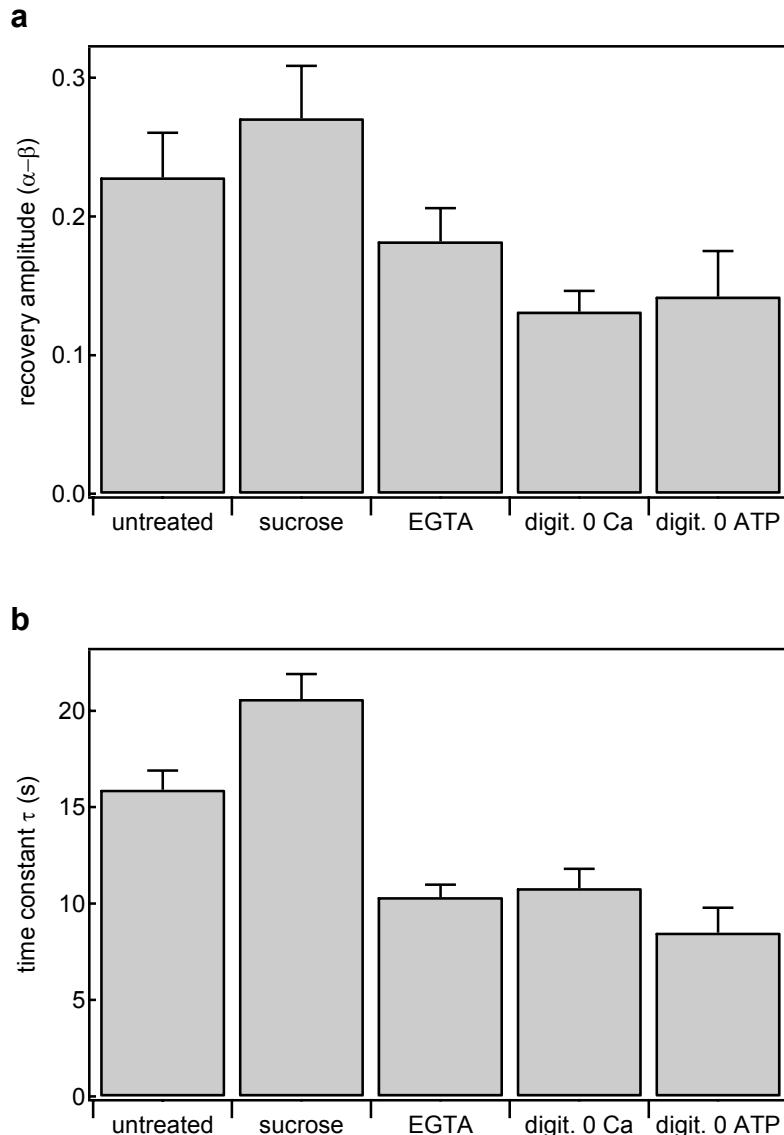


Figure 4.16: Heavy chain recovery for different treatments

a: Recovery amplitude. None of the treatments inhibited clathrin heavy chain exchange, although the amplitude was reduced for Ca^{2+} and ATP depletion. (Untreated cells $n=70$, sucrose treatment $n=29$, EGTA treatment $n=17$, digitonin in 0 Ca^{2+} $n=11$, digitonin in 0 ATP $n=8$)

b: Recovery time constants Sucrose treatment increased the time constant, Ca^{2+} and ATP depletion reduce the time constant to approximately 10s.

4.2.3 Model for clathrin heavy chain exchange

From the measured results of clathrin heavy chain exchange, it can be concluded that:

(1) Clathrin heavy chain is able to exchange independently of clathrin light chain (since treatments that abolish light chain exchange do not abolish heavy chain exchange),

and that therefore, in spite of the high affinity of the chains to each other, a pathway of heavy chains without light chains must exist.

(2) The light-chain-independent pathway of heavy chain is faster than the pathway of exchange where heavy and light chain are bound to each other, because the suppression of light chain exchange leads to an increase in speed (a reduction of the time constant τ).

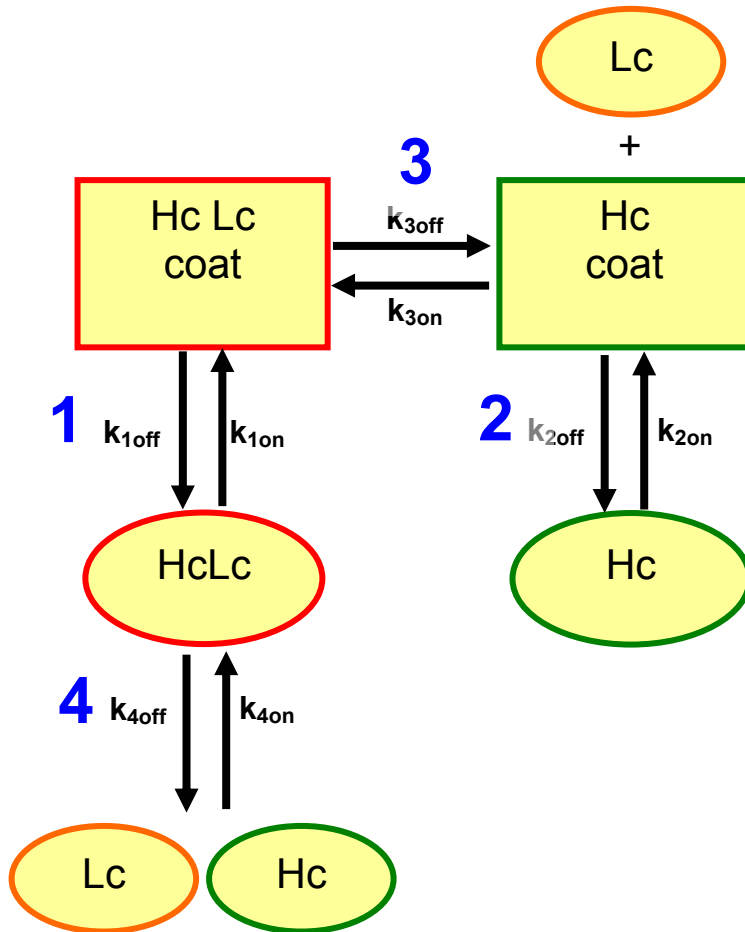


Figure 4.17: Model for clathrin exchange

The boxes represent clathrin heavy chain (Hc) in its bound form in pits, with or without light chain (Lc) bound to it. The circles represent the freely diffusible form of both light chain and heavy chain.

Heavy chain can disassemble from a coat both with light chain bound to it (pathway 1) or without bound light chain (pathway 2). Light chain can bind to and unbind from heavy chain while in the coat (pathway 3). A free heavy-chain-light-chain molecule can disassemble further into (presumably) a heavy chain triskelion and free light chains (pathway 4).

Therefore, a simple model of clathrin heavy chain and light chain exchange is proposed, which is shown schematically in figure 4.17.

This model implies the following differences for heavy chain and light chain dynamics: When experiments are performed with the light chain construct, the only visible pathways for exchange are pathway 1 and pathway 3, and the measured off-rate is a combination of k_{3off} and k_{1off} . Due to the high affinity of light and heavy chain $k_{3off} \ll k_{1off}$, so that the contribution of pathway 3 is probably negligible; thus the measured value for the exchange rate, $k_{light} = 1/(18.9s) = 0.053s^{-1}$ (at room temperature) constitutes a good approximation for k_{1off} .

In measurements on fluorescent clathrin heavy chain, the exchange through the pathways 1 and 2 is observed, so that both $k_{1\text{off}}$ and $k_{2\text{off}}$ contribute to the measured value of $k_{\text{heavy}}=1/(15.9\text{s})=0.063\text{s}^{-1}$. Since $\tau_{\text{heavy}}<\tau_{\text{light}}$, $\tau_{2\text{off}}$ must also be shorter than $\tau_{1\text{off}}$ to yield the combined value of τ_{heavy} . This conclusion is consistent with the idea that clathrin light chain serves to stabilize the coat; thus, the dissociation of a heavy chain-light chain complex from coats is slower than the dissociation of heavy chain triskelia or molecules without light chains.

For use of both the clathrin light chain and the heavy chain fusion construct, pathway 4 is invisible.

This model also implies that the recovery in heavy chain is actually not a mono-, but a biexponential function; but while it is possible to fit a double exponent to our data, our noise level is too high for reliable results. Fitting the recovery with a double exponential function, where one time constant is kept fixed to the value of $\tau=1/k_{1\text{off}}=18.9\text{s}$, yields a second exponential time constant on the order of magnitude of several seconds.

The light-chain independent time constant can be determined more precisely from the experiments in paragraph 4.2.2. For calcium or ATP depletion, the light chain-dependent pathway is abolished, while the light chain-independent pathway of exchange is unaffected by the treatment; presumably, the resulting time course of recovery is again a mono-exponential function where the time constant is $\tau=1/k_{2\text{off}}$. This is supported by the fact that for calcium depletion, the amplitude of the recovery also decreases significantly, corresponding to the simple “removal” of one exponential component contributing to recovery.

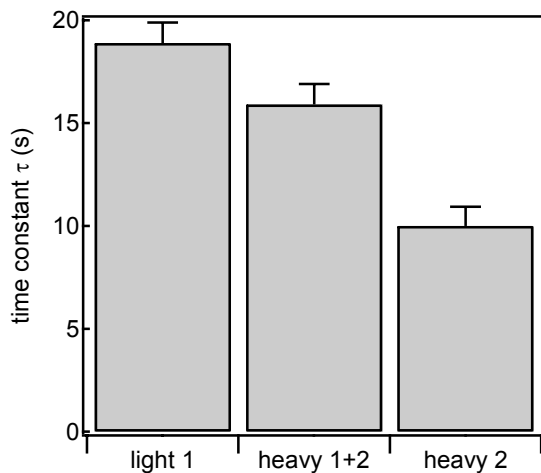


Figure 4.18: Recovery time constant τ in different exchange pathways.

Light chain (pathway 1), n=70.

Heavy chain (pathway 1 and pathway 2), n=70.

Isolated light-chain independent heavy chain (pathway 1) n=39.

Thus, the time constants calculated for calcium-depleted and ATP-depleted cells ($\tau=10.3 \pm 0.7s$ for EGTA-AM treatment, $n=17$ cells, $\tau=10.8 \pm 1.0s$ in permeabilised cells in Ca^{2+} -free solution, $n=12$ cells, $\tau=8.5 \pm 1.3s$ in permeabilised cells in ATP-free solution, $n=10$ cells) constitute an estimate for the second component, yielding an average of $\tau=10.0 \pm 0.9s$ and $k_{2off}=0.10 \pm 0.01s^{-1}$. These results are summarized in figure 4.18, where the time constants τ for exchange through the different pathways are shown. Pathway 1 is determined through light chain recovery, normal heavy chain recovery constitutes a combination of pathway 1 and 2, and calcium- (or ATP-) depleted heavy chain recovery determines the separated time constant of pathway 2.

Using a linear extrapolation of the form

$$a_1\tau_1 + a_2\tau_2 = \tau_{measured}$$

where $\tau_1 = \tau_{light} = 18.9 \pm 1.3s$ and $\tau_2 = \tau_{isolated HC} = 10.0 \pm 0.9s$ as above and $a_1 + a_2 = 1$,

the relative contributions a_1 and a_2 of the clathrin light chain-bound and light chain-independent pathway can be estimated to be approximately 65% and 35%, respectively, in the heavy chain experiment yielding $\tau_{heavy}=15.9s$, i.e. for HEK cells overexpressing clathrin heavy chain about 6-8 hours after transfection. It must be noted that the overexpression itself may constitute a shift in the equilibrium towards the light chain-independent pathway, simply through the oversupply of heavy chain molecules, and that the relative contribution of the light chain-independent pathway in normal cells is likely to be much smaller.

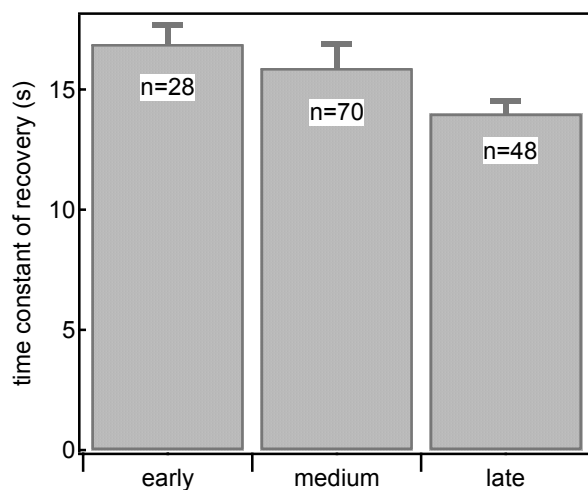


Figure 4.19: Recovery time constant for different expression times

Time constant of recovery of clathrin heavy chain construct was measured in HEK cells at different times after the transfection: early (4-5.5h after transfection), medium (6-9h after transfection) and late (10-12h after transfection).

Along the same line of reasoning, the above model predicts that for a progressive overexpression of clathrin heavy chain, the “combined” rate constant k_{heavy} should increase

(and the time constant τ should decrease). Through the overexpression and thus oversupply of heavy chain, the equilibrium is shifted further towards pathway 2 (heavy chain exchanging without light chain), and the faster time constant of this pathway contributes a larger fraction to the global exchange.

Additional experiments were performed to demonstrate that this is indeed the case. Figure 4.19 shows the results of measuring the combined time constant τ_{heavy} for different expression levels. For lower expression levels than normal (measuring the cells after 4-5.5 hours after transfection, when the expression just becomes visible), the time constant τ_{heavy} is increased from 15.9 ± 1.0 s to 17.2 ± 0.8 s. For higher expression levels (measuring the cells later than 10 hours after transfection), the time constant is decreased to 14.0 ± 0.5 s.

To prove that this effect was indeed caused by a relative oversupply of heavy chain vs. light chain molecules, a “rescue” experiment was performed with a double transfection, where the (green) clathrin heavy chain GFP construct was co-transfected with a light chain mRFP construct (red) (see figure 4.20). In these cells, the relative oversupply of heavy chain was counteracted by the simultaneous overexpression of light chain. Cells with double staining were identified in EPI illumination, and heavy chain recovery was recorded in the green channel as normal. While the (red) light chain was invisible in the green channel, its overexpression prevented the progressive decrease of the recovery time constant τ with the time after transfection.

As a control for the double transfection, a mock double transfection was performed using an mRFP construct instead of the light chain-mRFP construct. For the mock double transfection, the modifying effect of the overexpression level of heavy chain on the time constant was restored. From this result, it is clear that the removal of the modifying effect during the double transfection was not a side effect of the transfection itself, but rather the result of the relative expression level of light chain.

These results are summarized in figure 4.20. The graph shows the recovery time constant of clathrin heavy chain for different expression levels (low, medium, and high), for the normal heavy chain overexpression (“single (HC)”, corresponding to the data shown in figure 4.18), for the “double” transfection of heavy and light chain, and for the “mock” double transfection with the heavy chain construct together with the free mRFP construct.

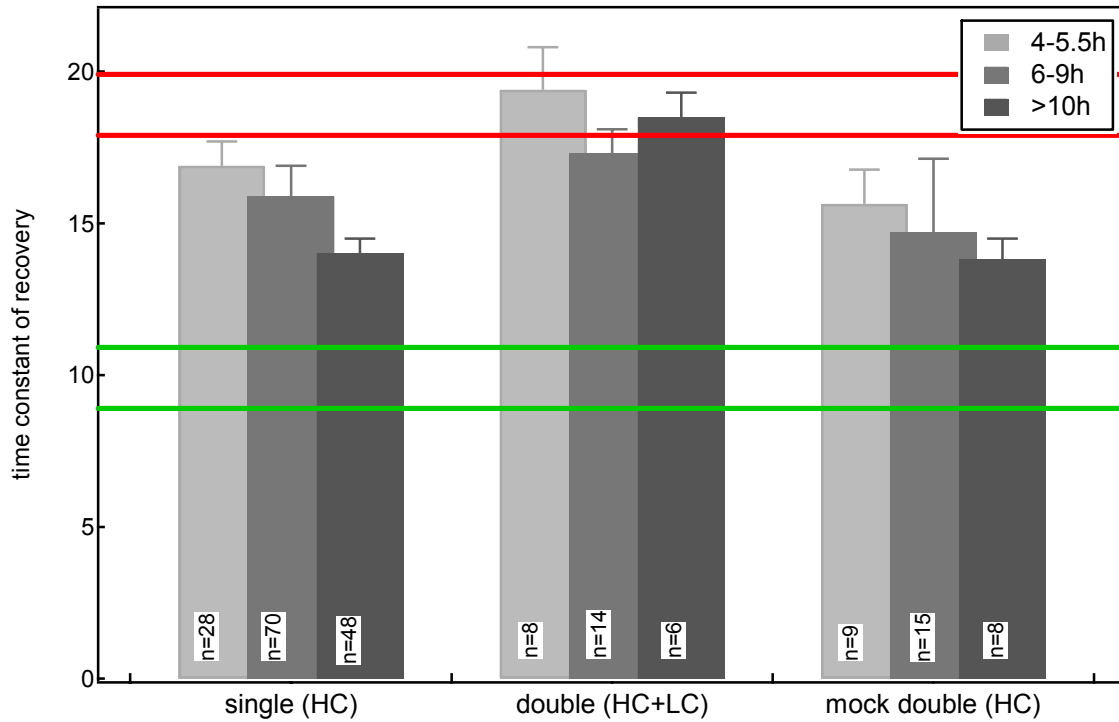


Figure 4.20: Heavy chain recovery time constant for different expression levels (low: 4-5.5 hours; medium: 6-9 hours; high: over 10 hours).

“Single (HC)”: cells are transfected with clathrin heavy chain EGFP; the recovery time constant decreases with increasing expression level. “double (HC+LC)”: cells were transfected with clathrin heavy chain EGFP and with clathrin light chain mRFP; no significant change of the recovery time constant was observed for different expression levels. “mock double (HC)”: cells were transfected with clathrin heavy chain EGFP and free mRFP; the decrease of the time constant was restored.

Red lines are upper and lower limit (mean \pm SD) of the estimated time constant τ_{1off} of the light chain-dependent pathway; green lines represent upper and lower limit of the estimated (light chain-independent) time constant τ_{2off} .

The speed and time course of (over-)expression of the heavy chain-EGFP and the light chain-mRFP construct are, of course, not necessarily the same. However, when assuming that they are at least similar for the time window considered, the relative contributions of the light-chain dependent and light-chain independent pathways can be expected to remain fairly constant (and certainly closer to the physiological conditions than would be the case for overexpression of just a single construct). Under these circumstances, the results for the different expression levels of the double transfection can be averaged, which yields $\tau_{double}=18.1\pm 1.0s$.

This double-transfection value for heavy chain is very close to $\tau_{light}=18.9s\pm 1.3s$, and it is considerably higher than the results for heavy-chain-only transfection, even than the value for the shortest feasible transfection times of about 4 hours, when the first green cells can be distinguished. This implies that for heavy-chain-only transfection, the overexpression

of the heavy chain construct progresses rapidly to a high level, so that for measurements after several hours, the equilibrium has already been shifted from the physiological level towards the light-chain-independent pathway.

Using the linear extrapolation $a_1\tau_1 + a_2\tau_2 = \tau_{measured}$ as above, the relative contributions a_1 and a_2 of the clathrin light-chain dependent and light-chain independent pathways are estimated from the value of $\tau_{double}=18.1\pm 1.0s$ to be 95% and 5%, respectively (as opposed to 65% and 35% for medium overexpression of clathrin heavy chain yielding $\tau_{heavy} = 15.9 \pm 1.0s$).

Chapter 5

Discussion

The aim of this work was to use evanescent-wave FRAP microscopy to study the exchange dynamics of single clathrin subunits from clathrin-coated pits at the plasma membrane. The clathrin unbinding rate was calculated from the time course of recovery from photobleaching.

In particular, this work sought to lay the basis for a solid quantitative estimate of the unbinding rate of clathrin light chain by separating diffusion and reaction contributions to the recovery signal. Additionally, this approach was extended to a new clathrin heavy chain fusion construct. By the direct comparison of the light chain with the heavy chain fusion construct, the differential control of the different subunits could be explored.

5.1 Clathrin exchange studied by photobleaching recovery

FRAP has been used in the past in conjunction with confocal microscopy to study the exchange of a clathrin light fusion construct from pits (Wu et al., 2001; Wu et al., 2003; Moskowitz et al., 2003). The first two of these papers have demonstrated in their work that a considerable amount of exchange takes place between bound and unbound clathrin in pits.

This finding is particularly relevant in light of the question whether clathrin pits form *de novo*, or whether pre-existing flat lattices invaginate into pits. In order to turn flat lattices into curved pits, hexagonal lattice structures have to be broken and replaced by pentagons, which requires considerable structural rearrangement. The naturally high degree of exchange of clathrin subunits from pits may be sufficient for this restructuring; this possibility is also supported by another work (Merrifield et al., 2002) suggesting that flat lattices can be rearranged into functional pits. The work by Moskowitz et al., 2003, uses photobleaching recovery as a measure of chemical disruption of clathrin (light chain) function.

Concerning a quantitative estimation of the time course of recovery (i.e. the unbinding rate k_{off}), the one shortcoming of these FRAP studies is their disregard for the variable fraction of labeled clathrin in the cytosolic surroundings caused by the bleaching of the diffusive component. In a FRAP experiment both in confocal and in TIRF microscopy, a typical bleaching interval on the order of 10s will not only bleach the pits at the membrane, but also create a gradient of fluorescent vs. bleached fluorophores in the cytosolic diffusive fraction. This gradient recovers with a time course of several tens of seconds and, depending on cell diameter, may have a slow component that can significantly affect the estimation of the unbinding rate, if the signal is not corrected for diffusion.

In this work a correction for the diffusional contribution to the recovery signal is performed, yielding a reaction recovery signal that follows an exponential time course and can be fitted with a single exponential to yield the time constant of recovery.

First, a set of experiments (using the clathrin light chain fusion construct in chromaffin cells) proved the efficiency of the separation of the diffusional and the reaction components, by showing that they could be manipulated separately, as the reaction recovery component can be selectively removed by a number of treatments that inhibit exchange of light chains from pits. Additionally, it was demonstrated that the observed reaction recovery is not rate-limited by diffusion, i.e. by the re-supply of soluble unbleached fluorophores.

It was found that clathrin light chain exchanges from pits at the membrane with a time constant of $\tau=18.9 \pm 1.3\text{s}$ at room temperature (where $\tau=1/k_{\text{off}}$). The recovery of clathrin light chain could be almost completely blocked by ATP depletion with rotenone, by treatment with hypertonic sucrose, and by Ca depletion (by permeabilising the cells in internal solution containing 5mM EGTA).

As expected, the time constant τ of clathrin light chain exchange is temperature sensitive, with a Q_{10} of approximately 1.6 ± 0.2 ($\tau = 12.7 \pm 1.4$ s for 28°C , $\tau = 10.6 \pm 1.4$ s for 34°C).

These findings point to an even faster exchange than what is found in the literature. Wu et al. (2001 and 2003) estimate the recovery halftime $\tau_{1/2}$ in the range of $\tau_{1/2} = 16$ s (for 37°C) and $\tau_{1/2} = 30$ s (for 28°C). Moskowitz et al. (2003) do not give a value for the halftime, but a rough estimate from their data is $\tau_{1/2} > 30$ s (at 37°). For an exponential function, the recovery halftime $\tau_{1/2}$ depends on the exponential recovery time constant τ as

$$\tau_{1/2} = -\ln(1/2) \cdot \tau.$$

Thus, the studies cited above would predict recovery time constants τ well over 40s for room temperature, if the time course of recovery is indeed a monoexponential function.

The following table is a summary of the results from this study and the results from the literature for comparison. Where measured halftime values are converted into time constants (or vice versa), the converted values are put in brackets.

	$\tau_{1/2}$ at 28°C	τ at 28°C	$\tau_{1/2}$ at $34/37^\circ\text{C}$	τ at $34/37^\circ\text{C}$
Wu et al (2001)	29.9 ± 11.4 s	(43.1 ± 16.4) s	16.2 ± 4.8 s	(23.4 ± 6.9) s
Moskowitz et al(2003)	-	-	≈ 35 s	(≈ 50) s
results of this study	(8.8 ± 1.0) s	12.7 ± 1.4 s	(7.3 ± 1.0) s	10.6 ± 1.4 s

The discrepancy in the estimation of the unbinding rate of clathrin light chain (by a factor of more than two) can probably be entirely attributed to the diffusion correction. Since in the cited studies, data are normalised and no values for typical absolute pit or background intensities are given, there is no evidence from which to estimate whether the relative levels of diffusion are similar to this study. However, even for 10s bleaching (used by the cited studies and in the majority of experiments in this work), the diffusion recovery has a long “tail” of a slow recovery component (see figure 5.1), while the reaction recovery reaches its plateau value quickly. Thus, even for a good signal-to-background ratio, failing to correct for the diffusion contribution will add a slow time component to the signal. As can be seen in figure 5.1, the contamination of the reaction signal with a diffusion component will, both for halftime determination and for exponential fitting, result a significant overestimation of the time constant.

It can be concluded that a diffusion correction is pivotal for a reliable quantitative estimate of the unbinding rate of clathrin from the recovery time course after photobleaching. Additionally, these results still strongly support the possibility of local restructuring of clathrin lattices to form pits, as the exchange takes place even somewhat faster than previously estimated.

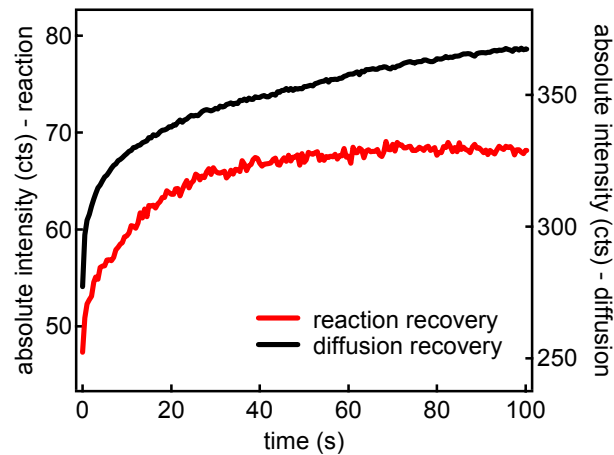


Figure 5.1: Example traces of pit/reaction recovery (red) and diffusive recovery (black) Intensity values are calculated per pixel (diffusion plotted against the right axis, reaction recovery plotted against the left axis).

5.2 Clathrin light chain and heavy chain interaction

Secondly, this study draws a direct comparison between light chain and heavy chain exchange dynamics. Experiments with a clathrin heavy chain fusion construct revealed that the exchange rate of clathrin heavy chain is significantly faster than that of clathrin light chain. Additionally, hypertonic sucrose, ATP-depletion or Ca^{2+} -depletion (all of which inhibit clathrin light chain exchange from pits) do not abolish heavy chain exchange. Thus, it can be postulated that a light-chain independent pathway of exchange must exist for clathrin heavy chain. Therefore, the faster time constant measured for heavy chain is, in fact, the result of exchange through two pathways with different individual time constants.

Until recently, the only clathrin fusion constructs in use were light chain constructs. As it is known that light chains bind to heavy chains with extremely high affinity *in vitro* ($K_D < 10^{-10}$ M) (Winkler and Stanley, 1983), for most practical considerations, heavy chain and light chain were thought to act as a unit in cells, and studies using the available clathrin light chain fusion construct naturally proposed light as chain as representative of function of entire clathrin triskelia.

The first known clathrin heavy chain fusion construct (Damer and O'Halloran, 2000), is a *Dictyostelium* construct, so that it cannot be readily compared to the studies in mammalian cells. Our lab created a novel clathrin heavy chain fusion construct, which is, to our knowledge, the first mammalian fusion construct of clathrin heavy chain, and which makes it possible to compare the exchange dynamics of the clathrin subunits side-by-side.

In this study, it seemed probable that, while heavy chain self-assembly does not require the presence of light chain, due to the high affinity of the two subunits and the regulatory function of light chain *in vivo*, the smallest functional unit to exchange from clathrin coats would be the heavy chain molecules with bound light chains. In this case, one would expect the time course of exchange for heavy chain to be identical to the light chain.

However, it was found that *in vivo*, clathrin heavy chain can and does unbind from clathrin pits independently of light chain to a significant degree, depending on the relative supply of the two subunits, with a significantly faster time constant.

The temperature-dependent time constant of recovery τ_{heavy} was determined for clathrin heavy chain, and was found to be consistently smaller than the light chain time constant. Next, experiments were performed under conditions that inhibit light chain exchange from pits (sucrose treatment, Ca^{2+} -depletion, ATP-depletion); the results was that clathrin heavy chain exchange is not blocked by these treatments, while in some cases the amplitude of recovery was reduced (accompanied by a reduction of the time constant of recovery).

On the basis of these results, it was concluded that the observed recovery must take place through a light-chain independent mechanism. A model was proposed for heavy chain exchange from pits through two pathways, one bound and one unbound to light chain, with differing binding constants. Thus, the observed decrease in the recovery time constant for heavy chain (at room temperature, $\tau_{\text{heavy}}=15.9\pm 1.0\text{s}$) is the result of the mixing of contributions from the slower light-chain bound pathway (with $\tau=18.9 \pm 1.3\text{s}$) and a faster, light-chain independent pathway. This faster pathway is isolated in the experiments that selectively block light chain exchange, i.e. Ca^{2+} -depletion, ATP-depletion (sucrose treatment, while it blocks light chain exchange, also affects other cell functions, and its mechanism is not well known, so it may have secondary effects that affect heavy chain exchange, too). The estimate for the time constant of the fast pathway from these experiments is $\tau = 10.0 \pm 0.9\text{s}$.

As the light-chain bound complex has an approximately two-fold higher unbinding time constant, it can be said to be more stable, so that light chain binding serves to stabilize the heavy chains in the clathrin coat.

This model for the “composition” of the heavy chain time constant of a fast ($\tau = 10.0 \pm 0.9$ s) and a slow ($\tau = 18.9 \pm 1.3$ s) component predicts that the composite time constant will change as the relative contributions of the two pathways change – e.g. by shifting the ratio of available light vs. heavy chains through overexpression of the heavy chain fusion construct.

With increasing overexpression of the heavy chain construct (i.e. with increasing time after transfection of the cell), the relative contribution of the light-chain independent pathway increases, because there is no accompanying increased production of light chains to provide binding partners for the progressive oversupply of heavy chains. Therefore, with rising contribution from the fast pathway, the composite time constant should decrease with expression time.

Experiments show that this is the case, and that the composite time constant drops from $\tau = 16.9 \pm 0.8$ s (for minimum feasible transfection times on the order of 4-5 hours) to $\tau = 14.0 \pm 0.5$ s (for transfection times over 10 hours), with the original value $\tau_{\text{heavy}} = 15.9 \pm 1.0$ s determined at intermediate 6-9 hours. It must be concluded that even intermediate overexpression of the heavy chain construct constitutes a significant shift in the equilibrium of light-chain bound vs. unbound heavy chains. It is difficult to extrapolate the values for overexpression times to zero, as the time course of overexpression is not known, but a rough linear estimate yields $\tau = 18.6 \pm 0.4$ s for physiological expression levels, which is only little smaller than the light chain pathway time constant.

This effect is, as the model predicts, abolished in a double transfection, i.e. when cells are transfected with heavy chain together with a light chain construct. In this case, the overproduction of heavy chain is accompanied by an overproduction of light chains (even if the speed of production is not necessarily the same), so that the natural equilibrium of light-chain bound vs. unbound heavy chains is not disturbed as strongly, and the time constant is $\tau_{\text{double}} = 18.1 \pm 1.0$ s. That this shift was caused by the change in ratio of light chains vs. heavy chains and not by a transfection artifact was proved by a mock transfection, which contained the “empty” mRFP construct, and which restored the transfection-time dependence of the recovery time constant.

Taking together the results of the double transfection and the extrapolation of time-dependent recovery time constants, it can be concluded that at physiological expression levels, the light-chain independent pathway of heavy chain exchange probably contributes less than 5% to the entire clathrin exchange from pits.

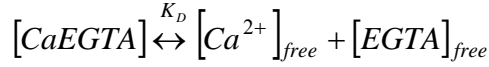
5.3 Outlook

This work has provided insight into the exchange reaction of clathrin molecules from clathrin pits, and, particularly, into the differential control of light chain and heavy chain subunits in clathrin pits. As a next step, it would be of particular interest to extend the FRAP assay to probe the ATP- and calcium dependency of light chain function in a quantitative concentration-dependent fashion.

Additionally, fusion constructs of deletion mutants of clathrin light chain can be tested with this assay, to identify key constituents for the ATP- and calcium dependency of exchange.

APPENDIX

Calcium-EGTA dissociates into free Ca^{2+} and EGTA



so that, by definition

$$\frac{1}{K_D} = \frac{[CaEGTA]}{[Ca^{2+}]_{free} [EGTA]_{free}} \quad \text{or} \quad [Ca^{2+}]_{free} \cdot [EGTA]_{free} = K_D \cdot [CaEGTA]$$

When we substitute into the above equation that

$$[EGTA]_{free} = [EGTA]_{total} - [CaEGTA] \quad \text{and} \quad [CaEGTA] = [Ca^{2+}]_{total} - [Ca^{2+}]_{free} ,$$

we arrive at

$$[Ca^{2+}]_{free}^2 + [Ca^{2+}]_{free} \cdot ([EGTA]_{total} - [Ca^{2+}]_{total} + K_D) - K_D \cdot [Ca^{2+}]_{total} = 0$$

This quadratic formula is solved by

$$x = \frac{-b \pm \sqrt{b^2 - 4ac}}{2a}$$

$$\text{where } [Ca^{2+}]_{free} = x, \quad a = 1, \quad c = -K_D [Ca^{2+}]_{total} \quad \text{and} \quad b = ([EGTA]_{total} - [Ca^{2+}]_{total} + K_D)$$

K_D is pH-dependent and, close to physiological pH, ranges from 20-50nM.

For a more precise calculation (taking into account the presence of additional ions and buffers), a program custom-written in the department (freecon) is used.

Literature

- Alvarez de Toledo G, Fernandez-Chacon R, Fernandez JM (1993) Release of secretory products during transient vesicle fusion.[comment]. *Nature* 363:554-558.
- Aravanis AM, Pyle JL, Tsien RW (2003) Single synaptic vesicles fusing transiently and successively without loss of identity. *Nature* 423:643-647.
- Augustine GJ, Burns ME, DeBello WM, Hilfiker S, Morgan JR, Schweizer FE, Tokumaru H, Umayahara K (1999) Proteins involved in synaptic vesicle trafficking. *J Physiol* 520 Pt 1:33-41.
- Axelrod D (1981) Cell-Substrate Contacts Illuminated by Total Internal Reflection Fluorescence. *The Journal of Cell Biology* 89:141-145.
- Axelrod D (2001) Total internal reflection fluorescence microscopy in cell biology. *Traffic* 2:764-774.
- Axelrod D, Burghardt TP, Thompson NL (1984) Total internal reflection fluorescence. *Annu Rev Biophys Bioeng* 13:247-268.
- Blanpied TA, Scott DB, Ehlers MD (2002) Dynamics and regulation of clathrin coats at specialized endocytic zones of dendrites and spines. *Neuron* 36:435-449.
- Brodin L, Low P, Shupliakov O (2000) Sequential steps in clathrin-mediated synaptic vesicle endocytosis. *Curr Opin Neurobiol* 10:312-320.
- Brodsky FM (1988) Living with clathrin: its role in intracellular membrane traffic. *Science* 242:1396-1402.
- Brodsky FM, Chen CY, Knuehl C, Towler MC, Wakeham DE (2001) Biological basket weaving: formation and function of clathrin-coated vesicles. *Annu Rev Cell Dev Biol* 17:517-568.
- Brodsky FM, Hill BL, Acton SL, Nathke I, Wong DH, Ponnambalam S, Parham P (1991) Clathrin light chains: arrays of protein motifs that regulate coated-vesicle dynamics. *Trends Biochem Sci* 16:208-213.
- Bronstein IN, Semendjajew KA, Musiol G, Mühlig H (2000) Taschenbuch der Mathematik, 5 Edition. Frankfurt am Main: Verlag Harri Deutsch.
- Burghardt TP, Axelrod D (1981) Total internal reflection/fluorescence photobleaching recovery study of serum albumin adsorption dynamics. *Biophys J* 33:455-467.
- Campbell RE, Tour O, Palmer AE, Steinbach PA, Baird GS, Zacharias DA, Tsien RY (2002) A monomeric red fluorescent protein. *Proceedings of the National Academy of Sciences of the United States of America* 99:7877-7882.
- Carslaw H, Jaeger J (1978) Conduction of heat in solids, 2, reprinted Edition. Oxford: Clarendon Press.
- Ceccarelli B, Hurlbut WP, Mauro A (1973) Turnover of transmitter and synaptic vesicles at the frog neuromuscular junction. *J Cell Biol* 57:499-524.
- Chow RH, von Ruden L, Neher E (1992) Delay in vesicle fusion revealed by electrochemical monitoring of single secretory events in adrenal chromaffin cells. *Nature* 356:60-63.
- Chung SH, Takai Y, Holz RW (1995) Evidence that the Rab3a-binding protein, rabphilin3a, enhances regulated secretion. Studies in adrenal chromaffin cells. *Journal of Biological Chemistry* 270:16714-16718.
- Conner SD, Schmid SL (2003) Differential requirements for AP-2 in clathrin-mediated endocytosis. *J Cell Biol* 162:773-779.
- Crank J (1975) The mathematics of diffusion, 2 Edition. Oxford: Clarendon Press.
- Cremona O, De Camilli P (1997) Synaptic vesicle endocytosis. *Curr Opin Neurobiol* 7:323-330.
- Crowther RA, Finch JT, Pearse BM (1976) On the structure of coated vesicles. *J Mol Biol* 103:785-798.
- Damer CK, O'Halloran TJ (2000) Spatially regulated recruitment of clathrin to the plasma membrane during capping and cell translocation. *Mol Biol Cell* 11:2151-2159.
- Datsyuk V (1992) Some characteristics of resonant electromagnetic modes in a dielectric sphere. *Applied Physics B-Photophysics & Laser Chemistry* vol.B54:pp.184-187.
- Denk W, Strickler JH, Webb WW (1990) Two-photon laser scanning fluorescence microscopy. *Science* 248:73-76.

- Gaidarov I, Santini F, Warren RA, Keen JH (1999) Spatial control of coated-pit dynamics in living cells. *Nat Cell Biol* 1:1-7.
- Gesty-Palmer D, Thompson NL (1997) Binding of the soluble, truncated form of an Fc receptor (mouse Fc gamma RII) to membrane-bound IgG as measured by total internal reflection fluorescence microscopy. *J Mol Recognit* 10:63-72.
- Graham FL, Smiley J, Russell WC, Nairn R (1977) Characteristics of a human cell line transformed by DNA from human adenovirus type 5. *Journal of General Virology* 36:59-74.
- Gundelfinger ED, Kessels MM, Qualmann B (2003) Temporal and spatial coordination of exocytosis and endocytosis. *Nat Rev Mol Cell Biol* 4:127-139.
- Hecht E (2002) *Optics*, 4 Edition. San Francisco: Addison Wesley.
- Hellen EH, Axelrod D (1987) Fluorescence Emission at Dielectric and Metal-Film Interfaces. *J Opt Soc Am B* 4:337-350.
- Heuser J (1980) 3-Dimensional Visualization of Coated Vesicle Formation in Fibroblasts. *Journal of Cell Biology* 84:560-583.
- Heuser JE, Reese TS (1973) Evidence for recycling of synaptic vesicle membrane during transmitter release at the frog neuromuscular junction. *J Cell Biol* 57:315-344.
- Holroyd P, Lang T, Wenzel D, De Camilli P, Jahn R (2002) Imaging direct, dynamin-dependent recapture of fusing secretory granules on plasma membrane lawns from PC12 cells. *Proceedings of the National Academy of Sciences of the United States of America* 99:16806-16811.
- Huang KM, Gullberg L, Nelson KK, Stefan CJ, Blumer K, Lemmon SK (1997) Novel functions of clathrin light chains: clathrin heavy chain trimerization is defective in light chain-deficient yeast. *J Cell Sci* 110 (Pt 7):899-910.
- Jarousse N, Kelly RB (2001) Endocytotic mechanisms in synapses. *Curr Opin Cell Biol* 13:461-469.
- Keen JH, Willingham MC, Pastan IH (1979) Clathrin-coated vesicles: isolation, dissociation and factor-dependent reassociation of clathrin baskets. *Cell* 16:303-312.
- Kirchhausen T (2000) Clathrin. *Annu Rev Biochem* 69:699-727.
- Kirchhausen T, Scarmato P, Harrison SC, Monroe JJ, Chow EP, Mattaliano RJ, Ramachandran KL, Smart JE, Ahn AH, Brosius J (1987) Clathrin light chains LCA and LCB are similar, polymorphic, and share repeated heptad motifs. *Science* 236:320-324.
- Klingauf J, Kavalali ET, Tsien RW (1998) Kinetics and regulation of fast endocytosis at hippocampal synapses. *Nature* 394:581-585.
- Koenig JH, Yamaoka K, Ikeda K (1998) Omega images at the active zone may be endocytotic rather than exocytotic: implications for the vesicle hypothesis of transmitter release. *Proc Natl Acad Sci U S A* 95:12677-12682.
- Kosaka T, Ikeda K (1983) Reversible blockage of membrane retrieval and endocytosis in the garland cell of the temperature-sensitive mutant of *Drosophila melanogaster*, shibirets1. *J Cell Biol* 97:499-507.
- Lindner R, Ungewickell E (1991) Light-chain-independent binding of adaptors, AP180, and auxilin to clathrin. *Biochemistry* 30:9097-9101.
- Liu SH, Wong ML, Craik CS, Brodsky FM (1995) Regulation of clathrin assembly and trimerization defined using recombinant triskelion hubs. *Cell* 83:257-267.
- Marsh M, McMahon HT (1999) The structural era of endocytosis. *Science* 285:215-220.
- Marty A, Neher E (1985) Potassium channels in cultured bovine adrenal chromaffin cells. *Journal of Physiology* 367:117-141.
- Mattheyses A, Axelrod D (2002) Measurement of fluorophore excitation and emission properties near bare and metal coated surfaces. *Biophysical Journal* 82:499a-500a.
- McPherson PS, Kay BK, Hussain NK (2001) Signaling on the endocytic pathway. *Traffic* 2:375-384.
- Merrifield CJ, Feldman ME, Wan L, Almers W (2002) Imaging actin and dynamin recruitment during invagination of single clathrin-coated pits. *Nat Cell Biol* 4:691-698.
- Miller TM, Heuser JE (1984) Endocytosis of synaptic vesicle membrane at the frog neuromuscular junction. *J Cell Biol* 98:685-698.
- Minsky M (1988) Memoir on Inventing the Confocal Scanning Microscope. *Scanning* 10:128-138.
- Moore MS, Mahaffey DT, Brodsky FM, Anderson RG (1987) Assembly of clathrin-coated pits onto purified plasma membranes. *Science* 236:558-563.

- Moskowitz HS, Heuser J, McGraw TE, Ryan TA (2003) Targeted chemical disruption of clathrin function in living cells. *Mol Biol Cell* 14:4437-4447.
- Motley A, Bright NA, Seaman MN, Robinson MS (2003) Clathrin-mediated endocytosis in AP-2-depleted cells. *J Cell Biol* 162:909-918.
- Mueller VJ, Wienisch MW, Nehring RBN, Klingauf JK (accepted) Monitoring Clathrin-mediated Endocytosis during Synaptic Activity. *Journal of Neuroscience*.
- Nagy G, Matti U, Nehring RB, Binz T, Rettig J, Neher E, Sorensen JB (2002) Protein kinase C-dependent phosphorylation of synaptosome-associated protein of 25 kDa at Ser187 potentiates vesicle recruitment. *Journal of Neuroscience* 22:9278-9286.
- Oheim M, Loerke D, Stühmer W, Chow RH (1998) The last Few Milliseconds in the Life of a Secretory Granule. Early Steps of Exocytosis visualized by Total Internal Reflection Fluorescence Microscopy (TIRFM). *Eur Biophys J* 27:83-98.
- Oheim M, Loerke D, Stuhmer W, Chow RH (1999) Multiple stimulation-dependent processes regulate the size of the releasable pool of vesicles. *Eur Biophys J* 28:91-101.
- Olveczky BP, Periasamy N, Verkman AS (1997) Mapping fluorophore distributions in three dimensions by quantitative multiple angle-total internal reflection fluorescence microscopy. *Biophysical Journal* 73:2836-2847.
- Pearse BM (1976) Clathrin: a unique protein associated with intracellular transfer of membrane by coated vesicles. *Proc Natl Acad Sci U S A* 73:1255-1259.
- Pearse BM (1982) Coated vesicles from human placenta carry ferritin, transferrin, and immunoglobulin G. *Proc Natl Acad Sci U S A* 79:451-455.
- Pearse BM, Robinson MS (1984) Purification and properties of 100-kd proteins from coated vesicles and their reconstitution with clathrin. *Embo J* 3:1951-1957.
- Rappoport JZ, Simon SM (2003) Real-time analysis of clathrin-mediated endocytosis during cell migration. *J Cell Sci* 116:847-855.
- Ryan TA (1996) Endocytosis at nerve terminals: timing is everything. *Neuron* 17:1035-1037.
- Santini F, Gaidarov I, Keen JH (2002) G protein-coupled receptor/arrestin3 modulation of the endocytic machinery. *J Cell Biol* 156:665-676.
- Scott MG, Benmerah A, Muntaner O, Marullo S (2002) Recruitment of activated G protein-coupled receptors to pre-existing clathrin-coated pits in living cells. *J Biol Chem* 277:3552-3559.
- Shupliakov O, Low P, Grabs D, Gad H, Chen H, David C, Takei K, De Camilli P, Brodin L (1997) Synaptic vesicle endocytosis impaired by disruption of dynamin-SH3 domain interactions. *Science* 276:259-263.
- Slepnev VI, De Camilli P (2000) Accessory factors in clathrin-dependent synaptic vesicle endocytosis. *Nat Rev Neurosci* 1:161-172.
- Smith CJ, Grigorieff N, Pearse BM (1998) Clathrin coats at 21 Å resolution: a cellular assembly designed to recycle multiple membrane receptors. *Embo J* 17:4943-4953.
- Steyer J, Almers W (1999) Tracking single secretory granules in live chromaffin cells by evanescent-field fluorescence microscopy. *Biophysical Journal* 76:2262-2271.
- Steyer JA, Horstmann H, Almers W (1997) Transport, Docking and Exocytosis of Single Secretory Granules in Live Chromaffin Cells. *Nature* 388:474-478.
- Stout AL, Axelrod D (1995) Spontaneous recovery of fluorescence by photobleached surface-adsorbed proteins. *Photochem Photobiol* 62:239-244.
- Sund SE, Axelrod D (2000) Actin dynamics at the living cell submembrane imaged by total internal reflection fluorescence photobleaching. *Biophys J* 79:1655-1669.
- Sund SE, Swanson JA, Axelrod D (1999) Cell membrane orientation visualized by polarized total internal reflection fluorescence. *Biophys J* 77:2266-2283.
- Swaminathan R, Bicknese S, Periasamy N, Verkman AS (1996) Cytoplasmic viscosity near the cell plasma membrane: translational diffusion of a small fluorescent solute measured by total internal reflection-fluorescence photobleaching recovery. *Biophys J* 71:1140-1151.
- Takei K, Mundigl O, Daniell L, De Camilli P (1996) The synaptic vesicle cycle: a single vesicle budding step involving clathrin and dynamin. *J Cell Biol* 133:1237-1250.
- Thompson NL, Burghardt TP, Axelrod D (1981) Measuring surface dynamics of biomolecules by total internal reflection fluorescence with photobleaching recovery or correlation spectroscopy. *Biophys J* 33:435-454.

- Thomson DJ, Chave and A. D. (1991) Jackknifed Error Estimates for Spectra, Coherences, and Transfer Functions. In: *Advances in Spectrum Estimation*' (Haykin S, ed), pp 58-113. Prentice: Hall.
- Ungewickell E, Ungewickell H, Holstein SE, Lindner R, Prasad K, Barouch W, Martin B, Greene LE, Eisenberg E (1995) Role of auxilin in uncoating clathrin-coated vesicles. *Nature* 378:632-635.
- Wang J, Virta VC, Riddelle-Spencer K, O'Halloran TJ (2003) Compromise of clathrin function and membrane association by clathrin light chain deletion. *Traffic* 4:891-901.
- Winkler FK, Stanley KK (1983) Clathrin heavy chain, light chain interactions. *Embo J* 2:1393-1400.
- Wu X, Zhao X, Baylor L, Kaushal S, Eisenberg E, Greene LE (2001) Clathrin exchange during clathrin-mediated endocytosis. *J Cell Biol* 155:291-300.
- Wu X, Zhao X, Puertollano R, Bonifacino JS, Eisenberg E, Greene LE (2003) Adaptor and clathrin exchange at the plasma membrane and trans-Golgi network. *Mol Biol Cell* 14:516-528.
- Ybe JA, Greene B, Liu SH, Pley U, Parham P, Brodsky FM (1998) Clathrin self-assembly is regulated by three light-chain residues controlling the formation of critical salt bridges. *Embo J* 17:1297-1303.
- Zenisek D, Steyer JA, Almers W (2000) Transport, capture and exocytosis of single synaptic vesicles at active zones. *Nature* 406:849-854.
- Zhang B, Ganetzky B, Bellen HJ, Murthy VN (1999) Tailoring uniform coats for synaptic vesicles during endocytosis. *Neuron* 23:419-422.
- Zhang B, Koh YH, Beckstead RB, Budnik V, Ganetzky B, Bellen HJ (1998) Synaptic vesicle size and number are regulated by a clathrin adaptor protein required for endocytosis. *Neuron* 21:1465-1475.
- Zhang JZ, Davletov BA, Sudhof TC, Anderson RG (1994) Synaptotagmin I is a high affinity receptor for clathrin AP-2: implications for membrane recycling. *Cell* 78:751-760.

Acknowledgements

I would like to thank my supervisors, head of department Prof. Dr. Neher and group leader Dr. Jürgen Klingauf, for making this work possible, for their enormous patience, and for their critical and continuous support through the past years.

I am also grateful to my co-referee Prof. Dr. A. Zippelius, and to my former boss, Prof. Dr. W. Stühmer, whom I thank for his support and open-mindedness.

In my present lab, I owe a million thanks to my colleagues whose input helped this project along, and whose presence made coming to work every day enjoyable. I thank Martin Wienisch for going beyond the call of duty to make the clathrin heavy chain construct, and for his smooth disposition. Edward Lemke made the light chain mRFP construct and provided me with daily entertainment and great movie ideas. Vroni Müller shared her library and her clathrin expertise, and very often provided some badly needed perspective. Alexey Kochubey was an immeasurable resource of technical information, as well as a source of calm and moral support. Dr. Pieter Vanden Berghe was the axis of maturity in our office, and a man of scientific good sense and human wisdom.

I also want to thank Dr. Ralf Nehring and Dr. Maria Krikunova for their help and input, Michael Pilot for his work and his good cheer, and Ina Herfort for some of the best chromaffin cells and some of the best conversations I've had during my time here. Thanks to Ira Milosevic and Attila Gulyás-Kovács for help with freecon, solutions and chromaffin cells, and to Irmgard Barteczko for her good advice in tough times.

In my former lab, I owe thanks to my great co-workers Tatiana Fiordelisio and Marc Jenke, for improving my morale and perspective, and spending quality time with me.

There are many people outside the lab who supported me and shared my fortunes, frustrations and in-betweens, without whose help this work would not have been possible. I thank my parents, who were interested and there when needed; I thank Raffael Hoffmann for the fun and for providing a different view on life while consistently supporting my "job self". I am grateful to all my friends, to the many fellow PhD students (particularly Robert Weber, Annette Bundy, and Birte Werner), to the fellow physicists (particularly Justus Loerke, Dagmar Krefting, and Reinhard Geisler), and in the muses' department, to Lore Caspary and Vahagn Maloyan for their faith in my abilities.

I would probably not be here without the example of the many brilliant and inspiring women academics in my family. Above all of these, for their love and support through all of my life, I want to thank my aunt and godmother Dr. Verena Fertmann, and my beloved late grandmother Dr. Gisela Fertmann.

CURRICULUM VITAE

Persönliche Angaben:

Name: Dinah Loerke

Geboren: 18.08.1972 in München

Eltern: Gertrud und Bernd Loerke

Staatsangehörigkeit: deutsch

Familienstand: ledig

1979-1982	Volksschule Flotowgasse, Wien (Österreich)
1982-1984 und 1985-1991	Schickhardt-Gymnasium Herrenberg (Baden-Württemberg)
1984/85	St. Anthony's School, Thornhill (Kanada)
Juni 1991	Abitur
Oktober 1991 – Oktober 1995 Oktober 1996 – Oktober 1998	Studium der Physik, Universität Göttingen
Oktober 1995 – September 1996	Studium der Japanologie, Universität Chiba (Japan) (<i>Japanese Studies</i> -Stipendium des japanischen Kultusministeriums)
Oktober 1998	Diplomhauptprüfung in Physik Titel der Diplomarbeit: „Aufbau und Charakterisierung eines Totalreflexions-Fluoreszenzmikroskopes mit veränderlichem Einfallswinkel“, angefertigt am Max-Planck-Institut für experimentelle Medizin, betreut durch Prof. Dr. Walter Stühmer und Prof. Dr. W. Lauterborn
Januar 1999 – August 2001	wissenschaftliche Hilfskraft am Max-Planck-Institut für experimentelle Medizin, Göttingen (Abt. Prof. Dr. Walter Stühmer)
Seit September 2001	wissenschaftliche Hilfskraft am Max-Planck-Institut für biophysikalische Chemie, Göttingen (Abt. Prof. Dr. Erwin Neher)

Göttingen, den 15.01.2004